論文 / 著書情報
Article / Book Information

題目(和文)	量子センサに向けた炭素材料中のスピン状態制御
Title(English)	Spin state control of carbon materials for quantum sensors
著者(和文)	田原康佐
Author(English)	Kosuke Tahara
出典(和文)	学位:博士(工学), 学位授与機関:東京工業大学, 報告番号:甲第10152号, 授与年月日:2016年3月26日, 学位の種別:課程博士, 審査員:波多野 睦子,小田 俊理,宮本 恭幸,河野 行雄,小寺 哲夫,都倉 康弘
Citation(English)	Degree:Doctor (Engineering), Conferring organization: Tokyo Institute of Technology, Report number:甲第10152号, Conferred date:2016/3/26, Degree Type:Course doctor, Examiner:,,,,,
学位種別(和文)	博士論文
Type(English)	Doctoral Thesis

Spin state control of carbon materials for quantum sensors

Kosuke Tahara
Department of Physical Electronics
Tokyo Institute of Technology

February 19, 2016

Abstract

Carbon-based solid state materials are promising platforms for spin state control and engineering because of small spin-orbit interaction and lack of nuclear spin in the most abundant isotope (^{12}C). Paramagnetic impurities are introduced in these materials in order to control the electron spin state. We consider two different types of impurities: the impurity to control the spin state of conduction electrons in conductor and the one in insulator which serves as the localized spin state for sensing.

First, we discuss the charge and spin current transport in fluorinated graphene. Although graphene is known as a good conductor of charge and spin current, its control is difficult. It is shown that carrier and spin transport properties of graphene can be controlled by the impurities, covalently bonded fluorine atoms.

The latter part is devoted to quantum sensor application of nitrogen-vacancy (NV) color center in diamond. Spin state of NV center can be polarized and readout optically, and controlled by electron spin resonance. Toward the realistic application of this unique qubit as sensitive magnetometer, we have developed micro-structure to enhance photon collection efficiency, quantification method of the selective alignment of high density NV centers, and optimized measurement sequence for AC signal.

This thesis is concluded by the outlook for sensor devices and applications combining graphene and diamond.

Contents

List of Figures

List of Tables

Citations to previously published work

Chapter 2 has been published as the following paper:

1. K. Tahara, T. Iwasaki, A. Matsutani, and M. Hatano, Effect of radical fluorination on mono- and bi-layer graphene in Ar/F_2 plasma. Appl. Phys. Lett. **101**, 163105 (2012).

Contents of Chapter 3 have been published in the following two papers:

2. K. Tahara, T. Iwasaki, S. Furuyama, A. Matsutani, and M. Hatano, Asymmetric transport property of fluorinated graphene. Appl. Phys. Lett. **103**, 143106 (2013).

3. ©2014 IEEE. Reprinted, with permission, from
   S. Furuyama, K. Tahara, T. Iwasaki, A. Matsutani, and M. Hatano, Fluorinated Graphene FETs Controlled by Ionic Liquid Gate. IEEE J. Display Technol. **10**, 962 (2014).

Chapter 5 has been published as

4. S. Furuyama*, K. Tahara*, T. Iwasaki, M. Shimizu, J. Yaita, M. Kondo, T. Kodera, and M. Hatano, Improvement of fluorescence intensity of nitrogen vacancy centers in self-formed diamond microstructures. Appl. Phys. Lett. **107**, 163102 (2015).

Most of Chapter 6 and a part of Chapter 7 have been published in

5. K. Tahara, H. Ozawa, T. Iwasaki, and M. Hatano, Quantifying selective alignment of ensemble nitrogen-vacancy centers in (111) diamond. Appl. Phys. Lett., **107**, 193110 (2015).

Inclusion of the articles above, published by American Institute of Physics† and The Institute of Electrical and Electronics Engineers, Inc.,‡ is permitted without obtaining formal reuse licenses.

*These authors contributed equally to the work.

†http://publishing.aip.org/authors/copyright-reuse

‡https://www.ieee.org/publications_standards/publications/rights/permissions_faq.pdf

Acknowledgements

My works have been accomplished only with help of my advisors, co-workers, friends and family.

My supervisors Prof. Hatano and Prof. Kodera gave me the valuable opportunities to pursue a variety of research projects. I have been helped by Prof. Hatano in many aspects since I joined her group as an undergraduate student. Dr. Iwasaki has taught me a lot of practical skills for the research activity. Thesis committee members Prof. Oda, Prof. Miyamoto, Prof. Kawano and Prof. Tokura (Tsukuba Univ.) reviewed my thesis and gave me insightful comments.

Lithographical fabrications of graphene devices and diamond micro-structures (Chapter 3, 4 and 5) were helped by MEXT nanotechnology platform (Prof. Miyamoto, Dr. Yamaguchi and Dr. Kawata). Dr. Matsutani shared many ideas and instruments for graphene fluorination process in Chapter 2. Dr. Ishibashi and Dr. Yamaguchi kindly welcomed me to their laboratory in Riken and gave me a chance to use Helium fridge, which was essential for works in Chapter 4. The measurement system for NV research (Appendix B) could not be built up without help of Prof. Mizuochi (Osaka Univ.) and Prof. Jelezko (Ulm Univ.).

Secretaries in Hatano-Kodera group, Ms. Kobayashi and Ms. Saito helped me to deal with lots of paper works. All of the faculties and students, including former members, in Hatano-Kodera group have been my collaborators and friends. Graphene works have been performed with Satoko Furuyama, Wataru Naruki and Koji Hatano. Diamond micro-structure in Chapter 5 has been simulated and fabricated by Satoko Furuyama and Makio Kondo. CVD diamond samples used in Chapter 6 and 7 have been fabricated by Hayato Ozawa. Wataru Naruki and Kosuke Mizuno have set up the measurement system for NV research with me.

Chapter 1

Introduction

1.1 Carbon materials for the spin state control and quantum sensors

Carbon-based crystalline solids are promising platforms to control and engineer the electron spin state due to small spin-orbit interaction as shown in Table 1.1. Smaller spin-orbit interaction means the less perturbation or noise, which destroys the electron spin state of interest. It is also important that the most abundant isotope (^{12}C) has zero nuclear spin because spin-spin interaction can also affect the spin state. Carbon has many crystalline allotropes with variety of electronic properties including diamond and graphite in three dimensional, graphene in two dimensional, carbon nanotube in one dimensional, and fullerene in zero dimensional spatial degrees of freedom. The paramagnetic impurity is our key to control the electron spin state in these materials. We consider two different types of impurities: the impurity to control the spin state of conduction electrons in conductor and the one in insulator which serves as the localized spin state for sensing.

Crystalline materials with sp^2 hybridized carbons are, in general, known as very good conductors because π electrons form dense conducting channel. In former part of this thesis, we will explore the possibility of spin state control of conduction electrons in graphene. On the other hand, diamond is one of the most typical insulator (semiconductor) with a large band gap of 5.5 eV. Diamond can host huge variety of color centers in its firm structure and large band gap. Amongst them, the nitrogen-vacancy (NV) center has been proven to have one of the most promising localized electronic structure to serve as a spin-based qubit. We present the CVD-based engineering of NV center toward microscopic quantum sensor applications in the latter part.

Table 1.1: Spin orbit interaction in Carbon, Silicon and Germanium. λ is for isolated atom ($\hat{H}_{SO} = \lambda \boldsymbol{L} \cdot \boldsymbol{S}$).[1] Δ_0 is the valence band splitting of diamond-structure solid.[2]

Atom	Atomic number	λ (cm^{-1})	Δ_0 (meV)
C	6	14	13
Si	14	65	44
Ge	32	400	295

Although the principle of quantum sensors will be introduced later in Section 1.6, we briefly introduce the concept and its impact here. Since we can perform sensitive optical detection of electron spin resonance of a single NV center, we can use it as an atomic-scale quantum sensor. The information about local magnetic field, electric field or strain field around the NV center is buried in its spin resonance frequencies. The similar physics can be exploited using atomic vapor for example, however, it is very difficult to achieve high spatial resolution using vapor.

The spin-based quantum sensor is the most sensitive to magnetic field. One of the most important application, which has been demonstrated recently, is nano-scale nuclear magnetic resonance (NMR) and imaging.[3–5] The NV centers at diamond surface can sense local fluctuation of magnetic field by nuclear spins on the surface. In ultimate case NV center can enable NMR with single spin sensitivity.[6] The use of electric field and stain field sensor is also demonstrated.[7, 8]

One goal we would like to set is the use of NV quantum sensor for the probe of spin current and related physics. Since graphene can be formed directly on top of atomically flat (111) surface of diamond,[9] graphene should provide the best bridge which connects spin current and NV center.

1.2 Overview and Structure

Brief reviews of basic physical concepts and previous researches are given in subsequent sections of this chapter. We will start to describe the graphene research by the fluorination methods of graphene using Ar/F_2 plasma in next Chapter (Ch. 2). Chapter 3 and 4 deal with charge and spin transport properties of fluorinated graphene, respectively.

CVD-based optimization of NV-containing diamond will be started by Chapter 5: diamond micro-structure for photon collection efficiency improvement. Next, we discuss the fabrication

and characterization of selectively-aligned high-density NV ensembles in Chapter 6. In Chapter 7, we will demonstrate the operation as actual AC magnetometer of our CVD sample and compare the results with NV center ensemble fabricated by ion-implantation. Chapter 8 will summarize all the researches and show the outlook for sensor devices and applications combining graphene and diamond.

1.3 Graphene and chemical functionalization

1.3.1 Graphene

Intriguing physics and possibility for electron device application of graphene has been attracted intensive attentions since its successful isolation and device demonstration in 2004.[10] It is widely recognized that due to graphene's unique band structure, the carriers (electrons or holes) has extremely high Fermi velocity without mass, resulting in large carrier mobilities. Although the carrier mobility is limited by a number of extrinsic scattering sources, a experimental research marks a value 200,000 cm^2/Vs by reducing them with suspended graphene.[11] Figure 1.1 shows the crystal structure and calculated band structure of graphene. First principles calculation of the band structure is performed using a software based on density functional theory. *

In spite of its large carrier mobility, the zero-gap band structure results in small on-off ratio when graphene is operated as a field-effect transistor (FET). There are several approaches demonstrated for creating a band gap in graphene or tuning its transport property for the switching device applications. Nano-structuring of graphene into a thin line shape, so called graphene nanoribbon, is one of them.[13, 14] This approach uses quantum confinement effect of the electrons within pseudo one dimensional space. An on/off ratio up to 10^6 is achieved by using sub-10 nm nanoribbons in Ref. [14], however, the rough edge of experimentally available structures results in degradation of the carrier mobility. Another approach is application of vertical electric field through bilayer graphene, that creates a potential-asymmetry-induced band gap.[15–18] Beautiful physics are predicted theoretically and observed experimentally, however, induced band gap is small for switching device application at room temperature. Thus, some new approaches should be explored for graphene's electron device applications.

1.3.2 Chemical functionalization of graphene

We shall introduce another way for tuning transport property of graphene, the chemical functionalization. Although our final goal is the control of spin transport (introduced later in Section 1.4),

*The asms/phase software (http://www.asms.co.jp/, https://azuma.nims.go.jp/cms1) is used for this calculation. Self consistent field optimization is performed by using Generalized Gradient Approximation (PBE[12]) exchange term and $24 \times 24 \times 1$ k-point sampling. After that, eigenenergies at each k point of interest are calculated to acquire the band structure.

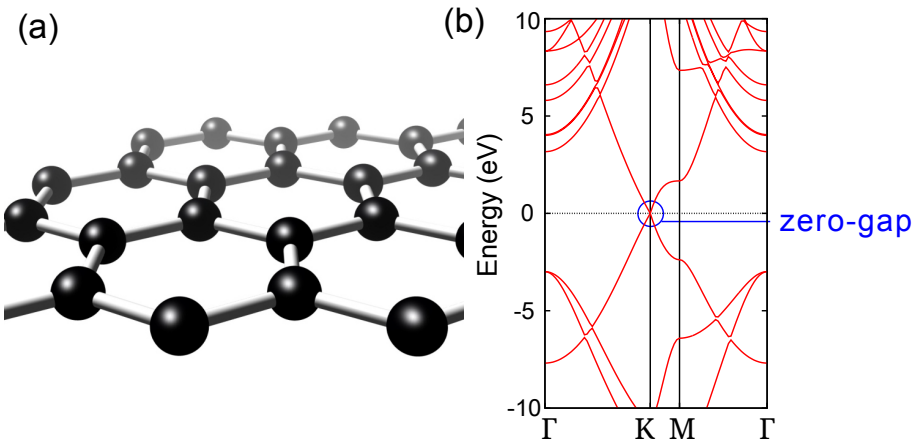

Figure 1.1: (a) Crystal structure of graphene (b) Band structure of graphene calculated by the density functional theory.

the control of charge transport, similar to several approaches above, can also be realized. In this approach, we add covalently bonded adatoms on graphene. Monovalent adatoms like hydrogen or fluorine is the most simplest case, though divalents like oxygen are possible as well. Covalent bonding of these atoms with carbon atoms in graphene makes atomic scale point defects with sp^3-like carbon.

In the extreme case where all carbon atoms are functionalized, graphene should turn into semiconductor with a finite band gap. Such perfectly hydrogenated and fluorinated graphene, named graphane and fluorographene, have been demonstrated both theoretically and experimentally.[19–23] The crystal structure and calculated band structure of fluorographene is shown in Figure 1.2. We can tune transport property continuously in between perfect graphene and perfectly functionalized graphene by controlled functionalization.[24–26] In chapter 3, we will see this kind of charge transport tuning by introducing fluorine with different concentrations.

1.3.3 Difference of midgap impurity states

Here we explain a detailed concept about the effect of adatom impurities on graphene transport, especially about the difference between hydrogen and fluorine. Theoretically, adsorbate atoms like hydrogen or fluorine on graphene create midgap impurity states.[27] Electron scattering rate and resulting conductivity depends on the energy level of this impurity state. It has been reported

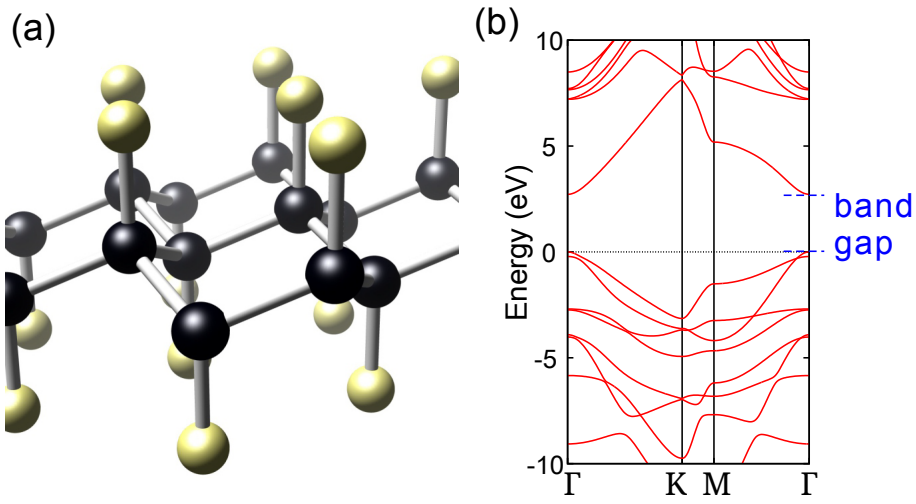

Figure 1.2: (a) Crystal structure of fluorographene (b) Band structure of perfectly fluorinated graphene (fluorographene) calculated by the density functional theory.

that impurity states of hydrogen (H) or organic groups like CH_3 are within ±0.03 eV from the charge neutrality point (CNP), and these impurities lead to negligible electron-hole asymmetry in conductivity.[27, 28] On the other hand, levels of highly electronegative fluorine (F) or hydroxyl (OH) impurity states are at more distant positions from CNP (-0.67 and -0.70 eV, respectively).[27] It is theoretically predicted that impurity resonances at relatively distant energy result in a notable asymmetry and local extremum of conductivity as a function of carrier density.[28–31] Such characteristics, however, have not been experimentally observed in fluorinated graphene. Although transport properties of fluorinated graphene have been reported by some groups,[21, 24–26, 32, 33] discussions on electron-hole asymmetry have not been found. In chapter 3, we will show that the electron-hole asymmetry can be actually introduced by intensive fluorination.

1.4 Spin transport control in graphene

1.4.1 Spin current in graphene

Graphene is a good conductor of the spin current as well as the charge current. The final goal of our graphene research is the control and generation of the spin current by means of chemical functionalization. In this section, we briefly review the concept of the spin current, and previous

studies of spin current in graphene.

The spin current and spintronics

The spin current is a reciprocal concept of the charge current. We usually do not care about spin states of carriers of charge current in paramagnetic materials. What matters is only the charge and momentum of the carrier. Even if we can distinguish current carried by up-spin electron ($j_\uparrow$) from that by down-spin electron ($j_\downarrow$), charge carrier is just the sum of the two ($j_c = j_\uparrow + j_\downarrow$). On the other hand, spin current is defined as difference of the two ($j_s = j_\uparrow - j_\downarrow$). In ferromagnetic materials, there is the difference between the number of up-spin electrons and down-spin electrons. Therefore, the charge current accompanies spin current in ferromagnetic materials. Since the number of up-spin electrons equals to that of down-spin electrons in paramagnetic (or normal) conductors, the spin current in such materials is usually zero. However, there are some methods to generate population difference between the up-spin and down-spin carriers in normal conductors.

One of them is the spin injection from ferromagnetic materials. Figure 1.3 depicts a typical device for this experiment. When current is flow from the ferromagnetic material (F) into normal material (N), the spin polarization (difference of electrochemical potential between up- and down-spin electrons) can be injected from F to N. Once spin polarization is generated in N, spin current can flow by diffusion. The spin polarization traveled by spin current can be detected as a voltage between two ferromagnetic probes. Because there is no spin polarization in N at thermal equilibrium, generated polarization is diffused accompanying the relaxation. In this sense, the spin current is not conserved in N, while the charge current is always conserved. The characteristic length of this diffusion is called spin diffusion length or spin relaxation length. When the spin current is flowing without accompanying charge current (where $j_\uparrow = -j_\downarrow$), this is called pure spin current. Pure spin current can transfer the information without charge current and Joule heating, although the length of such transfer is limited by the spin relaxation length. For this kind of spin current based electronics or spintronics, a normal conductor with a long spin relaxation length is required.

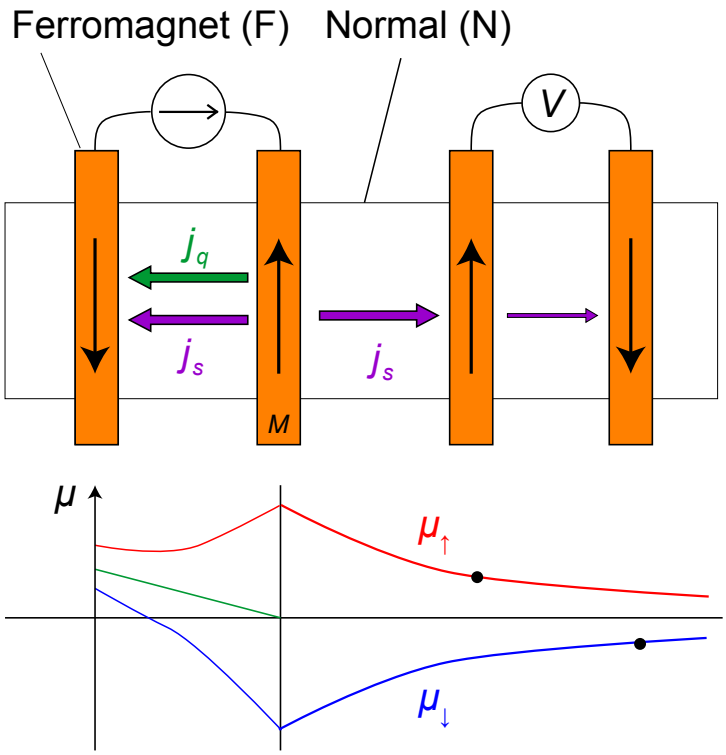

Figure 1.3: Schematic of the four terminal spin valve device for spin current injection and detection experiments in normal conductor. Lower panel shows electrochemical potentials for up- and down-spin electrons for each position.

Graphene as spin current conductor

Since spin relaxation length has correlation with carrier mobility, graphene has been expected to be a good conductor of spin current. A large number of experimental works have demonstrated the spin current generation and detection in graphene, and characterized graphene's parameter like spin relaxation length.[34–39] Graphene shows rather high spin relaxation lengths of several microns in these experimental works, however, these are not as high as the values predicted by intrinsic property of graphene. A simple consideration of Elliot-Yafet mechanism results in an estimated spin relaxation time of $\sim$ 50 ns and a length of $\sim$ 300 μm.[40] Because there is about two-orders difference between experimentally and theoretically estimated values above, some other mechanisms should be limiting the spin relaxation.

Several theories suggest that impurity related effects can be a limiting mechanism of spin relaxation, which includes enhancement of local spin orbit interaction and scattering at magnetic impurities.[41, 42] Thus, it is physically important to explore spin relaxation of graphene with impurities. Not only physical importance, there should be a chance to control and engineer the spin relaxation with impurities, if the relaxation is limited by impurities. In chapter 4, we show some evidences for this kind of spin relaxation control by impurities through magnetotransport measurements of fluorinated graphene.

1.4.2 Spin Hall effect in graphene

Recent studies revealed that adatom impurity not only impose electron spin relaxation in graphene, but also has possibility to generate a more positive effect. It can be an extrinsic source of the spin Hall effect by resonant skew scattering.[43, 44] In this section, we briefly review the concept of spin Hall effect, and previous studies of spin Hall effect in graphene.

The spin Hall effect

The spin Hall effect is the effect which converts a charge current into transverse spin current. A conceptual explanation of the extrinsic spin Hall effect is as follows. Let us assume there are some impurities in conductor which deflects up-spin carrier to the left, and down-spin carrier to the right. When a charge current is applied along one direction, on average, the up-spin current flows to the left and the down-spin current flows to the right. As a result, a spin current is generated along the

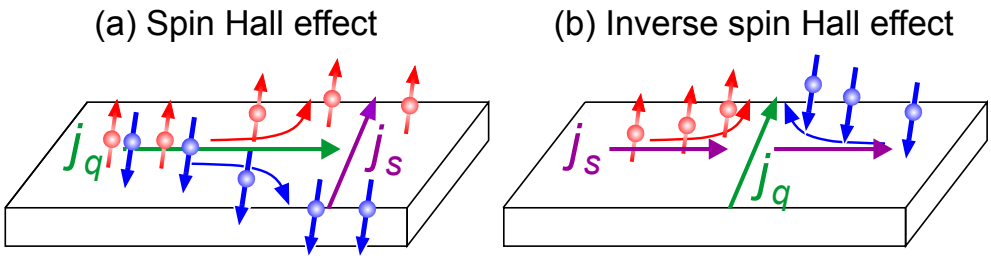

Figure 1.4: (a) Schematic showing concept of spin Hall effect. (b) Schematic showing concept of inverse spin Hall effect.

transverse direction of the charge current as depicted in Fig. 1.4. The same physics converts a spin current into a transverse charge current as well. This reciprocal effect is called the inverse spin Hall effect.

The inverse spin Hall effect can be observed, for instance, by using a device called Hall cross shown in Fig. 1.5. Spin current is generated by spin injection from ferromagnets. And then if there is inverse spin Hall effect in normal conductor, a voltage is observed between the probe electrodes. More simple experiment can be done without using ferromagnets as shown in Fig. 1.6. A charge current across a terminal pair of the Hall bar is converted into spin current, and then converted again into charge current. The charge current is detected by voltage between another terminal pair (voltage probe). This setup is very simple, however, may suffer from artifact due to inhomogeneous resistivity in normal conductor.

The spin Hall effect has been observed in various conductors including both metal and semiconductor.[45, 46] The conversion efficiency of a charge current into spin current is called spin Hall angle. This value has been known to be relatively large in metal (order of 0.01 in Pt[45] and 0.1 in Ta[47]), and small in semiconductor (order of 0.0001 in Si[46]). It is physically important and interesting to explore the spin Hall effect in graphene, which is a conductor with characteristics of both metal and semiconductor. If large spin Hall effect can be observed in graphene, spin current can be generated without ferromagnetic junctions, and pure-graphene spintronics device can become plausible.

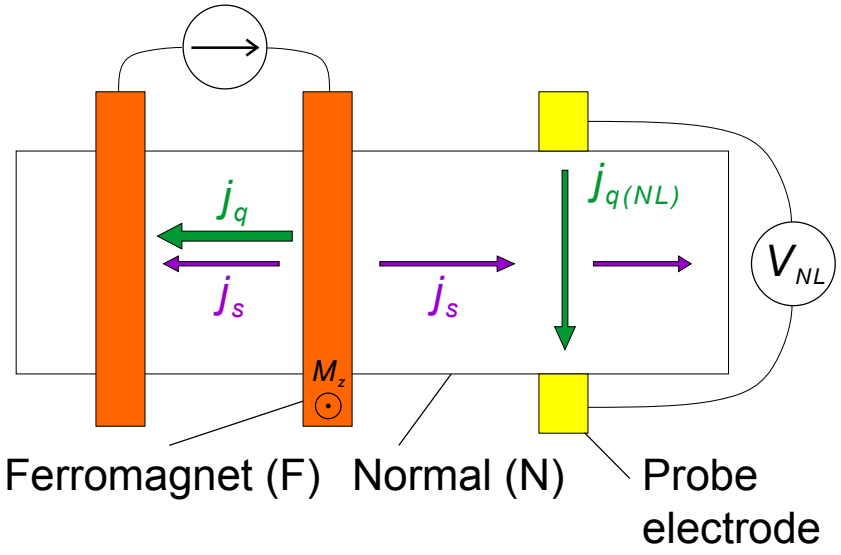

Figure 1.5: Device structure and experimental setup for observation of inverse spin Hall effect using the Hall cross device.

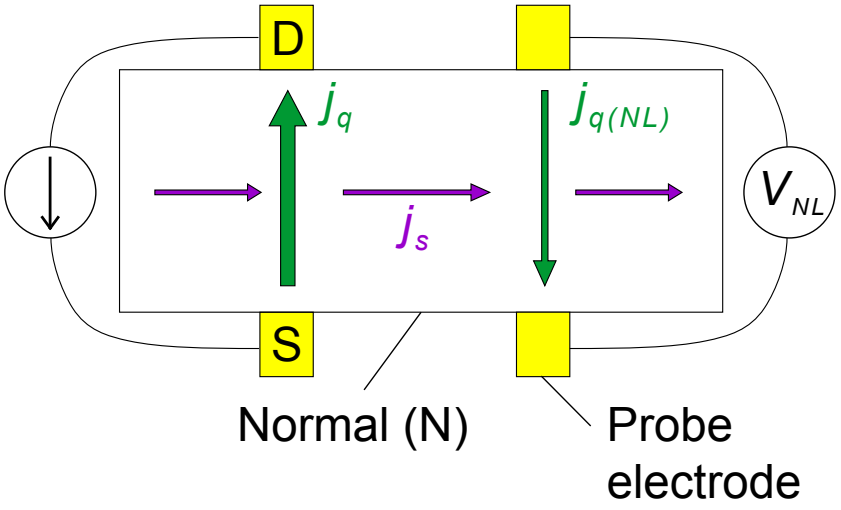

Figure 1.6: Device structure and experimental setup for observation of inverse spin Hall effect using the Hall bar device.

Extrinsic spin Hall effect in graphene

Very recently, both theory[44, 48] and experiments[43, 49] have shown that large extrinsic spin Hall effect can be observed in graphene with hydrogen adatoms. The observed effect is strong, having spin Hall angle with magnitude of the same order as, or even larger than, that in metal. Exploring the spin Hall effect for the case of fluorine adatoms is important to show the difference of observed spin Hall effect when resonant impurity level is changed. In chapter 4, we show the results of the trials to observe spin Hall effect in dilute fluorinated graphene.

1.5 Nitrogen-vacancy color center in diamond

1.5.1 Energy level structure

The nitrogen-vacancy color center (NV center) in diamond is one of various color centers in diamond. An NV center consists of a substitutional nitrogen and adjacent vacancy, as shown in Fig. 1.7 (a). There are five unpaired electrons attributed to one NV center: three as carbon atoms' dangling bonds and two as nitrogen's dangling bond. The neutral NV (NV^0) center is one stable charge state, however, negatively charged NV (NV^-) center is more important because optical initialization and readout of spin state can be performed. Hereafter, we denote NV^- center by just writing NV center.

NV^- center consists of six electrons. The electronic structure is calculated by first principles molecular orbital theories.[50, 51] Four electrons fill highly localized molecular orbitals in between the bandgap of diamond, while two electrons always fill a low-lying molecular orbital in valence band of diamond. Total energy level structure is constructed by symmetrizing linear combination of four electrons' orbital configurations including spin states.

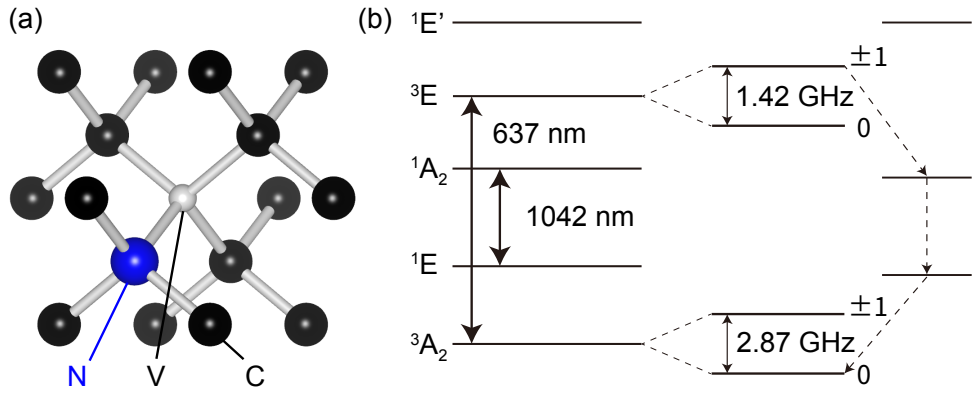

Figure 1.7: (a) Structural model of NV center in diamond. (b) Energy level structure of NV center.

Simplified energy level structure of NV^- center is shown in Fig. 1.7 (b). The ground state ($^3A_2$) and first excited (^3E) state are triplet states ($S = 1$), and the energy difference is 637 nm. Photoluminescence spectrum with zero phonon line at this energy is experimentally observed. There is meta-stable singlet state ($S = 0$) between the ground state and first excited state. One of

the most important properties of the NV center, optical spin polarization, is mediated by this singlet state. Electrons with $|m_s = \pm 1\rangle$ states have certain probability to decay through this singlet state to the $|0\rangle$ ground state. Although infrared light (1042 nm) is actually emitted, the energy is much different from direct luminescence (transition from ^3E to $^3A_2$). Thus, this decay is sometimes called non-radiative decay. Due to this property, continuous optical pumping result in spin polarization into the $|0\rangle$ state. Furthermore, spin state population can be read out optically, by observing photoluminescence intensity. The more $|0\rangle$ state is populated, the more intense luminescence is observed.

1.5.2 Ground state spin Hamiltonian

The spin state population can also be controlled by resonant microwave radiation, or electron spin resonance (ESR). The optically detected magnetic resonance (ODMR) at room temperature can be performed by combination of optical spin state polarization-readout and ESR. Although ODMR experiments can be done using either the ground state or excited state, the use of the ground state spin is more popular because it is simpler and more efficient. So we will focus on the spin state of ground state.

The full spin Hamiltonian of the NV ground state can be written as[52]

$$\hat{H}_{gs} = \left(D_{gs} + d_{\parallel}\Pi_z\right) S_z^2 + \mu_B \boldsymbol{S} \cdot \bar{\boldsymbol{g}} \cdot \boldsymbol{B} - d_{\perp}\Pi_x \left(S_x^2 - S_y^2\right) + d_{\perp}\Pi_y \left(S_x S_y + S_y S_x\right), \tag{1.1}$$

where $D_{gs} = 2.87$ GHz, μ_B, $\boldsymbol{B}$ are zero field splitting, Bohr magneton, and external magnetic field, respectively. $\boldsymbol{\Pi} = \boldsymbol{E} + \boldsymbol{\sigma}$ is sum of external electric field ($\boldsymbol{E}$) and local strain field ($\boldsymbol{\sigma}$) of the NV center.

Since the effect of magnetic field is much larger than other fields and we are interested in magnetometry applications, we simplify the Hamiltonian by dropping $\boldsymbol{\Pi}$ as follows.

$$\hat{H}_{gs} = D_{gs} S_z^2 + \mu_B \boldsymbol{S} \cdot \bar{\boldsymbol{g}} \cdot \boldsymbol{B} = D_{gs} S_z^2 + \mu_B g_{\parallel} S_z B_z + \mu_B g_{\perp} (S_x B_x + S_y B_y) \tag{1.2}$$

When perpendicular field is small enough ($\mu_B g_{\perp} \sqrt{B_x^2 + B_y^2} \ll D_{gs}$ and $\mu_B g_{\perp} \left(B_x^2 + B_y^2\right) \ll D_{gs} \mu_B g_{\parallel} B_z$), eigenenergies of this Hamiltonian can be approximated as

$$E_{\pm} = D_{gs} \pm \mu_B g_{\parallel} B_z. \tag{1.3}$$

Thus, the energy levels (splittings) is determined only by B_z. Strictly speaking, D_{gs} has temperature dependence and the NV center can be utilized as a temperature sensor as well, however, we ignore this effect and treat D_{gs} as a constant.

1.5.3 Using spin state as two level system, or qubit

The NV ground state is spin triplet ($S = 1$) and of course has three states. However, if virtually only two of three states are populated, subspace of $S = 1$ can be regarded as a two level system. Matrix elements of spin operator for spin-1 system can be written, taking basis $\{|1\rangle, |0\rangle, |-1\rangle\}$, as

$$S_x = \frac{1}{\sqrt{2}}\begin{pmatrix} 0 & 1 & 0 \\ 1 & 0 & 1 \\ 0 & 1 & 0 \end{pmatrix}, S_y = \frac{1}{\sqrt{2}}\begin{pmatrix} 0 & -i & 0 \\ i & 0 & -i \\ 0 & i & 0 \end{pmatrix}, S_z = \begin{pmatrix} 1 & 0 & 0 \\ 0 & 0 & 0 \\ 0 & 0 & -1 \end{pmatrix}, \tag{1.4}$$

For example, we can write two dimensional subspace on basis $\{|0\rangle, |-1\rangle\}$ as

$$S_x = \frac{1}{\sqrt{2}}\sigma_x, S_y = \frac{1}{\sqrt{2}}\sigma_y, S_z = \sigma_z - \frac{1}{2} \tag{1.5}$$

where σ_i $(i = x, y, z)$ are Pauli matrices. This is same as $S = 1/2$, with non-essential addition of constants.

Once the system is regarded as a two level system or a qubit, we can introduce Bloch sphere notation to visualize the spin states. We write arbitrary state of the two level system as

$$|\psi\rangle = \cos(\theta/2)\,|0\rangle + e^{i\phi}\sin(\theta/2)\,|-1\rangle\,. \tag{1.6}$$

In Bloch sphere notation, this state is represented as a unit vector in Fig. 1.8. Here θ characterizes the population difference between the two states and ϕ, the phase difference.

1.5.4 Spin state control by external field

Let us discuss the dynamics of spin states described by spin Hamiltonian Eq. 1.2 under external magnetic field $\boldsymbol{B} = (B_1\cos(\omega_{MW}t + \phi_{MW}), -B_1\sin(\omega_{MW}t + \phi_{MW}), B_0)$. First we consider the case without rotating magnetic field ($B_1 = 0$). In this case the state can be written as

$$|\psi(t)\rangle = \cos(\theta/2)\,|0\rangle + e^{i(\phi_0 - \omega_0 t)}\sin(\theta/2)\,|-1\rangle, \omega_0 = D_{gs} - \mu_B g_{\parallel} B_z. \tag{1.7}$$

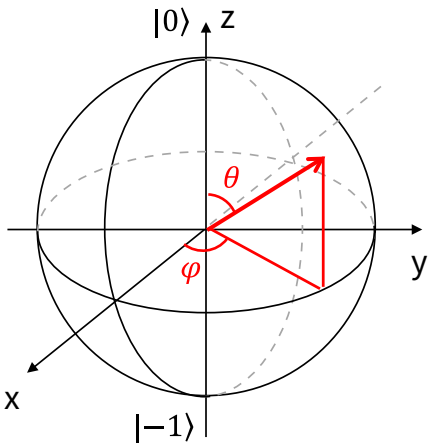

Figure 1.8: The Bloch sphere notation of two level system.

The phase difference is rotating at a fixed angular frequency ω_0 in this situation. This rotation depicted in Fig. 1.9 is called Larmor precession. Hereafter, we can set $\phi_0 = 0$ without loss of generality. Next step, we introduce rotating magnetic field and move onto rotating frame where the coordinate is rotating about z-axis at ω_{MW}. Let us consider the case $\omega_{MW} = \omega_0$. In this case ESR is on perfect resonance, and Larmor precession is apparently stopped on rotating frame. We shall skip the calculations here and write the answer as follows. (Calculation details are given in Appendix A.1).

$$|\psi(t)\rangle = \cos(\omega_1 t)\,|0\rangle + e^{-i(\phi_{MW}+\frac{\pi}{2})}\sin(\omega_1 t)\,|-1\rangle, \tag{1.8}$$

$$\omega_1 = \frac{\mu_B g_\perp}{\sqrt{2}} B_1. \tag{1.9}$$

We can see that we can tune the spin state's population using rotating magnetic field. This is the essence of ESR, and the oscillatory behavior is called Rabi oscillation or Rabi nutation.

1.6 Pulse ODMR and quantum sensing

We have seen in the previous section that the NV center can work as a spin-based qubit in solid equipped with optical polarization and readout capabilities. The NV center is not "one of a kind" being this type of qubit.[53–57] However, the NV center is for now one of the most deeply understood and promising qubits for applications. There are broad range of applications including

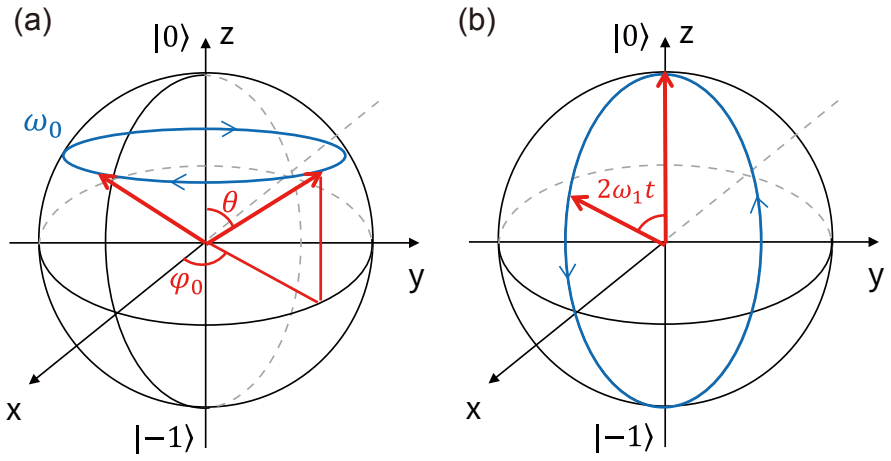

Figure 1.9: Bloch sphere notation of (a) Larmor precession and (b) Population oscillation (Rabi oscillation) by ESR in case $\phi_{MW} = -\pi/2$.

quantum computing and communication.[58–61]

In this thesis, we will focus on the quantum sensing (magnetometry) applications.[62–64] The solid state's defect-based qubits, aside from photon-based, gaseous atom-based or superconductor flux-based qubits, are the most suitable for this application because of their atomic-scale size and the position-control capabilities. Actually, the NV center has been demonstrated as a good quantum sensor which has both high sensitivity and spatial resolution. However, due to diamond's unique property, there appears to be many room for improvements and engineering. In this section we start by describing basic principle and method for the sensing, and introduce problems-to-be-solved to achieve better performance.

First, we shall introduce basic principles of the quantum sensing. We will focus on sensing only the magnetic field throughout this part, though sensing of electric field and mechanical movement is also feasible. The simplest description of sensing principle is "find the resonant frequency" (or energy). Equation 1.3 show the direct connection between external field (B_z) and the resonant frequency ($E_\pm$). The simplest method to find the resonant frequency of ODMR is observing the spectrum of continuous wave (CW) ODMR. We can actually sense magnetic field of order of millitesla by CW-ODMR. However, this method suffer from finite line width of the spectrum and not very efficient in terms of acquisition time. Some methods based on pulse ODMR is used for the sensing of much smaller fields.

1.6.1 Free induction decay

The simplest method amongst pulse ODMR sensing is called free induction decay (FID). Figure 1.10 shows a sequence of the FID measurement. One shot measurement starts with a laser pulse for spin-state initialization. As stated in Sec. 1.5.1, long enough optical pumping (laser irradiation) can polarize the spin-state into $|0\rangle$.

Next, resonant microwave pulse named $\pi/2$-pulse is applied. A resonant microwave can rotate the Bloch vector following Eq. 1.9. To realize $\pi/2$ pulse, we choose microwave power (B_1) and pulse width ($t_{\pi/2}$) to satisfy $2\omega_1 t_{\pi/2} = \pi/2$. The Bloch vector is flipped by $\pi/2$ and now lying on xy plane. In other words, the state becomes equal superposition of the two states which can be written as

$$|\psi\rangle = \frac{1}{\sqrt{2}}|0\rangle + \frac{1}{\sqrt{2}}|1\rangle . \tag{1.10}$$

(Note: In order to set the initial phase to be zero, we have determined to measure the phase difference as the angle between Bloch vector and y-axis. This definition is different (by $\pi/2$) from equations in previous section. We have also changed a ket from $|-1\rangle$ to $|1\rangle$ for simplicity, because the discussion below can be applied to either of the qubit using $\{|0\rangle, |-1\rangle\}$, or $\{|0\rangle, |1\rangle\}$.)

After that the qubit is freely evolved for certain time τ, which is called free evolution time. During this time state will acquire some phase difference. Because we are on the frame rotating at angular frequency ω_{MW}, precession at this frequency does not result in any movement of Bloch vector. This is the case for perfect resonance ($\omega_0 = \omega_{MW}$). When there is additional small external field (b_z) to be observed, ω_0 is detuned to be $\omega_0 = \omega_{MW} - \gamma b_z$. Here we have rewritten $\mu_B g_\parallel$ as γ. γ is called gyromagnetic ratio and has the value of $\gamma = 2\pi \times 28$ GHz/T. If we assume that b_z is constant during free evolution time, the Bloch vector will rotate at fixed angular frequency γb_z in rotating frame. The phase difference is accumulated for τ to finally become $\Delta\phi = \gamma b_z \tau$. The state just after free evolution is written as

$$|\psi\rangle = \frac{1}{\sqrt{2}}|0\rangle + \frac{e^{i\Delta\phi}}{\sqrt{2}}|1\rangle . \tag{1.11}$$

This accumulated phase difference is converted into population difference by another microwave $\pi/2$ pulse. In terms of equation the state will become

$$|\psi\rangle = \sin\left(\frac{\Delta\phi}{2}\right)|0\rangle + \cos\left(\frac{\Delta\phi}{2}\right)|1\rangle . \tag{1.12}$$

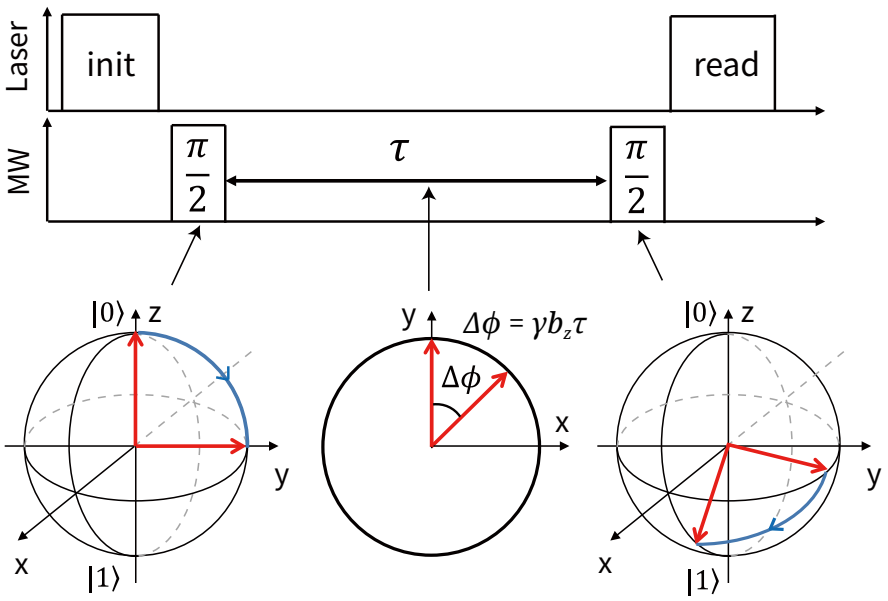

Figure 1.10: Laser and microwave pulse sequence of the FID measurement.

This population difference can be read out by observing photoluminescence intensity under another laser pulse.

1.6.2 Decoherence

Since phase difference is proportional to external field of interest (b_z) and free evolution time (τ), τ should be large enough to sense small b_z. However, in realistic situation this τ cannot be determined arbitrarily because there is decoherence or dephasing.

The NV spin is surrounded by another spins including nuclear spin (typically ^{14}N or ^{13}C) or electron spins (attributed to P1 center for example). Even if there is no additional external field (b_z), NV spin will interact with these spin environments. We can expect random (undesirable) phase accumulation, over certain time scale, from these interaction. The randomly acquired phase results in random distribution of Bloch vector in xy plane, or shortening of "averaged" Bloch vector as depicted in Fig. 1.11. When we are using multiple (ensemble) NV centers, we are always measuring this averaged Bloch vector. Even in the case we are using only one (single) NV center, Bloch vector is ensemble-averaged because we usually repeat the measurement cycle (typically for over 10^5 times) and take average to get enough signal to noise ratio. Therefore, shortening

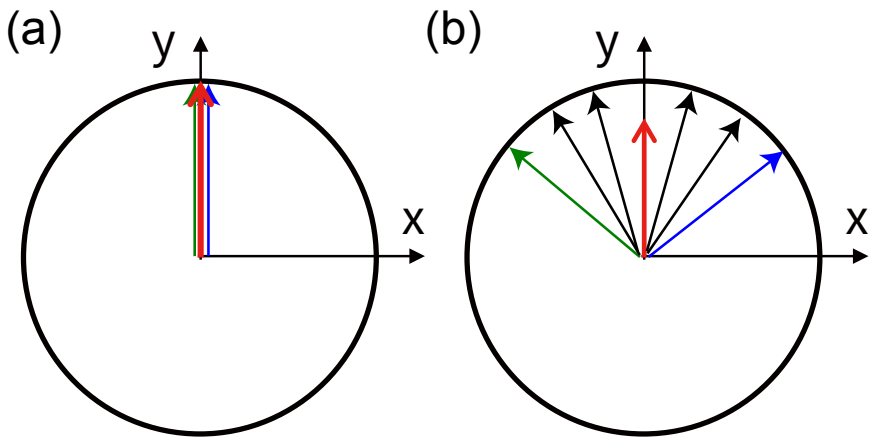

Figure 1.11: Schematic figure of decoherence. (a) If there is no decoherence, the spin state is fixed along y-axis in rotating frame. (b) Random distribution of Bloch vector (decoherence) results in shortening of averaged Bloch vector (arrow in red along y-axis).

of averaged Bloch vector, or decoherence, results in the loss of measurement contrast. We have to choose the evolution time τ which is enough shorter than, or comparable to, the time scale of decoherence (coherence time).

The contribution to decoherence is not only the spin environment around NV center. One important source of decoherence is magnetic field inhomogeneity. When ensemble NV centers are spreading over large volume, the static magnetic field B_z (or resonant frequency) of each NV center can be different from one to another. Since microwave frequency is fixed, random distribution of B_z means random detuning, or random movement of Bloch vector in xy plane. This is well-known problem for instrumentation of conventional ESR or nuclear magnetic resonance (NMR) system. These instruments are designed to apply static magnetic field as uniformly as possible to the sample. Any other source of resonant frequency change or distribution (over either space or time) can contribute to the decoherence.

1.6.3 Spin echo

The effect of decoherence can be partially removed by using spin echo technique. Difference between spin echo and FID is only microwave pulse sequence. In spin echo, free evolution is divided into two by π pulse as shown in Fig. 1.12. Spin echo can remove the effect of decoherence

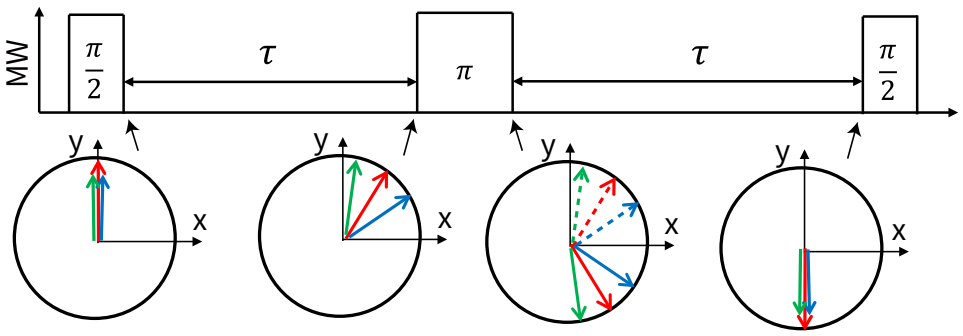

Figure 1.12: Microwave sequence of spin echo measurement.

due to static (or low enough frequency) source such as inhomogeneous magnetic field. At the end of half of free evolution, there might be decoherence. The π pulse flips all the spin states around x-axis. If each spin's angular frequencies during first and second half of the evolution is the same, all the Bloch vector will get together (make the spin echo) along -y-axis at the end of total evolution.

Note here that spin echo filters out constant movement of averaged Bloch vector as well (depicted as red arrow in Fig. 1.12). So we cannot apply this technique for detection of constant (DC) magnetic field (b_z). On the other hand, we can effectively detect alternating (AC) b_z if the AC frequency is matching with free evolution time. Figure 1.13 clarify the difference between DC and AC fields. While the effect of DC field is filtered out as stated, AC field alters the sign at π-pulse and move the Bloch vector toward opposite direction during the second half. The final state of the spin echo has information of AC field in phase difference:

$$\Delta\phi = \int_0^{\tau} b_z(t)dt - \int_{\tau}^{2\tau} b_z(t)dt \tag{1.13}$$

1.6.4 Dynamical decoupling

The spin echo sequence is not always perfect for sensing of small AC magnetic field. Since equation 1.13 can be maximized when $\tau = 1/2f$, available evolution time is limited by the frequency of AC field. We have to set the evolution time for high frequency signal that might be unnecessarily shorter than coherence time. We can choose longer evolution time per one measurement shot, by introducing multi-pulse extension of the spin echo called dynamical decoupling sequences. Figure 1.14 shows pulse timings of Car-Purcell-Meiboom-Gill (CPMG) type pulse sequences.

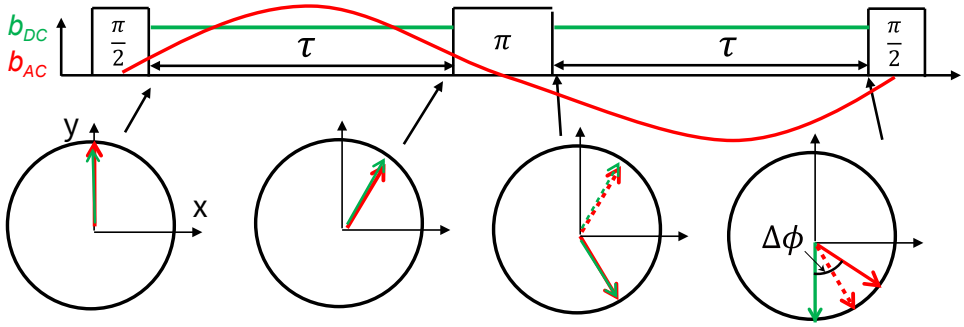

Figure 1.13: Effect of DC and AC external field onto spin echo.

Historically, this technique has been developed for relaxation experiments in conventional pulse NMR. And recently, it has been applied to pulse ESR of spin-based qubits like NV center and semiconductor quantum bit. As in the figure, this sequence consists of equally separated (by τ) multiple π pulses. We denote the number of π pulses by N hereafter. Even though we should choose $\tau = 1/2f$ according to AC field frequency, however, we can elongate the total evolution time by increasing N. The longer N we use, the more phase $\Delta\phi$ we acquire, leading to better sensitivity. But there is a limitation by decoherence again. We note here just we can choose N such that τN becomes comparable to NV coherence time. The detailed discussion will be in Chapter 7.

There are some variations regarding microwave phase among CPMG type dynamical decoupling sequences, though timings are same for all. The simplest case is called Car-Purcell (CP) sequence.[65] In this sequence the microwave phase is unique for all pulses including $\pi/2$ pulses. On the other hand, CPMG uses two quadrature microwaves.[66] We shall think of initial $\pi/2$ pulse has a phase such that rotate the Bloch vector around x-axis in our rotating frame (as in Fig 1.10) This pulse will be denoted as $\pi/2_x$ pulse. For subsequent π pulses we use microwave with 90°-shifted phase, which rotates Bloch vector around y-axis ($\pi/2_y$ pulses). Meiboom and Gill have found that this change can compensate the effect of pulse imperfection and avoid extrinsic signal loss. Further variation includes more complicated phase modulations. Here we introduce XYn type sequences.[67] XY4 sequence repeats π pulse trains with phase x-y-x-y, while XY8 repeats x-y-x-y-y-x-y-x. Although the degree of freedom for N is reduced (we can only choose N being integer multiple of 4(8) for XY4(8)), it is found that these sequence is suitable for sensing application because of its effective pulse-imperfection compensation especially under non-zero

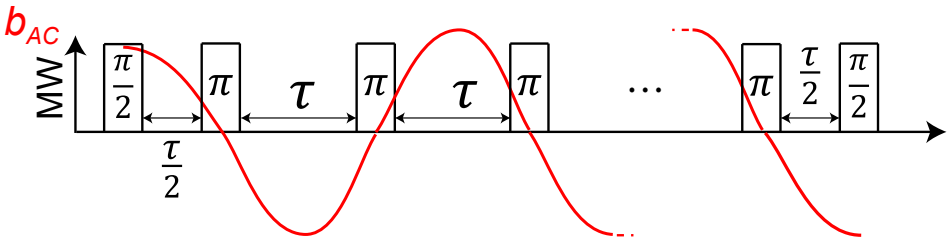

Figure 1.14: Microwave pulse timings of CPMG-type dynamical decoupling sequences.

total phase accumulation.

1.6.5 Sensitivity limit

We have briefly reviewed pulse ODMR method for the sensing above. We have to use FID method for DC field sensing, while we can get a better performance by using spin echo or dynamical decoupling for AC field sensing. As we have already seen, the difference of each method is basically available total free evolution time per single shot measurement, which we hereby denote with τ_{tot}. τ_{tot} should be large for sensing of small field because the phase difference acquired per single shot measurement will be $\Delta\phi \sim \gamma b_z \tau_{tot}$. However, τ_{tot} is limited by decoherence effect and optimized value is order of the "apparent" coherence time, which is dependent on measurement scheme. Coherence time is usually written as T_2^* (T_2) for FID (spin echo).

Here we shall discuss the sensitivity limits. The sensitivity is limited by quantum projection noise and photon shot noise. Quantum projection noise comes from the uncertainty of reading acquired phase ($\Delta\phi$).[68] This uncertainty is assumed to roughly 1 radian of uncertainty per measurement shot.[63] We define the minimum detectable field (B_{min}), which will be $B_{min} \sim 1/\gamma\tau_{tot}$ per measurement shot. The sensitivity is normally characterized as the minimum detectable field per unit acquisition time T. Because we can repeat roughly T/τ_{tot} measurements in a given acquisition time T, we increase sensitivity by $\sqrt{\tau_{tot}/T}$. Projection noise limited sensitivity (η_{proj}) can be written as

$$B_{min} \sim \frac{1}{\gamma\tau_{tot}}\sqrt{\frac{\tau_{tot}}{T}} = \frac{1}{\gamma\sqrt{\tau_{tot}T}}, \tag{1.14}$$

$$\eta_{proj} \sim B_{min}\sqrt{T} = \frac{1}{\gamma\sqrt{\tau_{tot}}} \left(\mathrm{T}/\sqrt{\mathrm{Hz}}\right) \tag{1.15}$$

There is further limitation for the sensitivity, the photon shot noise. The signal to noise for photon shot noise scales as $\sim 1/\sqrt{N_{photon}}$, where N_{photon} is number of collected photons. Sensitivity is also limited by the photon contrast to read the spin state. As stated in Sec. 1.5.1, spin state can be read out by photoluminescence intensity being higher for $|m_s = 0\rangle$ than $|m_s = \pm 1\rangle$. This difference is not perfect and typically has contrast of 30 % (intensity is about 70 % for $|m_s = \pm 1\rangle$ state compared to $|m_s = 0\rangle$). Total sensitivity limit combining the projection noise and the shot noise can be written as

$$\eta \sim \frac{1}{\gamma C \sqrt{n \tau_{tot}}} \left(\mathrm{T}/\sqrt{\mathrm{Hz}}\right) \tag{1.16}$$

where n is photon collection rate (number of photons collected per one measurement shot) and C is the contrast as stated above. Although Eq. 1.16 is an order estimate of achievable sensitivity, we can use this as a guide for the sample design.

1.7 CVD-based design of NV-containing diamond for quantum sensors

In the previous section we have introduced the working principle and the sensitivity limitation of NV spin quantum sensors. Methods to intentionally create NV centers in diamond is divided into two groups, irradiation and grown-in. Irradiation type methods are ion-implantation and electron beam irradiation. Since the position control is relatively easy, ion-implantation has been the most widely used for sensing below microscopic scale. However, ion-implantation will usually suffer from substantial damage of diamond lattice by high energy ion collisions, leading to short coherence time. The best choise for maximizing the coherence time is the grow-in NV center, which is incorporated during chemical vapor deposition (CVD) diamond growth. It is known that spin echo coherence time T_2 of $\sim 600\mu$s is available in the high-purity CVD diamond.[69–71] This limit is set by nuclear spin bath of ^{13}C with natural abundance (1.1 %). Further coherence time up to a few milliseconds is possible by isotopic engineering (reducing ^{13}C concentration).[72]

There are almost no preceding research of the high density nitrogen doping during CVD growth for NV quantum sensors, especially for (111) oriented diamond. In this thesis we will explore the capability of this technique. It is straightforward that the high density NV center will result

in high photon emission rate (n in Eq. 1.16) and sensitivity.[73] Although spatial resolution is reduced compared to the case of single NV center (nm-scale resolution is feasible), high density NV ensemble layer is suitable for imaging application at optical diffraction limit of μm-scale. Throughout this thesis, we will use the term 'ensemble' to denote the dense ensemble of NV centers, each of which cannot be resolved by diffraction-limited optics ($\gg 10^{12}$ centers/cm^3).

1.7.1 Photon collection efficiency

There is a problem regarding a intrinsic optical property of diamond. The photon collection efficiency from the NV centers in the bulk diamond is low due to the high refractive index (2.4) of diamond. Improvement of photon collection efficiency increases n in Eq. 1.16 and therefore has direct impact on sensitivity. High refractive index also means that diamond can work as an effective light wave guide in low refractive index environments. In order to exploit this property and improve the photon collection efficiency, pillar-shaped micro-structures fabricated by top-down lithography and etching have been intensively studied.[74–80] However top-down lithography may suffer from etching-induced damage. We will introduce a new CVD-based micro-structure for photon collection efficiency enhancement in chapter 5.

1.7.2 Selective alignment

NV centers can be formed along four equivalent $\langle 111 \rangle$ crystallographic axes due to its structural symmetry. This intrinsic inhomogeneity degrades the measurement contrast of ODMR because the change of energy levels depends on the angle between external field and NV center's symmetry axis.[52] Assuming the alignment of NV centers is randomly distributed, we can make use of only 25% of the NV centers for a measurement. This partial measurement degrades the measurement contrast (C in Eq. 1.16). If NV centers are selectively aligned along preferred axes, a larger subset of the NV centers can be utilized and a better contrast can be achieved. Such a selective alignment is realized for grown-in NV centers in CVD diamond. For (110) and (100) substrates, NV centers can be aligned along two out of the four axes, reaching a selective alignment of 50%.[81, 82] Recent studies have revealed that in CVD-grown (111) diamond, selectivity becomes almost perfect ($\geq$ 94%) along the [111] direction.[83–85] A high alignment ratio of 73% is also obtained using (113) oriented substrates, which is more stable than (111) substrates and suitable

for the growth of thick films.[86] These studies mainly focused on NV centers with relatively low density, where single NV centers can be resolved optically ($\sim 10^{12}$ centers/cm^3). We are interested in sensing applications at relatively large (μm) scale and require high density NV ensemble where large number of NV centers are in a diffraction limited spot. However, the selective alignment of such high density ensemble has not been explored. In chapter 6, we will show the results of fabrication and characterization of this kind of selectively-aligned and high-density NV ensemble in CVD-grown (111) diamond. And then, we demonstrate the AC magnetometer (quantum sensor) action of the samples in chapter 7.

Chapter 2

Fluorination of graphene

Toward the control of charge and spin transport in graphene, we started by establishing the method for controllable fluorination of graphene. In this chapter, we will show the fluorination method using Ar/F_2 plasma and the characterization of fluorinated graphene using Raman spectroscopy and X-ray photoelectron spectroscopy (XPS).

2.1 Graphene samples

Graphene samples for Raman spectroscopy were prepared by the mechanical exfoliation from Kish graphite onto SiO_2 (285 nm)/Si substrate. Mono- and bi-layer graphene were identified by optical microscopy (Fig. 2.1 (a)) and Raman spectroscopy. For XPS analysis, we used large-size CVD-grown monolayer graphene on a Cu foil as in Fig. 2.1 (b) and (c). Fluorination of such a large graphene was also done after transferring onto a SiO_2/Si substrate. We confirmed that more than 90 % of graphene area was monolayer by using optical microscopy and Raman spectroscopy after the transfer.

2.2 Fluorination using Ar/F_2 plasma

An reactive ion etching (RIE) system shown on Fig. 2.2 was used for plasma fluorination of graphene. The graphene samples were exposed to Ar/F_2 (90% / 10%) plasma with a relatively low RF power of 5 W, a gas pressure of 0.1 Torr, and a total gas flow rate of 75 sccm at room

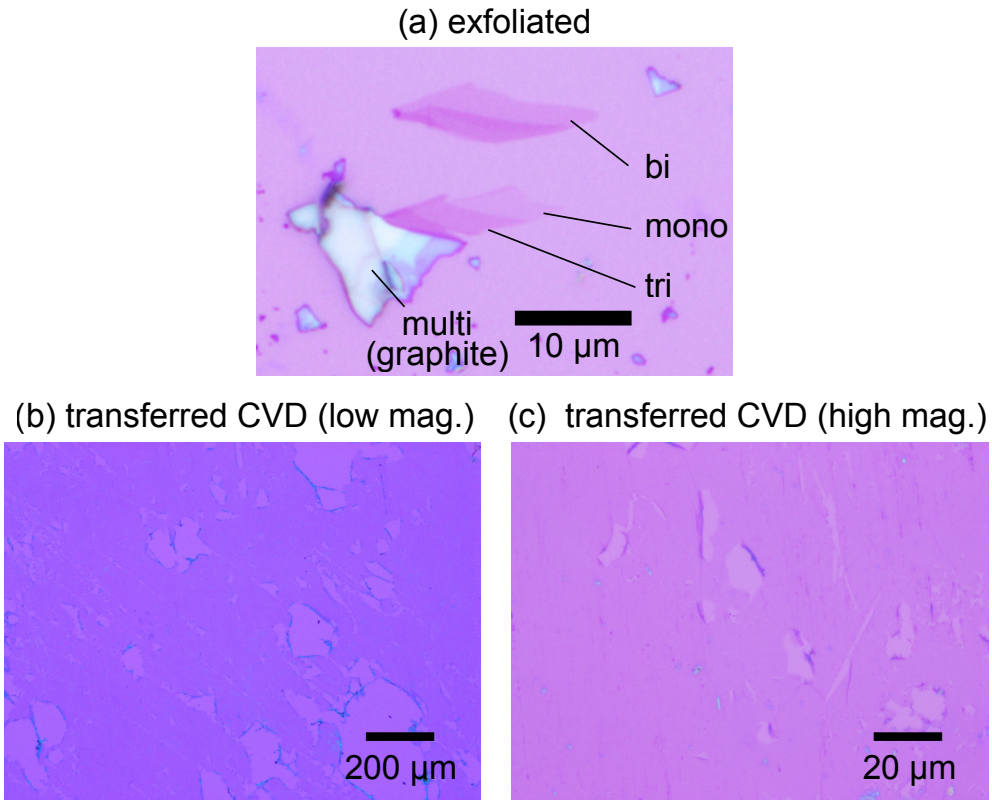

Figure 2.1: Optical micrograph of graphene samples on SiO_2 substrate prepared by (a) mechanical exfoliation (b) and (c) transfer of CVD-grown graphene on Cu foil.

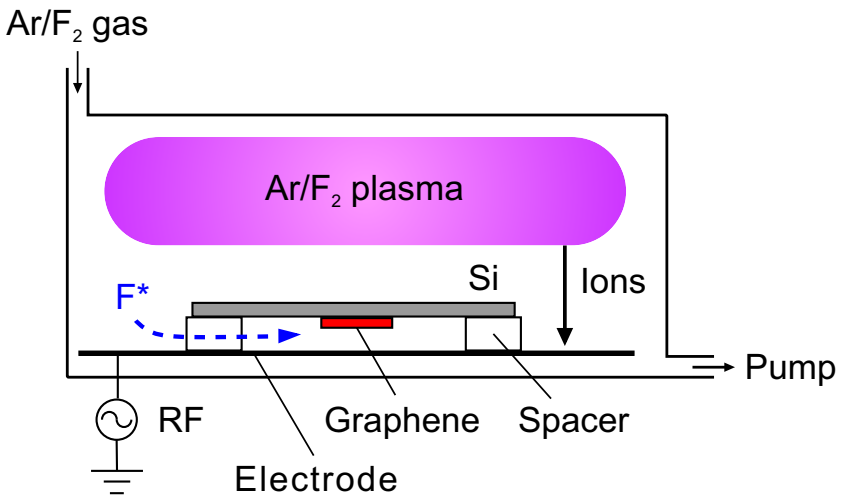

Figure 2.2: Schematic view of RIE system used for fluorination of graphene.

temperature. The reaction time ranged from 0.5 to 30 min. We characterized Ar/F_2 plasma by using optical emission spectroscopy. The emission signals of 686 nm and 704 nm originating from fluorine were observed. To suppress the effect of ion bombardment to graphene, the substrate was placed "face down" (graphene face toward the bottom electrode) using ceramic spacers. This configuration makes the reaction by fluorine radicals (F*) dominant over charged fluorine and argon ions. The effect of the face down setup will be discussed later (Section 2.3).

2.3 Raman spectroscopy analysis

2.3.1 Evolution of Raman spectra with reaction time

Raman measurements were done using a micro-Raman system with a solid-state green laser (532 nm). The spot size was about 1 μm and the laser power was kept below 1 mW to avoid laser-induced damage or heating. Figure 2.3(a) shows Raman spectra of monolayer graphene before and after fluorination for different duration. Two pronounced peaks are observed in the spectrum of pristine graphene. The G peak ($\sim 1580\,\mathrm{cm}^{-1}$) corresponds to Raman scattering by zero-momentum phonon, and the 2D peak ($\sim 2700\,\mathrm{cm}^{-1}$) originates from double resonant scattering by two phonons with opposite momenta.[87, 88] Raman spectra are dramatically changed by fluorination. The most apparent change is the rise of defect-induced D peaks ($\sim 1350\,\mathrm{cm}^{-1}$). In this case, the defect can

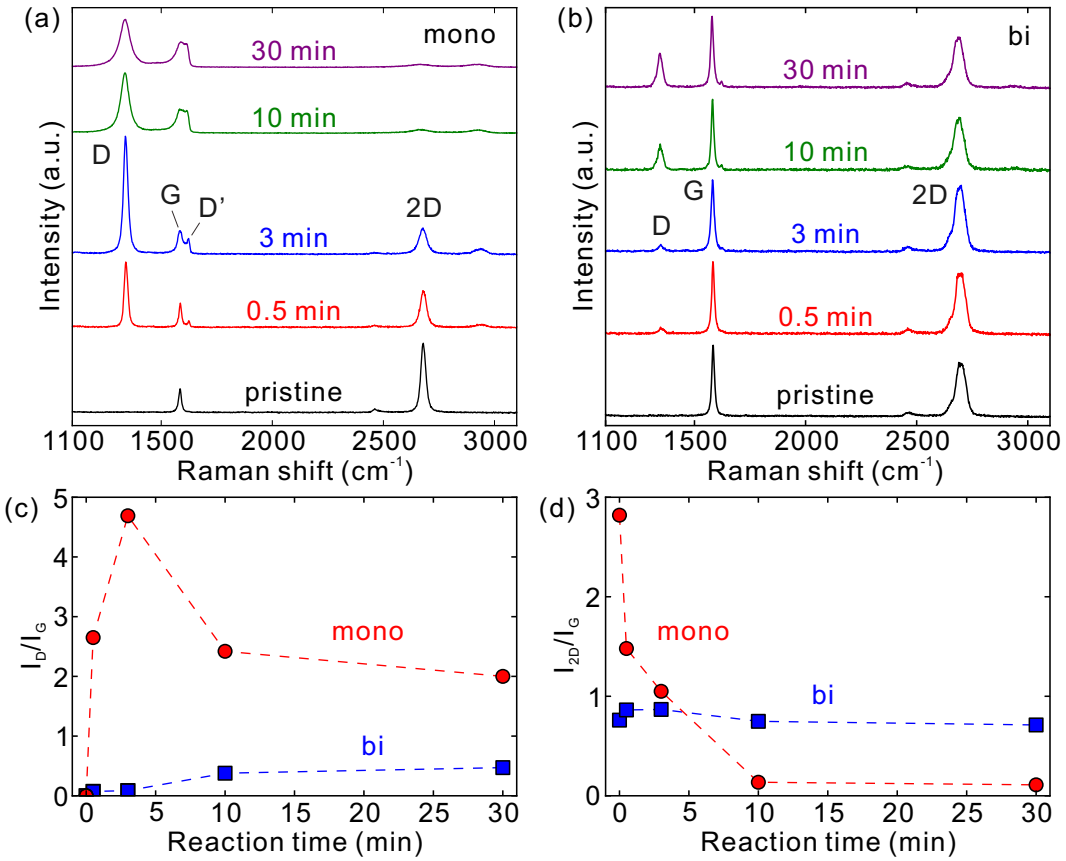

Figure 2.3: Raman spectra of (a) monolayer and (b) bilayer graphene after fluorination for several durations. Spectra in each figure are normalized with respect to the G peak intensity. Plots of (c) D peak and (d) 2D peak intensities vs. reaction time for spectra in (a) and (b).

be attributed to atomic fluorine attached to the graphene plane. Since the fluorination induces sp^3 hybridized bonding of a carbon atom with a fluorine atom, it acts as a point defect in the graphene lattice.

We now focus on reaction time dependence of intensities of the double resonant D and 2D peaks of monolayer graphene (red lines in Fig. 2.3(c) and (d)). With increasing reaction time, the D peak intensity shows non-monotonic behavior and has the maximum at 3 min, while the 2D peak intensity decreases monotonously. Such behavior of the peak intensities indicates an increase of amount of fluorine atoms attaching to the graphene. Therefore it is possible to control fluorine density by changing the reaction time. Similar behavior has been also reported previously on hydrogenated graphene, and theoretical models were proposed.[87–89] The D peak originates

from phonon-defect scattering process and requires extrinsic scatterings by defects for its activation. Then the D peak intensity is explicitly modeled to increase linearly with defect density. On the other hand, defects also perturb electronic states and decrease its life time. This effect leads to decrease of the peak intensity. The observed non-monotonic behavior of the D peak intensity results from these two competing mechanisms.[88] Meanwhile, the 2D peak intensity does not increase with elevation of defect density because it comes from two phonon scattering process. Thus, the 2D peak intensity shows monotonic reduction caused by the decrease of electronic state's life time. We conducted fluorination of bilayer graphene along with monolayer and found that changes of Raman spectra of bilayer graphene (Fig. 2.3(b)) are much different from that of monolayer. As shown in Fig. 2.3(c) and (d), the D peak intensity increased monotonically with increasing the reaction time and reached the value of $I_D/I_G \sim 0.5$, while change of the 2D peak intensity is insignificant. Although observed D peak intensities in spectra of bilayer fluorinated graphene are smaller than monolayer, these are larger than that of previous plasma fluorination studies.[90, 91] Furthermore, the fluorination of bilayer graphene was also proved by annealing as described below. The difference of Raman spectra between mono- and bi- layer graphene shows that bilayer is much less reactive to fluorine radicals than monolayer. The cause of this reactivity difference is likely to lie in intrinsic microscopic corrugation of graphene.[20, 92] Monolayer graphene has larger ripples in its plane than bilayer graphene and the corrugation enhances chemical reactivity of monolayer graphene.

2.3.2 Raman mapping and edge effect

Raman mapping measurements were performed to evaluate spatial homogeneity of fluorination. Figure 2.4 (b) shows mapping of the integrated D peak intensity of graphene flakes shown in Fig. 2.4(a). We can confirm clear difference in the D peak intensity between mono- and bi- (or thicker) layer graphene. It can also be seen that there is little fluctuation in the bulk region of these graphene and that the D peak intensity is larger near edges of monolayer graphene. For clarity, a line profile is shown in Fig. 2.4(c). The difference in the D peak intensity among three layer numbers (mono-, bi-, and multi- layer) is clearly detected as step-like profile. The difference between bi- and multi- layer can be also attributed to microscopic corrugation in graphene. The surface reactivity is expected to lower by the increase of layer number because graphene layers

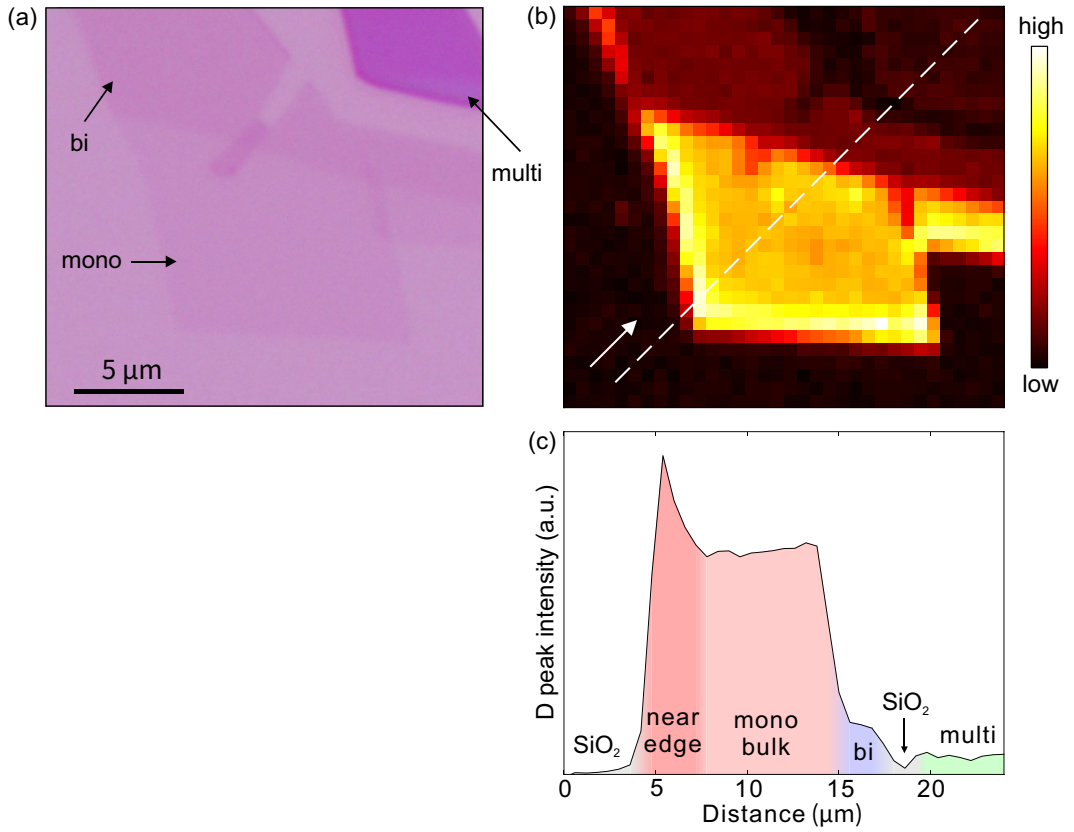

Figure 2.4: (a) Optical Micrograph of 3 min fluorinated graphene. Mono-, bi-, and multi-layer regions are included. (b) Raman mapping of the integrated D peak (1300 cm^{-1} ~ 1410 cm^{-1}) intensity. (c) Line profile of the mapping along dashed line in (b).

come close to 3-dimensional graphite and the corrugation is suppressed.[20, 92] Moreover, spatial homogeneity in bulk region and high intensity near edge of monolayer graphene can be seen in the line profile. Because the near edge region showed negligible D peaks before fluorination, the difference can be attributed to difference in fluorination degrees. Further studies are required to clarify the difference of the reaction mechanism between bulk and near edge regions in graphene.

2.3.3 Reversibility check by annealing

Fluorination is evinced by its reversibility. Fluorine atoms can be detached from graphene surface by thermal annealing. We annealed the fluorinated graphene samples in Ar atmosphere for 90 min at 573 K. Figure 2.5 shows Raman spectra of fluorinated graphene before and after annealing.

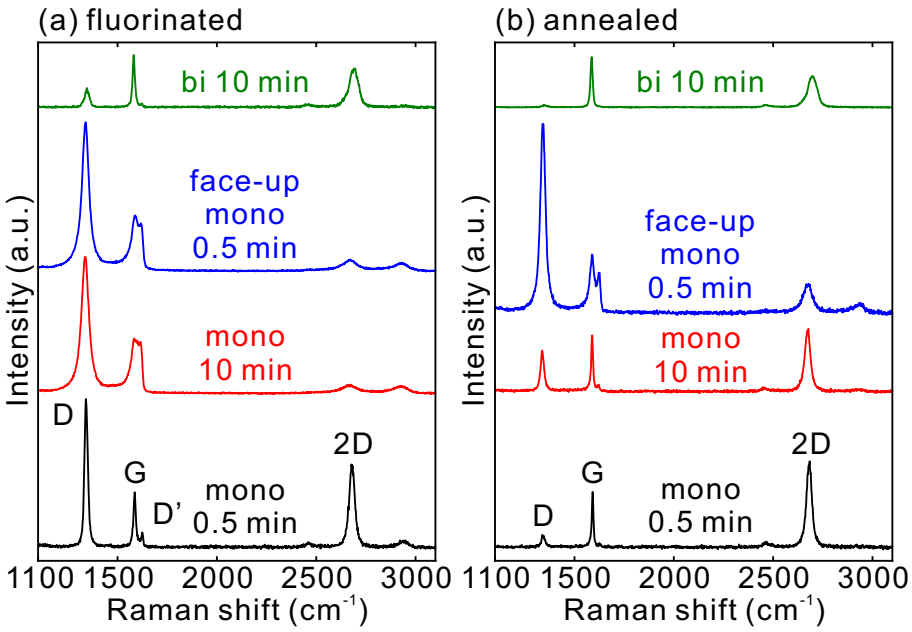

Figure 2.5: Raman spectra of fluorinated graphenes (a) before and (b) after annealing. Layer numbers and fluorination conditions are monolayer 0.5 min, monolayer 10 min, monolayer face-up 0.5 min, and bilayer 10 min (from bottom to top).

For monolayer graphene (black and red lines in Fig. 2.5), the D peak intensity decreases and the 2D peak intensity increases after annealing, indicating reversible fluorination of graphene. The residual D peak after annealing can be attributed to vacancy defects created when fluorine is desorbed.[21, 93] The remained D peak has a higher intensity for longer fluorination time because higher fluorine concentration enhances the chance of vacancy formation during annealing. It is important to note that bilayer graphene (green lines) also showed reversibility. Although fluorination degree is relatively low, bilayer graphene can be indeed fluorinated by our method. Since the dominant use of fluorine radicals is the key characteristic of our method, fluorine radicals are more effective than fluorine containing ion species for fluorinating bilayer graphene.

Here, we show the effect of graphene-face direction (face-up or face-down) during plasma treatment. Before annealing, the spectrum of 0.5 min "face-up" treated sample (blue line in Fig. 2.5(a)) is similar with that of 10 min "face-down" treated one (red line). After annealing, the face-up fluorination sample has a much higher D peak than the 10 min face-down treated sample. This fact clearly indicates that face-up treated graphene was highly-damaged by bombardment of

fluorine and argon ions during plasma treatment. In contrast, the face-down treatment can utilize fluorine radicals for fluorination without damaging graphene by the ion bombardment.

2.4 XPS analysis

Figure 2.6 shows XPS spectra of transferred CVD-grown monolayer graphene after 3 min fluorination. Pronounced F1s peak and chemical shift of the C1s peak are proofs of the existence of fluorine atoms and C-F bonding. The F1s spectrum was fitted by two peaks. The main component at a higher binding energy of ~ 688.5 eV is related to F atoms bonding to graphene and the small component at a lower binding energy of ~ 687 eV corresponds to F atoms bonding to Si atoms on the substrate. Carbon-fluorine bonds introduce several chemically-shifted components in the C1s peak.[94] The strongest component (~ 284.9 eV) corresponds to non-functionalized sp^2 bonding C atoms. The component with the second lowest binding energy (~ 285.7 eV) is attributed to aliphatic non-functionalized sp^3 C atoms (surface contamination) or non-functionalized sp^2 C atoms which have one neighboring C atom bonded with one F atom. Three small components labeled "C-CFn" in the figure (286.5 ~ 288.2 eV) are also related to non-functionalized C atoms with some fluorinated neighbors. Components with larger shifts are attributed to C atoms directly bonded to F atoms. In addition to C atoms bonded with one F atom (~ 289.6 eV), C atoms bonded with two or three F atoms (~ 291.7, 293.5 eV) exist. These multiple fluorine bonds are likely to form at defects, edges, or grain boundaries, amounts of which are thought to be relatively large in the transferred CVD graphene sample. This fact makes it difficult to estimate F/C ratio accurately by analyzing area ratio of the F1s to C1s peaks. To estimate F/C ratio excluding multiple fluorine bonds, area ratio of the C-F component in the C1s peak to the whole C1s peak can be used. From the peak analysis, we obtained an F/C ratio of 0.17, corresponding to fluorination of one of 6 C atoms.

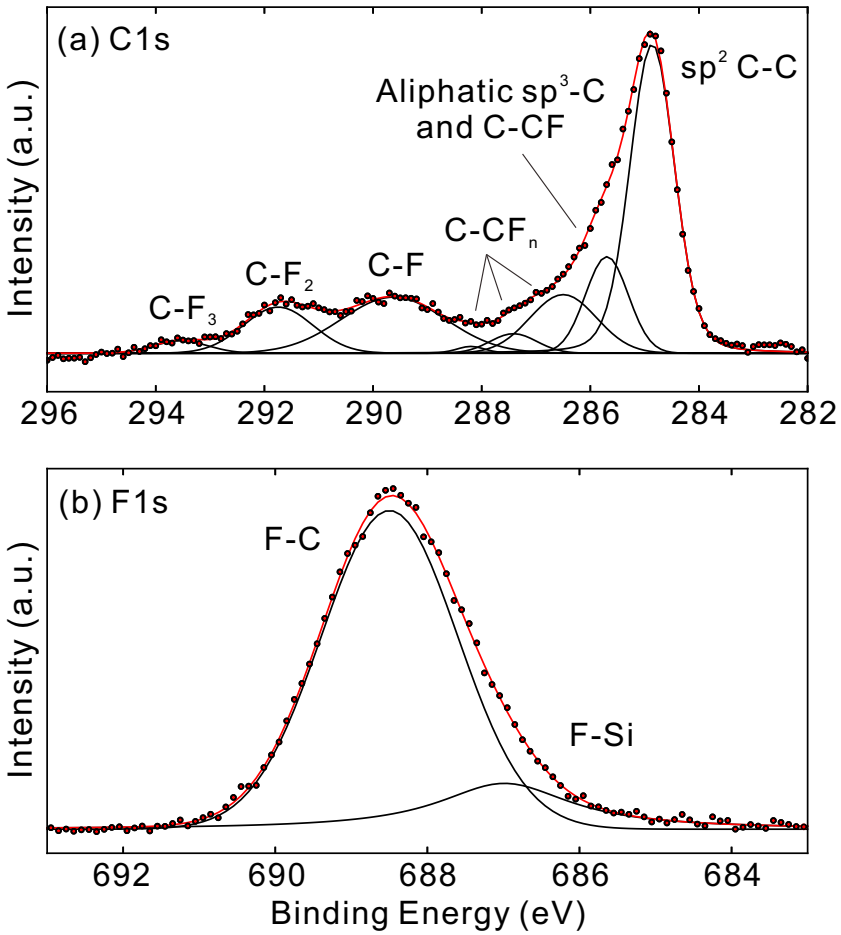

Figure 2.6: XPS (a) C1s and (b) F1s spectra of monolayer graphene after 3 min fluorination. (dots: experimental data, black lines: fitting curves, red lines: sum of the fitting curves) The background is subtracted.

Chapter 3

Charge transport of fluorinated graphene

Before proceeding to the control of spin transport, we will show charge transport properties of fluorinated graphene in this chapter. Dependence on fluorine concentration and temperature is explored in order to examine the effects of fluorination on transport mechanism. The last section is on the improvement of the device performance using ionic liquid gating.

3.1 Device structure and measurement system

The fluorinated graphene field effect transistor (FET) devices are fabricated by electron beam (EB) lithography and EB evaporation of Ti/Au and lift-off. Cross sectional schematic of the device is shown in Fig. 3.1. Carrier (electron and hole) concentration in fluorinated graphene is controlled by back gate voltage (V_G).

Three-terminal transport measurements were performed in a vacuum probing system from at room temperature down to at 78 K. First, linear I_D-V_D (drain current - drain voltage) characteristics were confirmed and then I_D-V_G (drain current - back gate voltage) curves were measured at a fixed V_D. Two-terminal resistivity was obtained by the relation $\rho = (W/L)(V_D/I_D)$, where W and L are sample width and length, respectively.

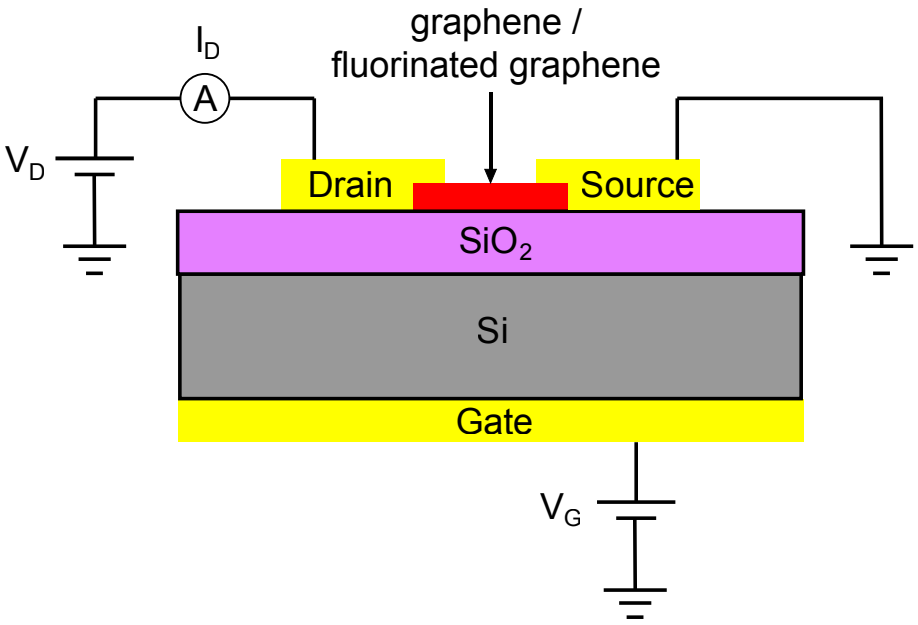

Figure 3.1: Cross sectional schematic of (fluorinated) graphene FET device.

3.2 Room temperature characteristics

Figure 3.2 shows Raman spectra (a) and room temperature ρ-V_G (b) characteristics of monolayer fluorinated graphene devices with different fluorination times. Resistivity gradually increases up to 3 orders of magnitude larger value than pristine graphene. CNPs of fluorinated graphene are more largely shifted to positive V_G than pristine graphene. Although uncontrolled transfer doping from physisorbed molecules or resist residues cannot be perfectly excluded, this result indicates the hole doping of fluorinated graphene due to the high electronegativity of attached fluorine atoms.[95]

The characteristics of bilayer graphene are shown in Fig 3.2 (c) and (d). Changes in both Raman and transport characteristics by fluorination are obviously smaller than those of monolayer graphene. This result is consistent with previous reports,[21, 90] and is possibly due to the suppression of ripples in bilayer graphene with enhanced surface stability.[20] Thus, we will focus only on the monolayer graphene in what follows.

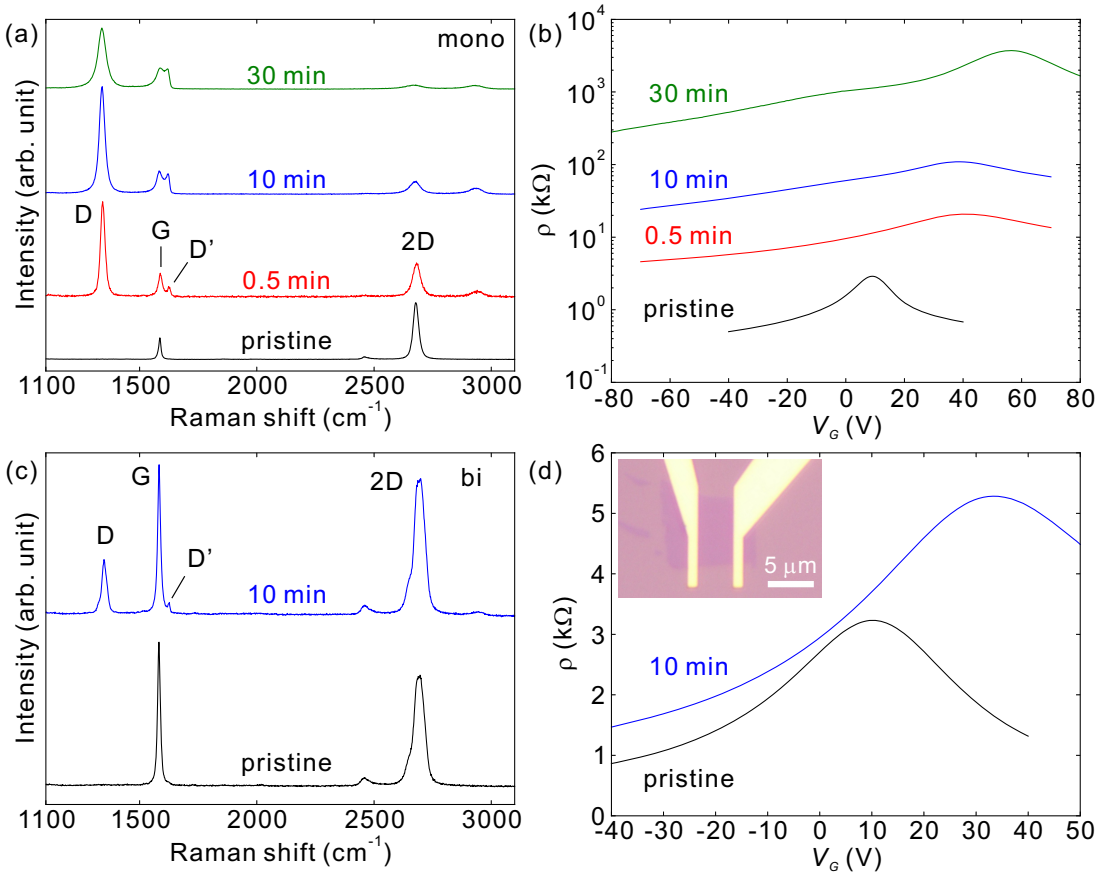

Figure 3.2: (a) Raman spectra and (b) transport characteristics at room temperature of fluorinated monolayer graphene devices. (c) and (d): Characteristics of fluorinated bilayer graphene devices. Inset to (d): optical micrograph of a typical monolayer fluorinated graphene device.

3.3 Temperature characteristics

To examine transport mechanism, we measured temperature characteristics of the devices (Fig. 3.3). We define V_{CNP} as the gate voltage at which resistivity takes maximum value and each curve in Fig. 3.3 is shifted with respect to V_{CNP}. Also shown in Fig. 3.3 is estimated surface charge density $n = \varepsilon\varepsilon_0 V_G/te$. Here $\varepsilon, \varepsilon_0, t$, and e are permittivity of SiO_2, electric constant, thickness of SiO_2, and elementary charge. Pristine graphene shows slightly increasing resistivity with increasing temperature (Fig. 3.3 (a)). This type of temperature dependence can be accounted for the electron scattering from phonon in graphene and surface phonon of SiO_2 substrate.[96] On the other hand, increasing resistivity with decreasing temperature is clearly observed on fluorinated graphene (Fig. 3.3 (b), (c), and (d)), which indicates insulator-like behavior.

3.3.1 Variable range hopping

As shown in Fig. 3.4 (a), this temperature dependence is well fitted by variable-range hopping model (VRH) in two dimensions:[97]

$$\rho = \rho_0 \exp\left[(T_0/T)^{1/3}\right], \tag{3.1}$$

$$T_0 = \frac{13.8}{k_B N(E_F)\, a^2}, \tag{3.2}$$

where T_0, k_B, $N(E_F)$, and a are characteristic temperature, Boltzmann constant, density of states at Fermi level, and localization length. Good fitting to the VRH model suggests existence of localized electronic states around Fermi level.[24–26] Slopes of the lines in Fig. 3.4 (a) (corresponding to T_0 in Eq. (3.1)) are strongly dependent on gate voltage, with higher T_0 in lower $V_G - V_{CNP}$.

Fig. 3.4 (b) shows V_G dependence of T_0. In the dilute fluorinated (0.5 min) device, T_0 goes to zero by introducing high carrier density. Vanishing T_0 means that VRH model no longer holds at high carrier density. As shown in Fig. 2 (b), T dependence of ρ in this region is very weak and conductivity exceeds minimum conductivity of graphene $4e^2/h$, implying onset of metallic conduction.[20, 24, 25] The transition from insulating (VRH) to metallic conduction gradually disappears by increasing fluorination rate. Although tendency toward the transition is kept in 10 min fluorinated device, finite T_0 ($\sim$ 85 K) remains at the highest carrier density. Regarding the most highly fluorinated (30 min) sample, quite high T_0 is maintained over whole V_G range. These

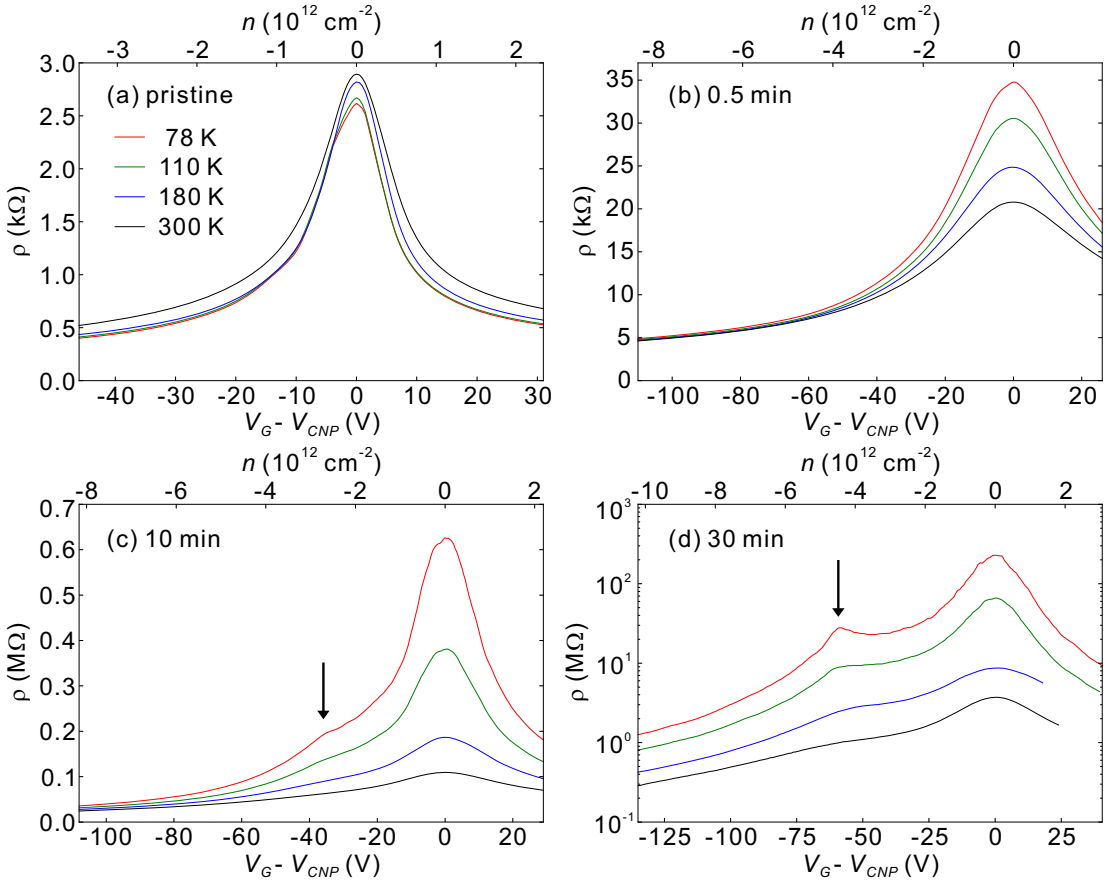

Figure 3.3: Temperature characteristics of (a) pristine, (b) 0.5 min, (c) 10 min, (d) 30 min fluorinated graphene devices. The temperatures are 78, 110, 180, and 300 K (from bottom to top for (a); from top to bottom for (b), (c), and (d)).

results indicate that states in wider energy range become localized by introducing higher fluorine density.

3.3.2 Asymmetric feature

We now focus on anomalous features in transport properties of highly fluorinated graphene: kink or local resistivity maxima appearing at around $V_G - V_{CNP} = -38$ V (Fig. 3.3 (c)) and -53 V (Fig. 3.3 (d)). Electron-hole asymmetry in resistivity accompanies these features. Asymmetry becomes higher with elevating energy from CNP ($|V_G - V_{CNP}|$), reaching values of $\rho_h/\rho_e(|V_G - V_{CNP}| = 32\ \mathrm{V}) = 1.2$ for 10 min fluorinated graphene and $\rho_h/\rho_e(|V_G - V_{CNP}| = 40\ \mathrm{V}) = 2.5$ for 30 min at 78 K. These features can be ascribed to resonant fluorine impurities. It is reported that fluorine adsorbates create a midgap impurity state at relatively distant energy level (-0.67 eV) from CNP,[27] which is fluorine's unique property. This kind of impurity introduces energy-dependent scattering rate, and can create electron-hole asymmetry and local maximum in transport characteristics.[28–31] Using pristine graphene's density of states (DOS), $V_G - V_{CNP} = -38$ and -53 V correspond to $E_F \sim -0.2$ eV. Due to relatively high impurity concentration where localization effect is important, resistivity of these samples reflects not only scattering rate from independent impurities, but also localization effect and perturbed density of states structure. Quantitative discussions on the position of these features require more detailed theoretical and experimental studies, however, the order of them seems to be reasonable when compared with the calculated energy level of midgap state of resonant fluorine impurity.

When discussing electron-hole asymmetry in resistivity, we have to consider the effect of carrier injection from invasive metal contacts.[98–100] It is claimed that metals directly deposited on graphene cause carrier injection into graphene, or Fermi level pinning, owning to the work function difference. In our case using Ti contact, n-type pinning of graphene below the contact can be assumed. Therefore p-n junction close to contact is formed when bulk graphene is p-doped, whereas n-n junction is formed when n-doped. This leads higher (lower) resistivity in p-doped (n-doped) region. Asymmetry appearing in our data possibly includes such an effect, however, the simple model above should result in monotonic carrier density dependence of resistivity in p-doped (or n-doped) region. Only the contact doping seems to be insufficient to explain the local resistivity maximum in p-doped region, which is our main finding.

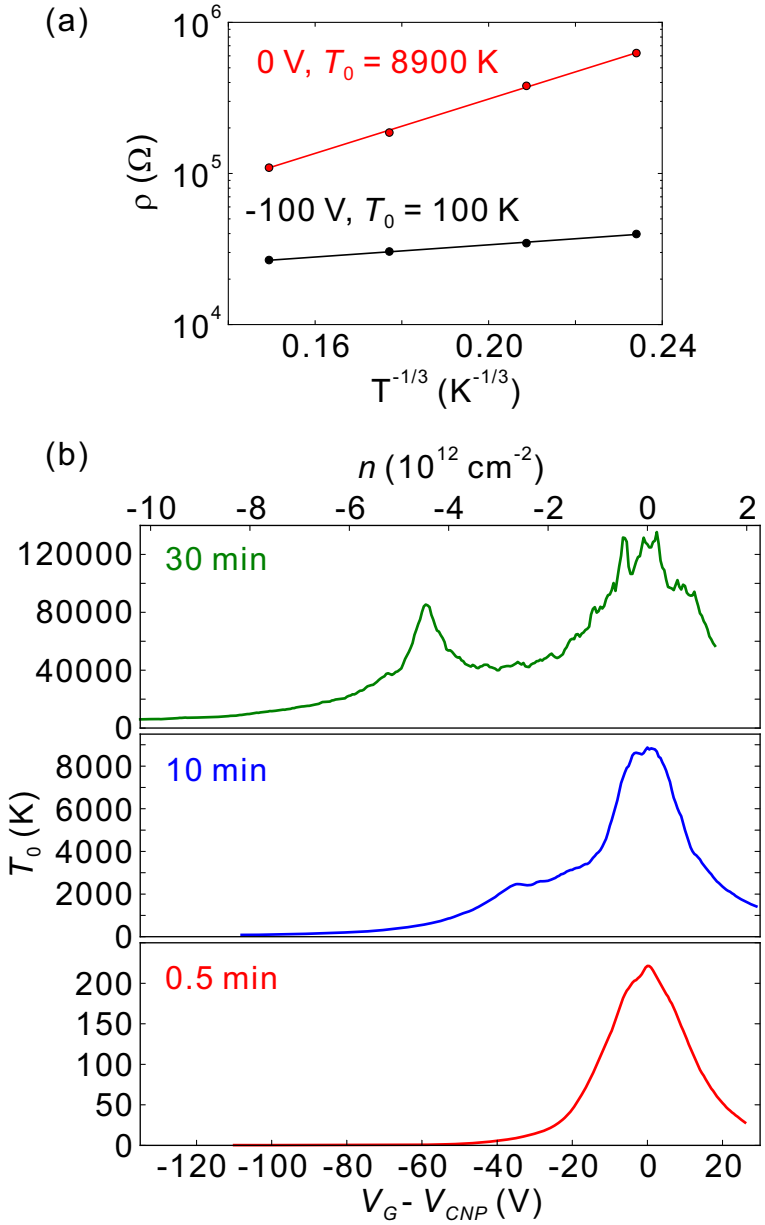

Figure 3.4: (a) Fitting to VRH model of temperature characteristics of 10 min fluorinated graphene. The upper data is resistivity at $V_G - V_{CNP} = 0$ V and the lower data is resistivity at -100 V. (b) V_G dependences of characteristic temperature T_0 in VRH model.

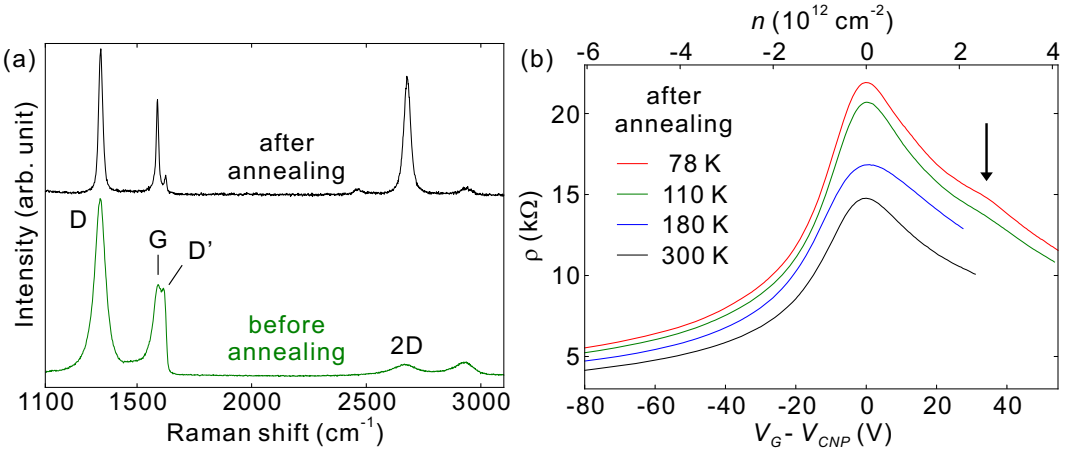

Figure 3.5: (a) Raman spectra of 30 min fluorinated graphene device before and after annealing. (b) Temperature characteristics of the device after annealing. The temperatures are 78, 110, 180, and 300 K (from top to bottom).

3.3.3 Reversibility check by annealing

To further evidence that the anomalous features discussed above originate from fluorine impurities, we have defluorinated the samples by thermal annealing. The devices were heated at 300 °C for 30 min in Ar atmosphere with a pressure of 10 kPa and a flow rate of 100 sccm. Figure 3.5 (a) shows Raman spectra of 30 min fluorinated graphene before and after annealing. Before annealing, the D and G peaks have large width and intensity of the 2D peak is very low. These features similar to the spectrum of amorphous carbon indicate quite large amount of disorder induced by randomly attaching fluorine impurities.[87, 101] Sharp D and G peaks and intense 2D peak are recovered by the annealing, which means removal of fluorine atoms from graphene. The remaining D peak can be accounted for point defects created when fluorine atoms are detached.[21, 93]

Temperature characteristic of the annealed device is shown in Fig. 3.5 (b). Although the order of resistivity decreases by annealing, it is only about one order larger than pristine graphene (Fig. 3.3 (a)). This is consistent with presumable existence of structural point defects detected by Raman spectroscopy. The local resistivity maxima in the hole conduction region now disappeared completely. Instead, annealed graphene shows asymmetry opposite to that before annealing, namely, higher resistivity at the electron conduction region (positive $V_G - V_{CNP}$). This asymmetry is comparable to that of fluorinated graphene: $\rho_e/\rho_h(|V_G - V_{CNP}| = 40\ \mathrm{V}) = 1.7$ at 78 K. A kink

feature also appears at the electron conduction region. It is speculated that these features are also originated from resonant impurity states with energy levels distant from CNP. In this case structural point defects, possibly vacancies, are regarded as the resonant impurities. The positions of vacancy defect levels in graphene have been reported to depend on the type of reconstruction, and to be at positive energy in some configuration.[30] Although the dominant type of defect in annealed device is currently unknown, there is a notable difference from fluorinated device. Therefore, we conclude that this kind of asymmetric properties could be useful, with further detailed studies, to derive the information on covalently bonded atoms or structural defects in graphene.

3.4 Ionic liquid gating

When we see the fluorinated graphene FETs as switching device, on/off ratio becomes important. We have shown insulator-like behaviour of flurinated graphene, at least around charge neutrality point. If we can apply very high gate voltage on fluorinated graphene FETs, we may move the Fermi level to energy levels where localization length is much shorter or even levels where we see metallic conduction. This kind of metal-insulator transistion could result in high on/off ratio. However, what we see in Sec. 3.2 were not high on/off ratios at room temperature. On/off ratio is about 10, even if we apply gate voltage over 100 V. The reason of this low performance could be that there are too many impurity states near charge neutrality point and the electric field effect is not enough high to move the Fermi level substantially.

A method to induce much higher electric field effect in graphene is ionic liquid gating (ILG). In this section we apply the ionic liquid gating to graphene and fluorinated graphene to see the possibility of higher on/off ratio.

Schematic and optical micrograph Ionic liquid gating device is shown in Fig. 3.6. Since the BG device has a thick gate dielectric (285 nm SiO_2), induced carrier concentration cannot be high, for instance 10^{11} cm^{-2} at $V_G = 2$ V. On the other hand, in the case of ILG, the thickness of the gate dielectric (electric double layer of ion liquid) is extremely thin (1 nm) and has high dielectric constant (12.8), carrier concentration can reach the value around 10^{14} cm^{-2} at $V_G = 2$ V.

Transport properties of pristine and 30 min fluorinated graphene at room temperature are shown in Fig. 3.7. The curves are shifted with respect to the CNP. As shown in Fig.3.7 (a), (c), ILG of

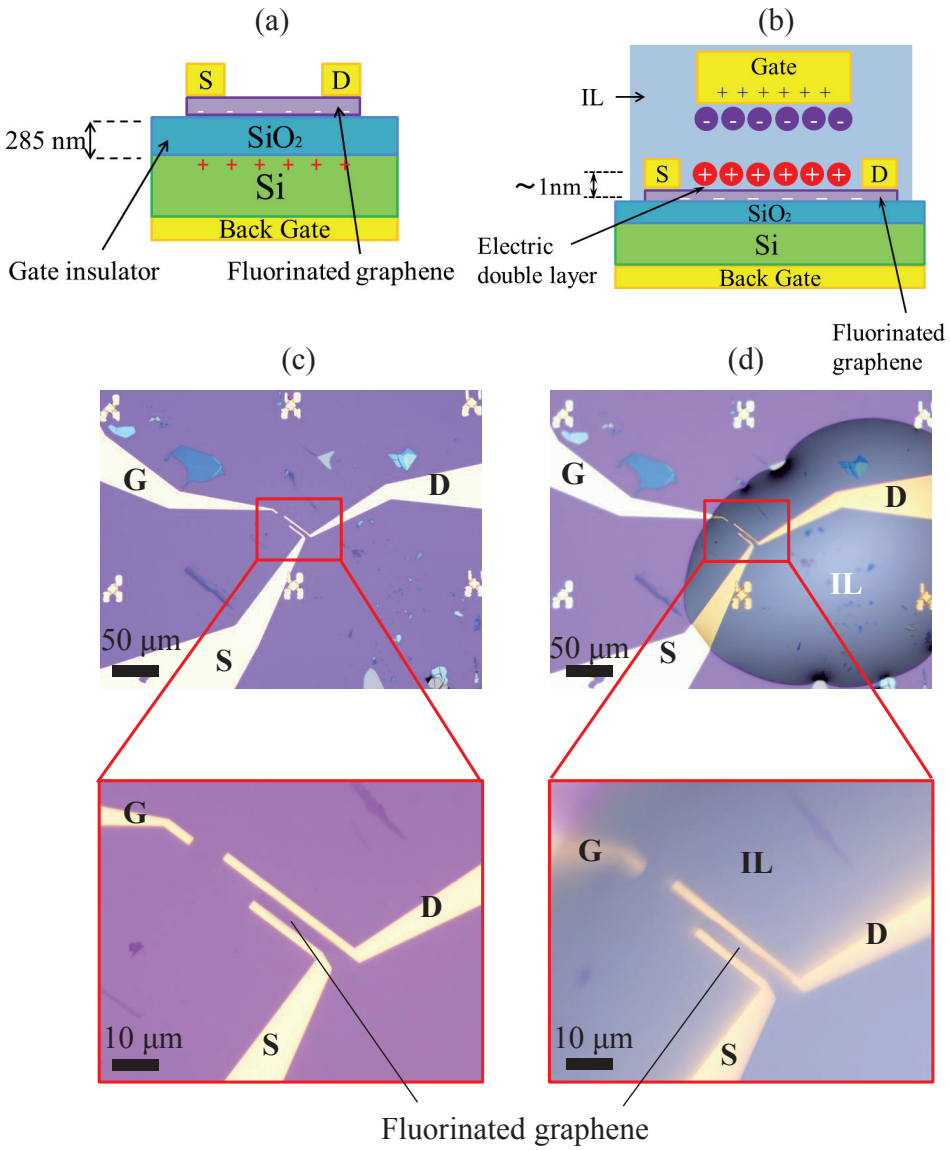

Figure 3.6: (a) Cross-sectional schematic of back gate operation of fluorinated graphene FET. (b) cross-sectional schematic of ionic liquid gating. (c) optical micrograph of a fluorinated graphene FET without ionic liquid. (d) optical micrograph with ionic liquid.

pristine graphene leads to lower resistivity at the same gate voltages than BG, indicating low voltage driving by ILG. However, the on/off ratios do not change so much for both BG (5.9) and ILG (6.5) due to saturating behavior of resistivity at high carrier density in pristine graphene FET[102–104]. Here, the on/off ratio was calculated using the ratio of the maximum and minimum resistivity of the curves: the ratio of resistivity at $V_G - V_{CNP} = 0$ V and -50 V for BG, at $V_G - V_{CNP} = 0$ V and 2 V for ILG. In contrast, for fluorinated-graphene, an apparently lower minimum resistivity was obtained by ILG than BG. In the 30 min fluorinated-graphene, electronic states are localized over the whole BG region. Higher charge density induced by ILG could move the Fermi level toward the energy region with larger density of states and localization length, leading to a lower resistivity in VRH conduction. As a result, the twice higher on/off ratio (10) was obtained for fluorinated-graphene with ILG. Note that ILG also leads to low voltage driving in fluorinated-graphene, as shown in Fig. 3.7 (b), (d).

The dependence of the on/off ratio of BG and ILG devices on the fluorination time at room temperature is shown in Fig. 3.8. For all reaction times, higher on/off ratios were obtained by ILG. While the BG fluorinated-graphene devices show lower on/off ratios than that of the BG pristine device, the on/off ratio clearly increases with higher fluorine densities (10 and 30 min) for the ILG devices. The resistivity increases at both on- and off-states after fluorination. Hopping conduction degrades the effect of BG, as observed in Fig. 3.7 (b). Accordingly, the resistivity at on-state does not decrease efficiently, resulting in the lower on/off ratios in the fluorinated-graphene devices than that of the pristine device with BG. On the other hand, one can reach to the range of much larger density of states and localization length with ILG because of the extremely high electric field effect, which leads to drastic decrease of the on-state resistivity. As a result, the ILG fluorinated-graphene devices have the higher on/off ratios than that of the ILG pristine device in spite of the increase of the on-resistivity by fluorination. Therefore, the higher on/off ratios can be obtained by the combination of fluorination and ILG.

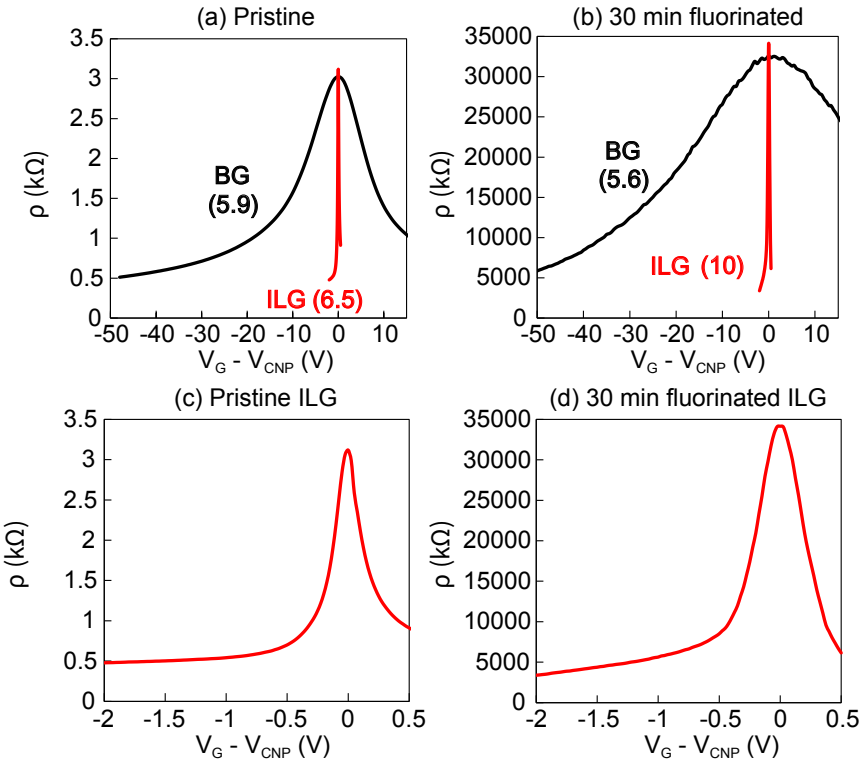

Figure 3.7: (a) Gate voltage dependence of resistivity of pristine graphene FET with back gating (BG) and ionic liquid gating (ILG). (b) Same characteristics of 30 min fluorinated graphene FET. (c) Magnified view of (a) for ILG. (d) Magnified view of (b) for ILG.

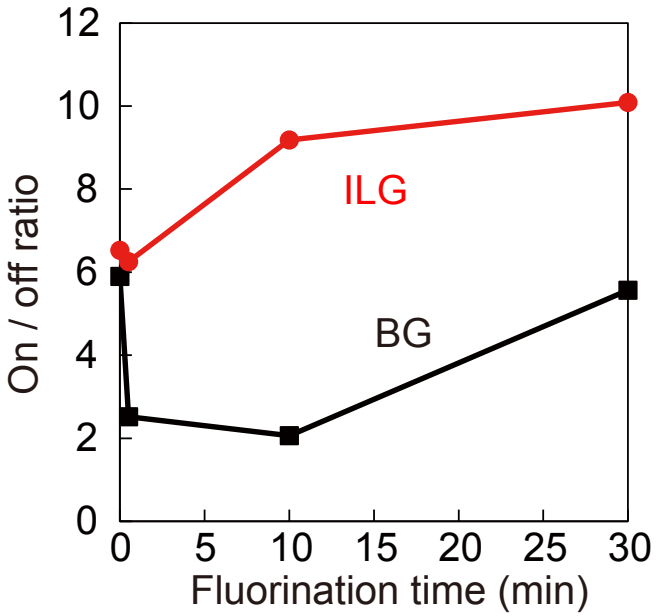

Figure 3.8: On/off ratios of fluorinated graphene FETs with different fluorination reaction time. Zero reaction time corresponds to pristine graphene.

Chapter 4

Spin transport of fluorinated graphene

As in introduction (Sec. 1.4), one of the goals of our graphene research is to control and generate spin current by fluorination. In former part of this chapter, we explore the possibility of spin transport control of fluorinated graphene through magneto-transport measurement. We will show the results of non-local resistance measurements to prove the possibility of spin Hall effect in the latter part.

4.1 Magnetotransport and control of spin relaxation

Magnetotransport is a well-established tool to extract important physical parameters of mesoscopic samples. In this section, we present the magnetotrasport properties of dilute fluorinated graphene, extract parameters related to spin relaxation, and show the possibility of spin relaxation control.

4.1.1 Device structure and measurement system

The Hall bar structured device (Fig. 4.1) is used for magnetotransport measurements. Fabrication procedures of this device is same as devices used in Chapter 3. The graphene channel is dilute-fluorinated with reaction time of 30 seconds before patterning and depositing electrodes. In dilute regime, we can estimate defect (or fluorine) density in graphene from Raman spectrum (Fig. 4.2, upper spectrum), that indicates fluorine density of 8×10^{11} cm^{-2} or fluorine-to-carbon ratio of 0.02 %.[105, 106] We have also fabricated a pristine graphene device for comparison. Amount of point defects of pristine graphene device is undetectable in terms of D peak of Raman spectrum (Fig.

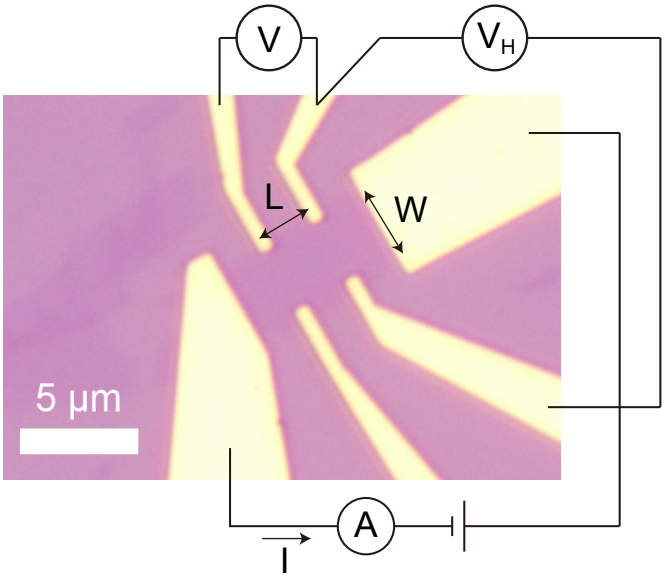

Figure 4.1: Optical micrograph and measurement setup for the fluorinated graphene Hall bar device.

4.2, lower).

Magnetotransport measurements are conducted in Helium refrigerator equipped with superconductor magnet which can generate magnetic field up to 10 T perpendicular to the sample. Temperature of the device is varied by a heater. Four terminal conductivity (resistivity) of the device is recorded as a function of gate voltage, magnetic field and temperature. The bias voltage is applied and the current (I) through the device is measured by current amplifier and voltmeter as in Fig. 4.1). Simultaneously, we measure voltages appeared at longitudinal voltage probes (V) and Hall voltage probes (V_H) by low-noise preamplifier and voltmeter. Four terminal (longitudinal) resistivity can be written as $\rho_{xx} = (W/L)(V/I)$, and the Hall (transverse) resistivity is written as $\rho_{xy} = V_H/I$. Measurements of the values above are conducted while all of the parameters (gate voltage V_G, temperature T and magnetic field B) is controlled and swept by a custom software on PC.

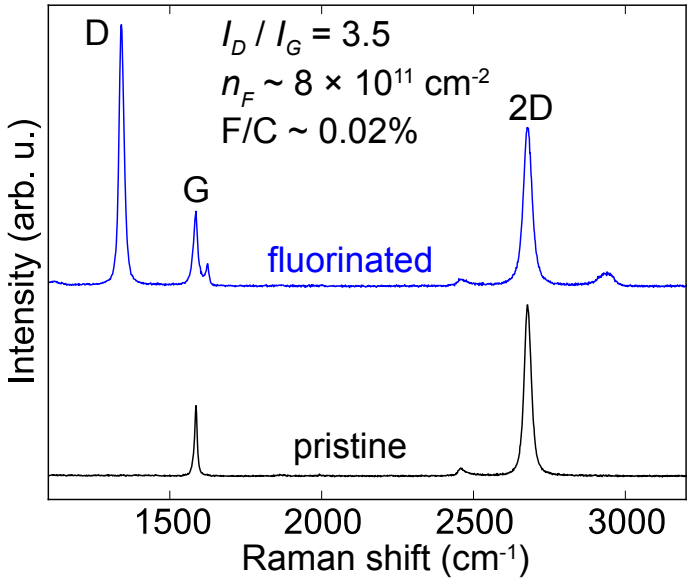

Figure 4.2: Raman spectrum of graphene channel of the Hall bar device for magnetotransport measurement. Upper (lower) panel is the spectrum of fluorinated (pristine) graphene.

4.1.2 Localization and Hall effects

We shall show basic properties of the devices through standard Hall measurements before going to detailed magnetotransport. Transport properties without magnetic field is shown in Fig. 4.3. At zero field, conductivity is just a inverse of resistivity ($\sigma = 1/\rho_{xx}$). The conductivity of pristine graphene device (Fig. 4.3 (a)) shows very weak temperature dependence. On the other hand, the conductivity of fluorinated graphene shows weak but clear temperature dependence. Conductivity exceeds minimum metallic conductivity of the graphene ($4e^2/h$) at high gate voltages. With low gate voltage (near charge neutrality point), conductivity is the same order of e^2/h. It is not straightforward to determine whether fluorinated graphene is metallic (weakly localized) or insulating (strongly localized) in this regime. As shown in Fig. 4.4, temperature dependence of the resistivity is well-fitted to VRH model introduced in Section 3.3.1, only where the resistivity is above $1/(2e^2/h)$. The resistivity deviates from this model for lower resistivity, that is indicative of transition from strongly localized to weakly localized regime.[25] Thus, we shall set the boundary between the two states as $\sigma = 2e^2/h$. We will use only metallic region for detailed magnetotransport measurements in subsequent section.

Hall effects can be clearly seen in both Hall bar devices. Figure 4.5 shows conventional Hall

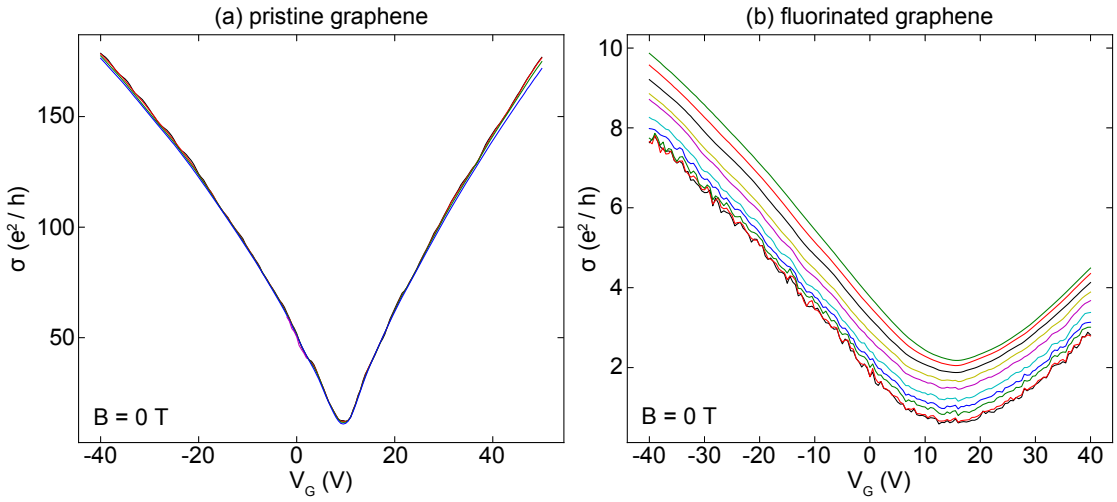

Figure 4.3: Four terminal conductivities of the Hall bar device as functions of gate voltage. (a) Characteristics of pristine graphene device. Temperatures are 7, 15, 30, 50, 100 K. (b) Characteristics of fluorinated graphene device. Temperatures are 2.6, 3, 5, 7, 10, 20, 30, 50, 75, 100 K (from bottom to top).

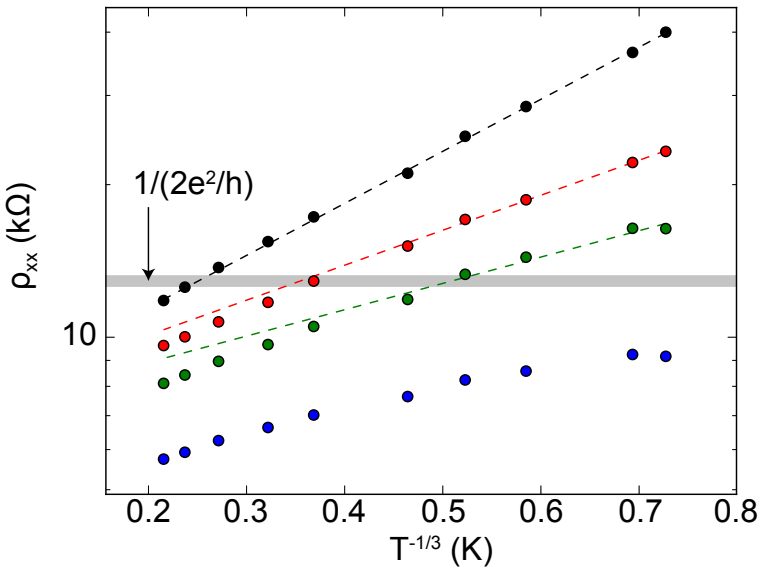

Figure 4.4: Fitting to the VRH model of the temperature dependence of resistivity of the fluorinated graphene Hall bar. Gate voltages are 15, 25, 30, 40 V (from top to bottom). Dashed line is the fitting to VRH model using only 5 data (low temperatures: 2.6, 3, 5, 7 and 10 K) for each gate voltage.

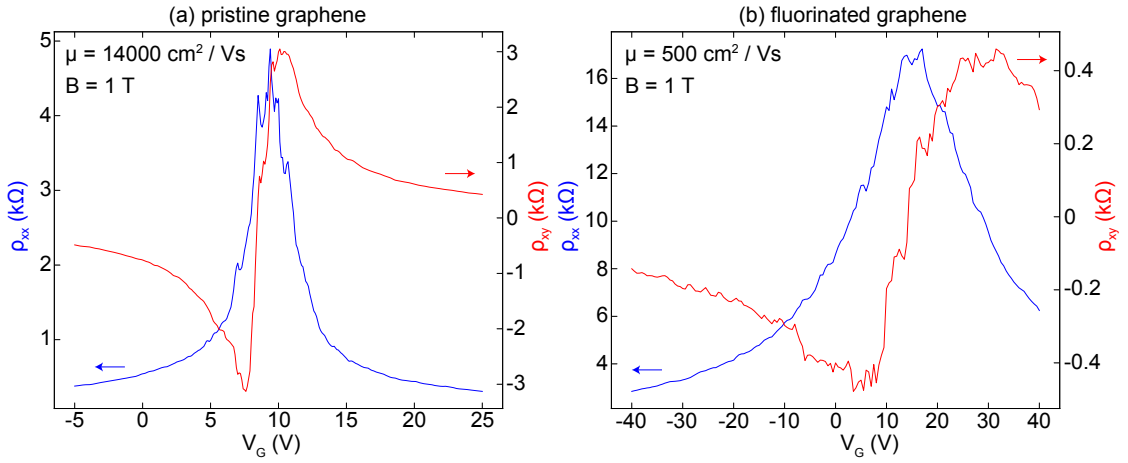

Figure 4.5: Conventional Hall effect of the (a) pristine and (b) fluorinated graphene Hall bar devices.

effect in relatively low magnetic field (1 T). We can see switching of Hall resistance polarity at resistivity maximum (charge neutrality point). Fluorinated graphene has broader gate voltage range where Hall resistance polarity is switching (around $V_G = 5 \sim 25$ V) than pristine graphene. This feature can be attributed to strongly localized nature in this region, as described above. The carrier mobility has weak gate voltage dependence in both devices, and the values are around $\mu = 14000$ cm^2/Vs for pristine and $\mu = 500$ cm^2/Vs for fluorinated graphene. Behaviors at high magnetic field is qualitatively different reflecting this mobility difference. Pristine graphene shows clear anomalous quantum Hall effect at 10 T as shown in Fig. 4.6, which is an evidence for two dimensional massless Dirac fermion in graphene.[107] Note that transverse conductance $\sigma_{xy} = \rho_{xy}/(\rho_{xy}^2 + \rho_{xx}^2)$, instead of ρ_{xy}, is plotted in this figure in order to clarify the existence of Hall plateaux. Fluorinated graphene actually shows a quantum oscillation in spite of its low mobility, however, it is only a hint of quantum Hall effect.

4.1.3 Magnetotransport property

Further details on the conduction mechanism can be revealed by measuring magnetoconductivity, i.e., conductivity as a function of magnetic field applied to the device. Figure 4.7 shows magnetoconductivity at gate voltage of -25 V and at different temperatures. Gate voltage of -25 V corresponds to carrier density of -3.0×10^{12} cm^{-2}. Dashed lines are fit to the follow-

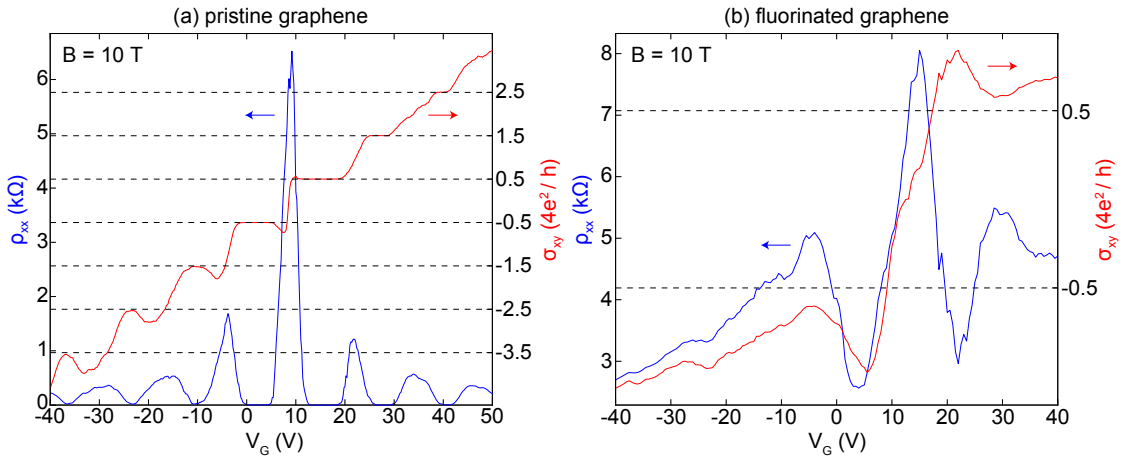

Figure 4.6: (a) Quantum Hall effect of the pristine graphene Hall bar device. (b) Fluorinated graphene Hall bar shows only a hint of quantum Hall effect.

ing equation describing magnetoconductivity due to the weak localization effect in disordered graphene.[33, 108, 109]

$$\Delta\sigma(B) = \frac{e^2}{\pi h}\left[F\left(\frac{4l_B^{-2}}{L_\phi^{-2}}\right) - F\left(\frac{4l_B^{-2}}{L_\phi^{-2}+2L_i^{-2}}\right) - 2F\left(\frac{4l_B^{-2}}{L_\phi^{-2}+L_i^{-2}+L_*^{-2}}\right)\right] \tag{4.1}$$

$$F(z) = \ln z + \phi\left(\frac{1}{2}+\frac{1}{z}\right) \tag{4.2}$$

Here ϕ, $l_B = \sqrt{\hbar/eB}$, L_ϕ, L_i and L_* are digamma function, magnetic length, phase coherence length, intervalley scattering length, and intravalley scattering length, respectively. Exact determination of 3 fitting parameters (L_ϕ, L_i and L_*) is difficult, however, we can reproducibly extract only L_ϕ by starting fitting with condition $L_i \sim L_*$ or assigning $L_i = L_*$.

Temperature dependence of phase coherence length is extracted from fitting of each curves. Furthermore, we can repeat the fitting for data at other gate voltages to acquire L_ϕ as a function of the carrier density and the temperature. Figure 4.8 shows temperature dependence of phase coherence time $\tau_\phi = L_\phi^2/D$ for three selected carrier densities. Apparently, τ_ϕ increases with decreasing temperature. Each data is fitted to the following equation.

$$\tau_\phi^{-1} = aT + bT^2 + \tau_{sat}^{-1} \tag{4.3}$$

Linear and quadratic temperature dependence can be explained by electron-electron interaction.[110–112] The important point is saturation (τ_{sat}) at zero temperature limit. This kind of saturation has

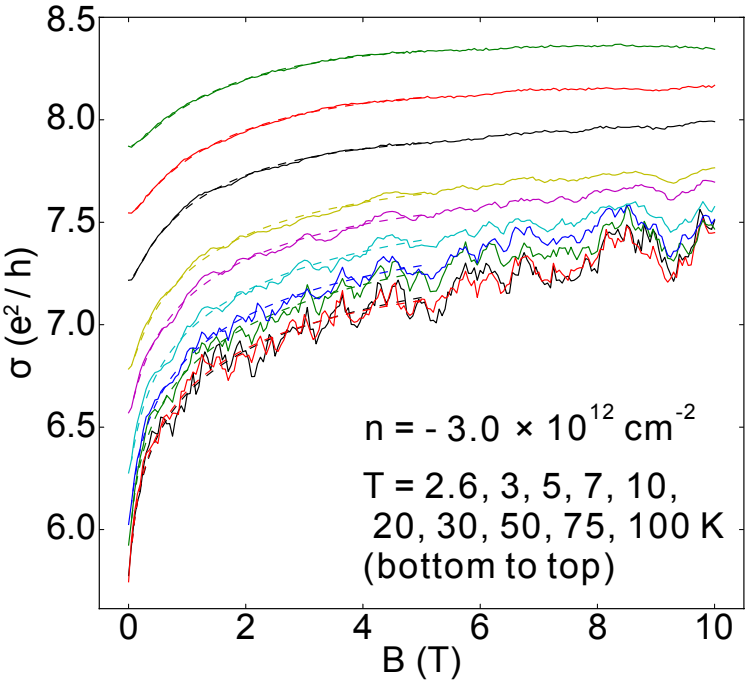

Figure 4.7: Magnetoconductivity of the Hall bar device. $V_G = -25$ V corresponds to $n = -3.0 \times 10^{12}$ cm^{-2}. Temperatures are 2.6, 3, 5, 7, 10, 20, 30, 50, 75, 100 K (from bottom to top).

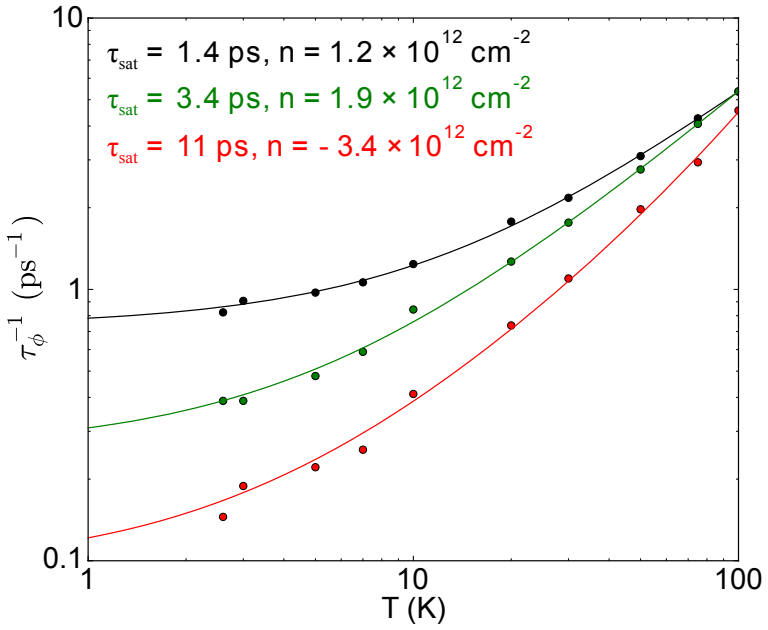

Figure 4.8: Temperature dependence of electron phase coherence time (τ_ϕ).

been ascribed to decoherence due to another degree of freedom, for example, spin.[33, 113] Here we can at least say that τ_{sat} is lower bound of spin coherence time.

Obviously, τ_{sat} is dependent on carrier density (or gate voltage). τ_{sat} - V_G relation is plotted on Figure. 4.9. τ_{sat} can be modulated by about 1 order of magnitude by changing gate voltage. The result indicates a possibility of gate-controlled spin relaxation, which might be applied to, for example, spin FET applications. This behavior might be explained by resonant impurity states introduced in Section 3.3.2. At low gate voltage, energy level of the carriers is close to resonant impurity levels and probability of spin-flip scattering could be high. On the other hand, carrier has high energy and scattering rate is low at high gate voltage. Since we have found electron-hole asymmetry of transport properties due to the energy of resonant impurity state in Section 3.3.2, we may also expect the asymmetry on phase coherence. However, we cannot find a hint of asymmetry in Fig. 4.9. The reason is for now unclear and more direct observation of spin related properties could provide clearer understandings, part of which we will show in subsequent Section. We here note that Ref. [113] shows similar experiments using pristine graphene and finds a saturating behavior of L_ϕ at about one order smaller temperatures ($\sim$ 0.1 K). The L_ϕ on order of 1 μm is about one order larger than our results and another work using fluorinated graphene

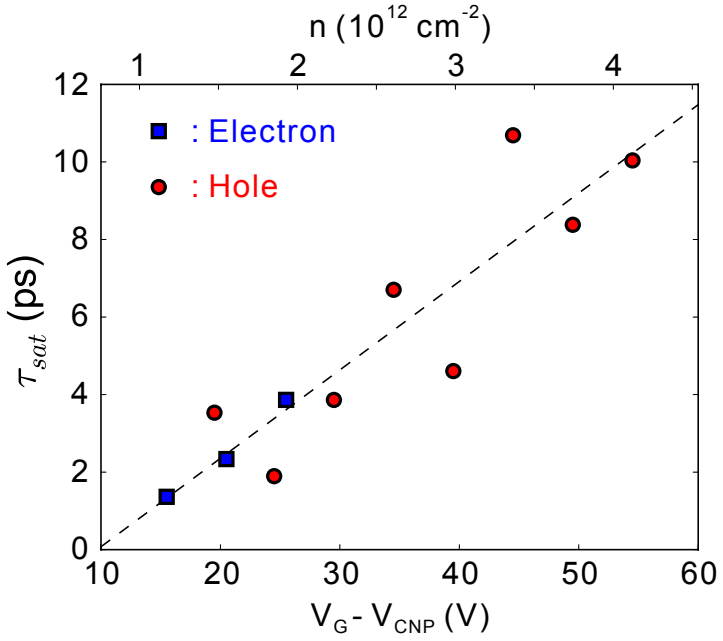

Figure 4.9: Gate voltage (carrier density) dependence of τ_{sat}.

($L_\phi \sim 100\ \mu$m).[33] Lower L_ϕ might be regarded as a degradation of graphene properties, however, our result clarified the role of impurities as a limiting factor of spin relaxation, which was one of the possible explanations in Ref. [113].

4.2 Non-local resistance and spin Hall effect

As introduced in Sec. 1.4.2, impurities can contribute not only to spin relaxation but also to another spin-related effect, the spin Hall effect. It is theoretically shown that point(-like) defect on graphene can cause resonant skew scattering that results in large spin Hall effect.[44] Experimental evidence of this extrinsic spin Hall effect is shown by non-local resistance measurements using hydrogenated graphene.[43] It should be important to see if this effect appear in fluroinated graphene as well because fluorine has been shown to have asymmetric impurity states with respect to charge neutrality point (Sec. 3.3.2).

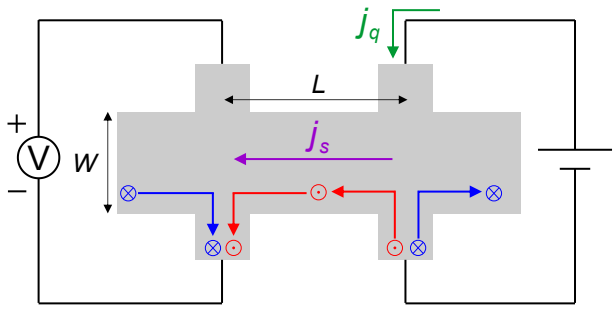

Figure 4.10: Schematic of the experimental setup for non-local resistance detection of spin Hall effect.

4.2.1 Device structure and measurement system

We set up the experiment as shown in Fig 4.10. In this experiment, fixed current is passed through a terminal pair of the Hall bar device and voltage at another terminal pair is measured. Non-local resistance R_{NL} is defined as follows.

$$R_{NL} = V/j_q \tag{4.4}$$

Since there should be current distribution spreading toward voltage probes, there is insignificant contribution, namely Ohmic contribution, in non-local resistance. The Ohmic contribution is written as,

$$R_{Ohmic} = \rho e^{-\pi L/W}, \tag{4.5}$$

where ρ, L and W are resistivity (sheet resistance), length between two terminal pairs, and width of the Hall bar. If there exists the spin Hall effect, charge current is converted to transverse spin current (spin Hall effect), and then converted to charge current again at voltage probe (inverse spin Hall effect). This additional current will result in additional voltage and non-local resistance.

The Hall bar used for this experiment is similar to that in previous section (4.1), except that graphene is patterned into well-defined structure by electron beam lithography and O_2 plasma etching, before electrode deposition. Optical micrograph of the device and measurement setup is shown in 4.11. Measurements were performed with the device in a vacuum probing system from at room temperature down to at 85 K (same one used in Chapter 3). Since the voltage signal will be small, lock-in amplifier is used for this measurement. Sinusoidal excitation current with low frequency (1 Hz) from one lock-in amplifier is applied to the device through current limiting

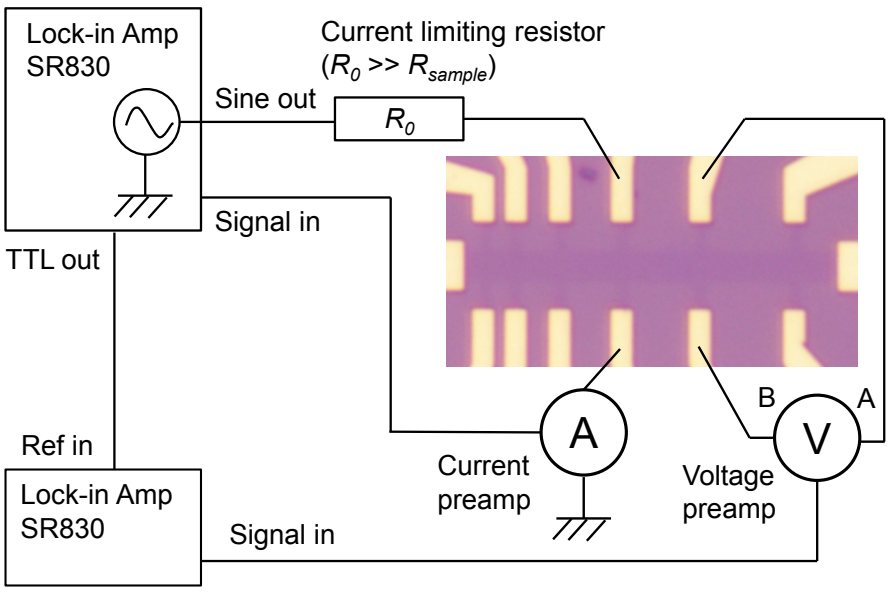

Figure 4.11: Optical micrograph of the fluorinated graphene Hall bar device and measurement setup for non-local resistance measurement.

resistor. The non-local voltage is picked up by a low noise preamplifier and detected by another lock-in amplifier in synchronization with the first one. Measurements of conventional four terminal resistivity are also conducted using the same setup.

Raman spectrum of the fluorinated graphene channel of the device is shown in Fig. 4.12. Estimation of the fluorine concentration (same as previous section) results in fluorine density of 4×10^{11} cm^{-2} or fluorine-to-carbon ratio of 0.01 %. Fluorination condition is same for the device in previous section, however, fluorine concentration might be reduced during extra lithography process for O_2 etching.

Figure 4.13 shows conventional resistivity of the device. Since fluorine concentration is lower, the resistivity is lower than the device in previous section and is always lower than $1/(2e^2/h)$. Thus, we can assume that this device maintains metallic conduction over all gate voltages.

4.2.2 Non-local resistance

Measured non-local resistance as a function of gate voltage is shown in Fig. 4.14. We can see that non-local resistance (R_{NL}) is greater than estimated Ohmic contribution (R_{Ohmic}) at gate

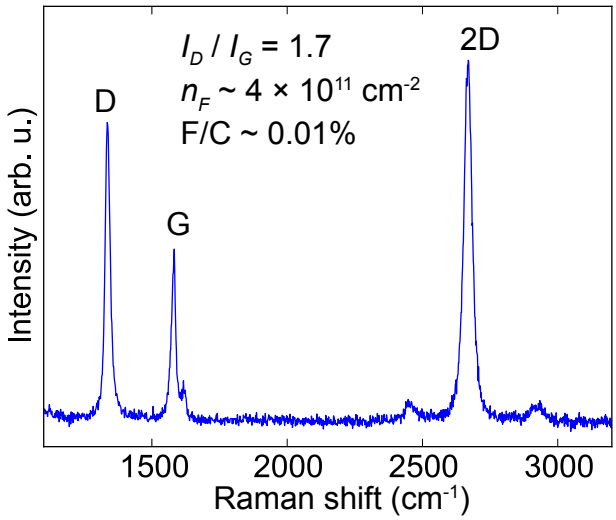

Figure 4.12: Raman spectrum of the fluorinated graphene channel of the Hall bar device used for non-local resistance measurement.

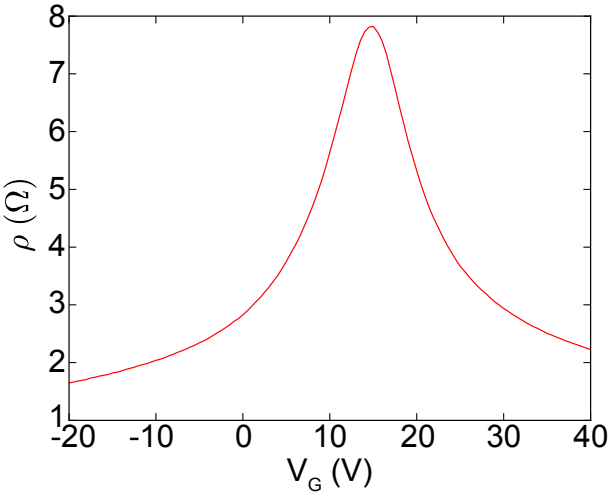

Figure 4.13: Four terminal resistivity of the fluorinated graphene Hall bar device as a function of gate voltage at room temperature.

voltage over ~ 15 V. To clarify the difference, the ratio of additional non-local resistance to sample resistivity ($(R_{NL} - R_{Ohmic})/\rho$) is also shown. Here we identify V_{CNP} as gate voltage that shows maximum resistance. According to a theory, non-local resistance due to the spin Hall effect can be written as[114]

$$R_{NL}^{SHE} = \frac{1}{2}\gamma^2 \rho \frac{W}{L_s} \exp\left(-L/L_s\right). \tag{4.6}$$

Here γ and L_s are spin Hall angle and spin relaxation length, respectively. Since we could observe the same characteristics for different lengths (L) using different terminal pairs in the Hall bar device, we can fit the scaling of non-local resistance with L.

Figure 4.15 shows the scaling characteristics at gate voltage of $V_G - V_{CNP} = 2.0$ V, around which R_{NL} exhibits maximum value. Data can be fitted to Eq. 4.6, yielding L_s about 680 nm (300 K) or 950 nm (85 K) and $\gamma \sim 0.6$ for both temperatures. Resultant spin relaxation length seems to be reasonable considering that $L_s \gtrsim 200$ μm was estimated for the device in previous section and this device has lower fluorine concentration than that. Spin Hall angle is similar to the values found in hydrogenated graphene.[43] This value is one order larger than that of Pt (about 0.01[45]) and very promising if it is true. However, there is unignorable possibility that these results contain spurious contributions to R_{NL} due to, for example, the inhomogeneity of sample resistance or geometry.

Hanle effect can be used to evince the existence of spin Hall effect and give more reliable estimation of the parameters. We have actually tried to observe the Hanle effect, however, it was very difficult to distinguish the Hanle effect from magnetoresistance due to weak localization effect. The quantum sensing using NV center, which we start to describe from subsequent chapter, may provide in the future a tool to overcome these problems and to show a stronger evidence of spin Hall effect in graphene. (possible experiment design will be shown in Sec. 8.2.1)

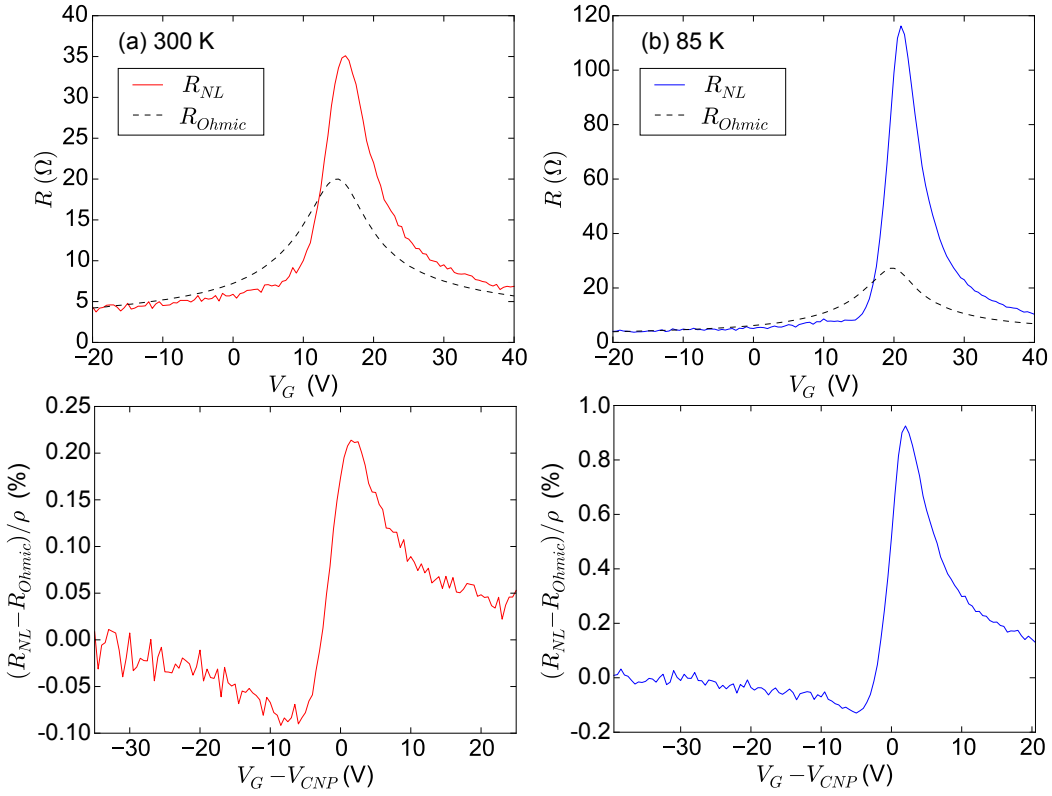

Figure 4.14: Non-local resistance as a function of gate voltage at (a) 300 K and (b) 85 K. Dashed lines are estimated Ohmic contribution (R_{Ohmic}). Solid lines are measured non-local resistance (R_{NL}). The device dimensions are $W = 2$ μm and $L = 3.8$ μm.

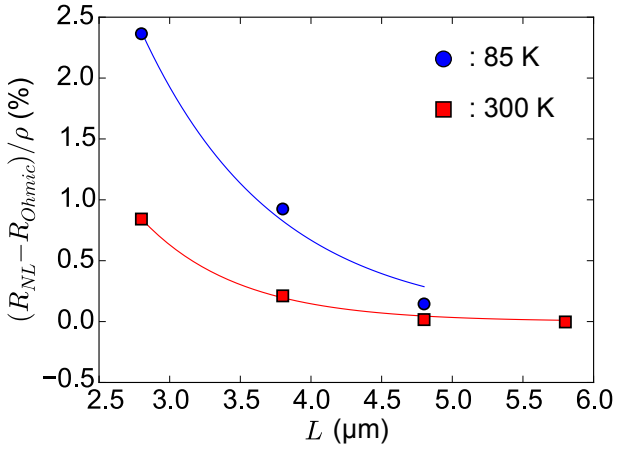

Figure 4.15: Scaling of non-local resistance with the length (L) at a gate voltage $V_G - V_{CNP} = 2.0$ V.

Chapter 5

Diamond micro-structure for photon collection efficiency improvement

In this chapter, we propose a new position-defined top-closed umbrella-shaped structures for photon collection efficiency improvement. The umbrella-shaped diamond micro-structure is formed by a bottom-up fabrication method utilizing the selective and anisotropic growth through holes in a metal mask.[115–117] The umbrella-shaped structure has an effect similar to solid immersion lens (SIL), i.e., it reduces the chance of total reflection at the upper surface and focuses the emitted light toward upper side of the structure.[118, 119] The metal mask also serves as a self-aligned mirror which further enhances the collection efficiency by reflecting the light at the lower surface of the structure.

5.1 Simulation

First, we compare the collection efficiency of the emissions from a single NV center in bulk, pillar-shaped, and proposed umbrella-shaped diamond using three-dimensional finite difference time-domain (FDTD) simulations. Figure 5.1 shows the analyzed structures and their electric field maps for emission at a wavelength of 637 nm (ZPL of the NV^- center). In the planar view, the pillar and the umbrella-shaped structures have 4-fold rotational symmetry and the light source (NV^- center) is located at the center. The depth of the light source is 600nm from the top of the structure. The pillar- and umbrella-shaped structures (Figs. 5.1 (b) and (c)) have the Ti metal

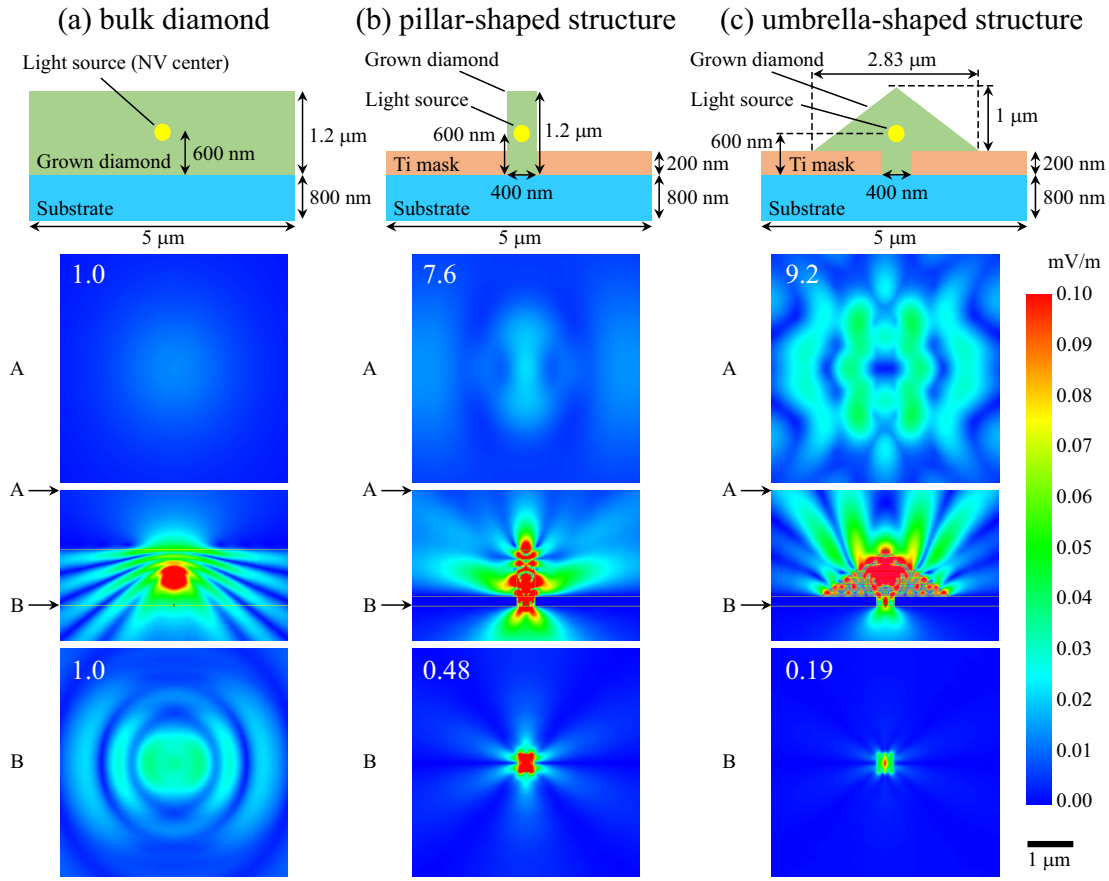

Figure 5.1: Schematic images of analyzed objects and electric field maps calculated by FDTD simulations of (a) bulk diamond, (b) pillar-shaped structures, and (c) proposed umbrella-shaped structures. Cross-sectional schematics, planar field maps at the height A, cross-sectional maps, and planar maps at the height B are shown from top to bottom.

mask. In the simulation, we assume that the reflectivity of the interface between Ti and diamond is 100%. The umbrella part possesses the 111 crystal faces, leading to a top angle of 109.5°. This is the best angle among possible growth modes which can be easily grown by controlling α parameter as explained below.

We analyze the field intensities at the plane located at 1.5 μm above the light source (labeled "A" in Fig. 5.1), and at the boundary between the grown diamond and the substrate (labeled "B"). When we normalize the electric field intensity by that of the view plane A of the bulk diamond, the intensity increases to 7.6 and 9.2 for the pillar-shaped and the umbrella structure, respectively.

On the other hand, at the view plane B, the corresponding values are 1.0, 0.48, and 0.18 for bulk, pillar, and umbrella, respectively. As we have expected, the umbrella-shaped micro-structure can collect the emitted light at the upside more effectively than the pillar-shaped structure. Note that anisotropic spatial distributions of the field maps originate from interference effects, which depend on the wavelength and the shape of the diamond micro-structure. The reason why the distribution has a line symmetry in the planar view rather than a 4-fold rotational symmetry is that the electric field of the wave source is oscillating along one axis.

5.2 Fabrication process

The umbrella-shaped diamond structures were fabricated by microwave plasma chemical vapor deposition (MPCVD) on a type-Ib (001) single-crystal diamond substrate. A 200-nm-thick Ti mask with circular patterns of 400 nm to 50 μm in diameter was formed on the substrate by electron beam lithography. We also designed a bulk region without the Ti mask on the same substrate for the reference. The diamond micro-structures were grown through the mask patterns for 10 h with 1% CH_4 and 50 ppm N_2 gases mixed in H_2 gas. The growth temperature and pressure were 650 °C and 5 kPa, respectively.

Figure 5.2 (a) shows the growth process of the micro-structure. First, diamond is synthesized upward on the exposed diamond substrate until the top surface reaches the height of the Ti mask. Then, it starts to grow also laterally to form the micro-structure. Here, we realized the umbrella-shape by controlling the α parameter,[120] expressed as

$$\alpha = \sqrt{3}\frac{V_{001}}{V_{111}}, \tag{5.1}$$

where V_{001} and V_{111} are growth rates on the (001) and (111) faces, respectively. We used an α parameter close to 3 to enhance the growth towards the [001] direction. Under this condition, the (001) top face tends to disappear, while the (111) faces appear as the diamond grows, resulting in an umbrella-shaped structure. Figure 5.2 (b) shows a scanning electron microscopy (SEM) image of a diamond micro-structure grown through a 400 nm Ti mask pattern which works as a mirror self-aligned to the diamond structures. Note that the handle of umbrella is not seen in Fig. 5.2 (b), because the Ti mask was not removed. In this study, all the observations and optical measurements are done with the mask.

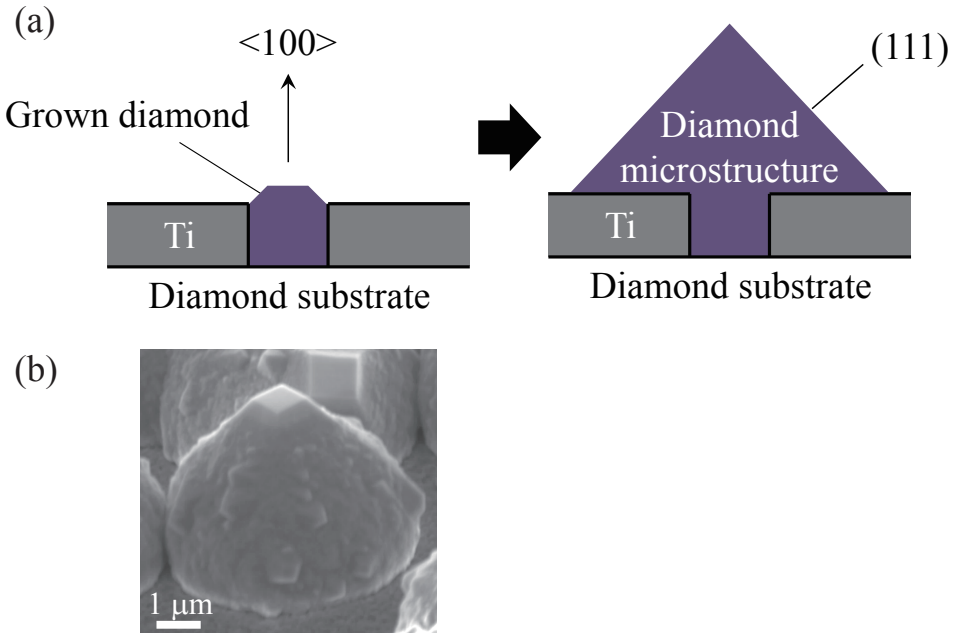

Figure 5.2: Fabrication process of an umbrella-shaped diamond micro-structure using the crystal anisotropy. (b) SEM image of a diamond micro-structure containing NV centers grown from 400 nm Ti mask pattern.

5.3 Measurement results

5.3.1 Confocal microscopy

Confocal microscopy measurements were performed to experimentally confirm the improvement of the photon collection efficiency. Details of the microscope is presented in Appendix B. Figure 5.3 shows SEM and confocal microscopy images of the micro-structures grown through the 400 nm, 1 μm, and 20 μm pattern holes. As shown in the SEM images (top panels), the large patterns (1 and 20 μm) possess flat top surfaces, where significant improvement of the photoluminescence intensity is not obtained since the center of the structure is almost equivalent to the bulk diamond. Note that slight enhancement of the intensity is seen at the tapered edge of the structure. On the other hand, diamonds grown through the 400 nm holes (Fig. 5.3 (a)) become the expected umbrella shaped structure with sharp top edges. The enhancement of the luminescence intensity is clearly seen in the confocal confocal microscopy microscopy images. The maximum photon count rate of the 400 nm structure (6.4 Mcps) is 3 times higher than that of bulk diamond (2.1-2.2 Mcps).

5.3.2 Photoluminescence spectrum

The increase of the photoluminescence intensity in the small sharp micro-structures was further confirmed by the measurements of the spectra in a wider wavelength range. Figure 5.4 (a) shows photoluminescence spectra from the NV centers in bulk diamond and in micro-structures grown with the 400 nm, 1 μm, and 50 μm mask patterns. A sharp Raman peak from the diamond lattice appears at 573 nm. The ZPL of the NV centers is seen at 637 nm, accompanied by the broad phonon side band. In addition, we observe the ZPL of neutral NV (NV^0) centers at 575 nm with its phonon side band. The overall intensity increased significantly as the structure size decreased. In order to study the dependence of the overall photoluminescence intensity on the structure size, we integrated each spectrum in Fig. 5.4 (a) from 575 nm (where the ZPL of the NV^0 center appeared) to 700 nm. Figure 5.4 (b) shows the integrated intensity as a function of the pattern size. It can be seen that the intensity for the 5-50 μm structures was similar to that for the bulk diamond (1.1×10^6 counts). Therefore, 5 μm or larger structures are ineffective for collecting photons at the top part of the structures. On the other hand, the intensity for the 400 nm structure was 5.6×10^6 counts, which is about 5 times higher. By the FDTD simulation as shown in Fig. 5.1, the collection

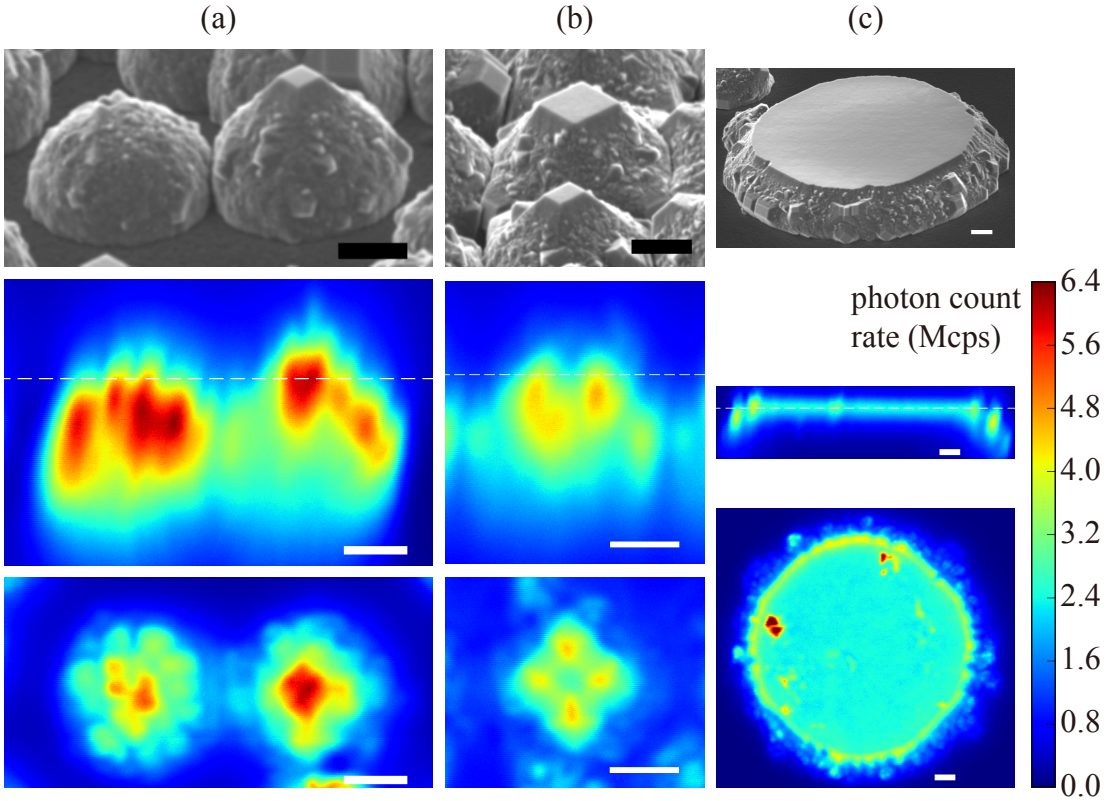

Figure 5.3: SEM images (top), cross-sectional (middle), and planar (bottom) confocal microscopy images of the diamond micro-structures grown through (a) 400 nm, (b) 1 μm, and (c) 20 μm patter holes. The bottom planar images are taken at the height indicated by dotted lines in corresponding cross-sectional images. All scale bars are 2 μm. All confocal micrographs are taken with the laser power of 0.1 mW.

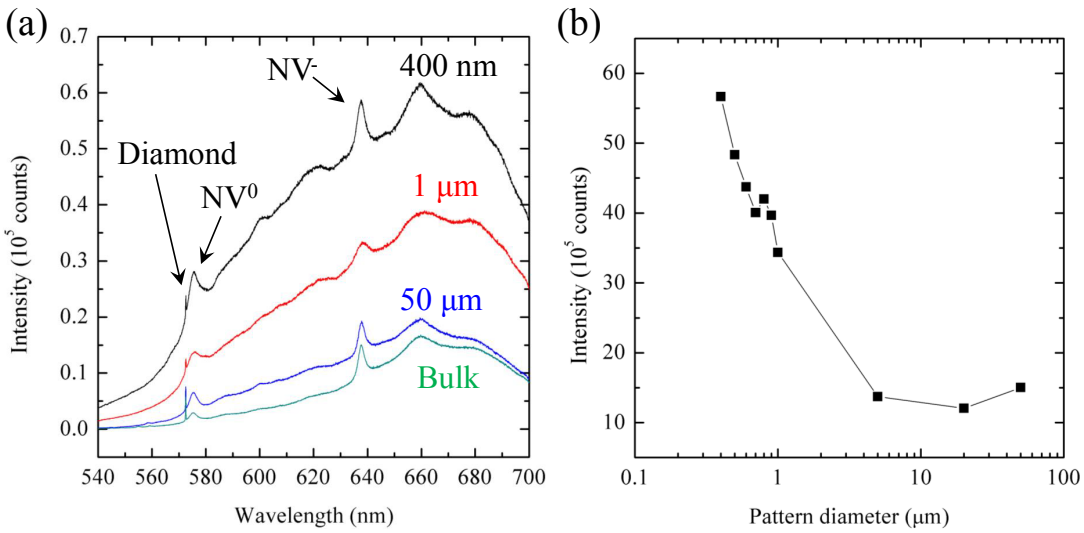

Figure 5.4: (a) photoluminescence spectra emitted from NV centers in 400 nm, 1 μm, and 50 μm micro-structures and bulk diamond. (b) Integrated photoluminescence intensity as a function of pattern size. Integration was performed within the wavelength range from 573 nm to 700 nm.

efficiencies for 1000, 800, 600, and 400 nm, are 5.1, 7.5, 7.8, and 9.2 (Fig. 5.1 (c)), respectively. This is qualitatively consistent with the experimental results shown in Fig. 5.4 (b).

5.4 Discussion

The improvement of the photon collection efficiency observed by the confocal microscopy and photoluminescence experiments is lower than the value predicted by the FDTD simulation. This would originate from the rough surface of the 400 nm micro-structure. As seen in the SEM images (top panel in Fig. 5.3 (a)), the micro-structures have a number of protruding facets on the surface due to secondary nucleation during the CVD process. The protrusions cause light scattering to random directions, which degrades the photon collection efficiency. Thus, further enhancement of the photon collection efficiency is expected by optimizing the CVD growth conditions. From the viewpoint of photonics, one of the best structures for photon collection from a NV center is the SIL structure.[118, 119] The collection efficiency obtained by similar FDTD simulation for a hemispherical SIL structure is 10.0. This is slightly larger than that of the umbrella-shaped structure (9.2). However, the SIL structure cannot be formed by the bottom-up crystal growth but by the

top-down etching. The etching may cause damages to the diamond crystal and deteriorate the NV center characteristics. On the other hand, since our umbrella-shaped diamond micro-structure is formed by the crystal growth avoiding the damages, we might be able to achieve an ideal structure in terms of both photonics and crystal quality, with further optimizations.

Chapter 6

Selective alignment of high density NV center ensemble

As mentioned in Sec. 1.7.2, we shall show the fabrication and characterization of CVD diamond containing selectively aligned high density NV centers. The quantification of the alignment ratio of ensemble NV centers is not straightforward because we cannot determine the alignment of individual NV centers optically[85, 121] or by ODMR.[83–85] In this chapter, we estimate the alignment ratio of ensemble NV centers along the [111] direction in (111) diamond by ensemble ODMR measurements. The measurement is calibrated by NV centers in high-pressure high-temperature (HPHT) diamond.

6.1 Materials and methods

For calibration experiments, we use randomly selected ensemble regions in sample HPHT1, a type-Ib (111) diamond synthesized by HPHT method (Sumitomo Electric). In each confocal spot are about 30 NV centers, estimated by comparing photoluminescence intensity with a single NV center. The NV-incorporated diamond films (sample CVD2 and CVD3) are deposited on HPHT Ib (111) diamond substrates by the microwave plasma CVD growth. The substrates are polished with an off-direction of 2° along the $[\bar{1}\bar{1}2]$ (CVD2) or $[11\bar{2}]$ (sample CVD3) direction to promote two dimensional homoepitaxial growth.[122] The CH_4 carbon source of 0.05 % and N_2 of 0.04 % are diluted in H_2 gas. The purities of CH_4, N_2 and H_2 gases are 99.999 %, 99.99995 % and

99.99999 %, respectively. The total gas flow rate was 1000 sccm and the pressure was kept 75 Torr during the growth. A microwave power of 900 W was input and the substrate temperature was kept at 1030 °C (1140 °C) for sample CVD2 (CVD3). A growth duration of 10 hours results in a film thickness of about 3 μm determined by a depth profile of secondary ion mass spectrometry (SIMS). The concentration of the nitrogen atoms in the film and substrate is estimated to be $\sim 10^{19}$ cm^{-3} by SIMS. Confocal microscopy, CW and pulse ODMR measurements are performed using a home-built measurement system presented in Appendix B.

6.2 Definition for alignment ratio quantification

Our problem is how to find the alignment ratio using ODMR. Since we expect the selective alignment of NV centers along the [111] direction, a static magnetic field (B_0) of about 25 G is applied perpendicular to the substrate (along the z axis in Fig. 6.1 (a)). As shown in Fig. 6.1 (d) and (e), ODMR signals appear at resonant frequencies of $f_\pm = D \pm \gamma B_0 \sim 2.87 \pm 0.07$ GHz for NV centers along the [111] axis, and frequency of $f_\pm = D \pm \gamma B_0 \cos\theta \sim 2.87 \pm 0.02$ GHz for NV centers along the other three axes.

Here we define the estimated alignment ratio along the [111] direction by

$$R_{[111]} = S_{[111]} / \left(S_{[111]} + k S_{other} \right) \tag{6.1}$$

where $S_{[111]}$ and S_{other} is ODMR signal areas from NV centers along the [111] and the other three axes, and k is the factor to correct signal differences attributed to causes other than the selective alignment. Fitting of ODMR signals is done using Lorentzian functions (3 components for each line) for $S_{[111]}$ and Voigt functions for S_{other}. The center frequencies of the 3 Lorentzians are separated by about 2.2 MHz, which is the energy level split by hyperfine interaction with ^{14}N nucleus[123]. Voigt functions are used to relax the effect of broadening due to misalignment of the static magnetic field. If all NV centers in a confocal spot is under the same condition, k will be 1. However, we will find that k should be carefully determined.

6.3 Calibration experiments using HPHT diamond

6.3.1 Effect of microwave field direction

First, the effect of the microwave direction should be noted. The ODMR signal strength (or Rabi frequency) is dependent on the magnitude of microwave magnetic field which is perpendicular to the NV axis.[52] Therefore, NV centers aligned along different axes may be driven by microwave field with different strength. Two ODMR spectra measured at the same position (Fig. 6.1 (d) and (e)) clarify this effect. Spectrum in Fig. 6.1 (d) is taken under microwave magnetic field (B_{MW}) nearly perpendicular to the substrate (Fig. 6.1 (b)), which is radiated from 2-turn loop coil. (The coil is intentionally mis-aligned from perfect perpendicularity.) On the other hand, the spectrum in Fig. 6.1 (e) is taken under in-plane B_{MW} configuration (Fig. 6.1 (c)), where microwave is radiated from a microwave wire placed just below the laser spot. $S_{[111]}$ becomes much smaller than S_{other} when the microwave is nearly perpendicular to the substrate because the projection of microwave magnetic field to the xy plane is less. We should use ideally a microwave direction which drives all NV centers with equal strength (e.g. [100] direction). However, due to technical difficulty, the in-plane magnetic field (Fig. 6.1 (c)) is used hereafter.

6.3.2 Microwave field difference in in-plane configuration

The unit vector parallel to an in-plane B_{MW} can be written as $\hat{\boldsymbol{b}} = (\cos\phi, \sin\phi, 0)$. The projection of B_{MW} to the plane perpendicular to an NV axis is given by $B_1 = B_{MW}|\hat{\boldsymbol{b}} \times \hat{\boldsymbol{d}}_{\boldsymbol{NV}}|$, where $\hat{\boldsymbol{d}}_{\boldsymbol{NV}}$ is the unit vector along an NV axis. For NV centers along [111] direction ($\hat{\boldsymbol{d}}_{\boldsymbol{[111]}} = (0, 0, 1)$), B_1 is independent of ϕ and equal to B_{MW}. B_1 for the other three direction is dependent on ϕ, however, the average value of the three (B_1^{other}) has weak ϕ dependence. B_1^{other} is periodic function of ϕ with period of $\pi/3$ and takes maximum (minimum) value of $0.72B_{MW}$ ($0.70B_{MW}$) at $\phi = \pi/6$ ($\phi = 0$).

The difference of B_1 field is confirmed by measuring Rabi oscillations. Figure 6.2 (a) shows the optically detected Rabi oscillations for NV centers along the [111] and the other three directions. The fitting by sinusoidal curves with exponential decay shows a frequency ratio of 16 MHz/22 MHz = 0.73, in good agreement with the expected value of B_1^{other}/B_{MW}. We note that the ODMR spectra are taken under the laser and microwave power condition so that the signal

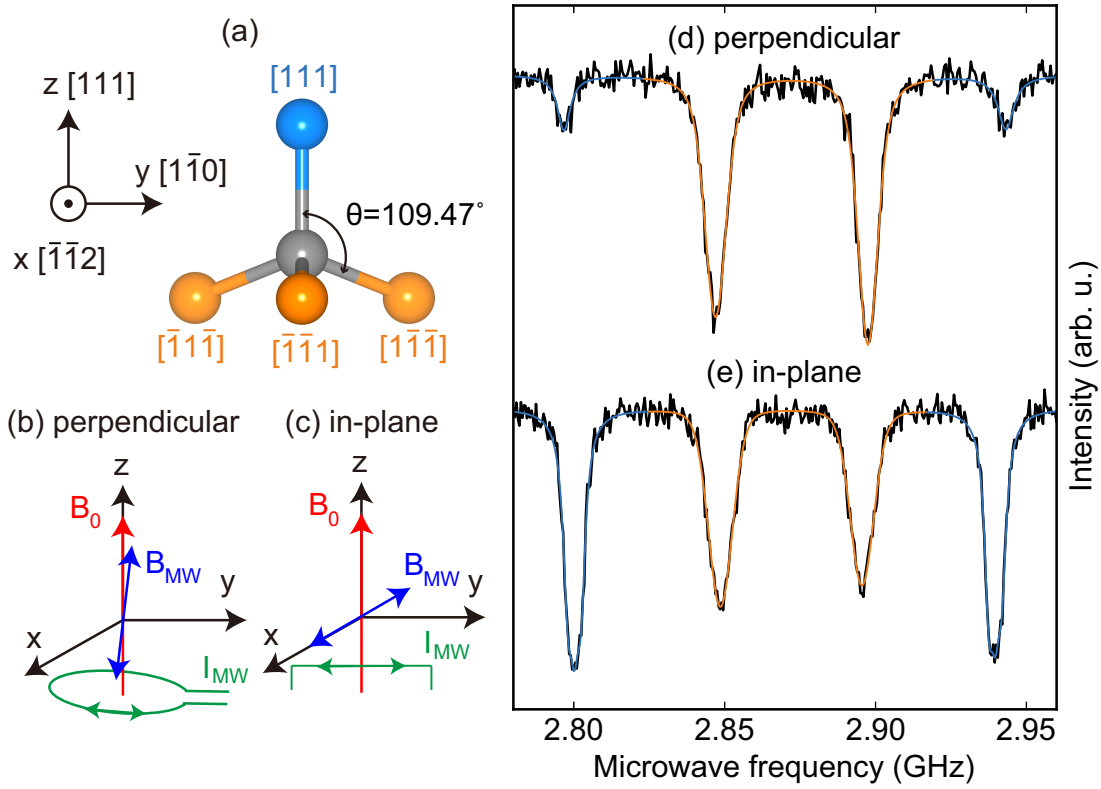

Figure 6.1: (a) Definition of the coordinate system and schematic model representing four possible NV center axes in single crystal diamond. The surface of (111) substrate corresponds to xy-plane. (b) Schematic description of direction of static (B_0) and nearly perpendicular microwave (B_{MW}) magnetic field radiated by loop coil. (c) Schematic of in-plane B_{MW} radiated by a microwave line. (d) ODMR spectrum of ensemble NV centers in HPHT diamond (sample HPHT1) under nearly perpendicular B_{MW} configuration. (e) ODMR spectrum under in-plane B_{MW} configuration. Both ODMR spectra are taken with a laser power of 0.5 mW.

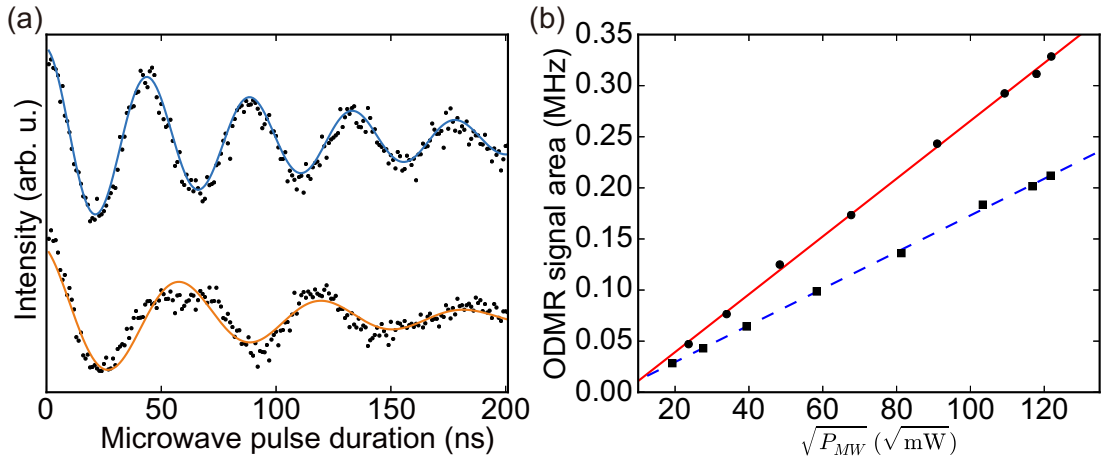

Figure 6.2: (a) Optically detected Rabi oscillations of sample HPHT1. Upper curve is $|m_s = 0\rangle \leftrightarrow |-1\rangle$ transition of NV centers along [111]. Lower curve is the same transition of NV centers along other 3 directions. (b) Dependence of ODMR signal area on square root of microwave power passed through the microwave line. Square (circle) symbols are data of sample HPHT1 (CVD2).

area scales linearly with B_1. As shown in Fig. 6.2 (b), we see linear dependence of the signal area on the square root of the microwave power ($\sqrt{P_{MW}}$). Since $\sqrt{P_{MW}}$ is proportional to B_1 and Rabi frequency, $k = B_{MW}/B_1^{other} = 1.4$ can be assigned in Eq. (6.1) to include the difference of B_1. Here weak ϕ dependence of B_1^{other} does not appear at the first decimal place of k.

When $k = 1.4$ is used, the alignment ratio in sample HPHT1 is estimated to be $R_{[111]} = 44 \pm 1\%$. This value is average over 7 values extracted from ODMR spectra taken at the independent ensembles in sample HPHT1 (including the spectrum in Fig. 6.1 (e)). The obtained alignment ratio is seemingly too high if we expect the random distribution (25%) of the alignment in the untreated HPHT substrate. One possible reason of this discrepancy could be the difference in optical excitation. Since the electric dipole lies in the plane perpendicular to the axis,[124] NV centers along [111] can interact more efficiently with electric field of the laser light propagating toward perpendicular direction to the substrate. Indeed several groups have reported stronger photoluminescence from single NV centers along the [111] axis than the other three.[85, 121] However, since it is difficult to selectively excite the ensemble NV centers in one confocal spot, quantitative estimation of this effect is out of scope of this work.

We resort to the use of an empirical parameter for k instead. A good empirical parameter,

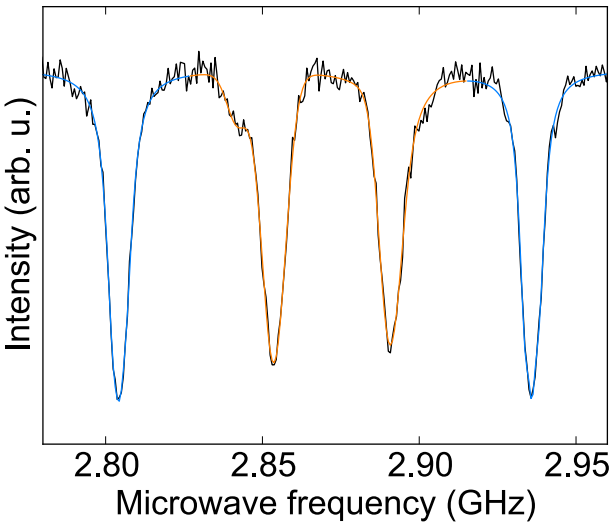

Figure 6.3: ODMR spectrum of electron-beam irradiated HPHT diamond. The fitting of signals from NV centers other than [111] is conducted using two Voigt functions per each line.

specific to our experimental setup, turns out to be $k = 3.3$ which leads to the alignment ratio of 25 ± 1% for sample HPHT1. We use $k = 1.4$ based on B_1 difference to estimate the upper bound of alignment ratio, and empirical $k = 3.3$ for the lower bound. Note here we also find the same value for the alignment ratio (within standard deviation shown above) in another HPHT sample containing much denser NV centers ($> 10^{17}$ cm^{-3}) after treatments. The type-Ib HPHT diamond is irradiated to the electron-beam (dose 10^{12} cm^{-2}) and annealed at 1000 °C for 60 min. The spectrum of this sample is shown in Fig. 6.3. Analysis of peak area yields alignment ratios between $R_{[111]} = 24.6\%$ ($k = 3.3$) and $R_{[111]} = 43.4\%$ ($k = 1.4$).

6.4 Selective alignment in CVD-grown diamond

CVD-grown films contain NV centers with higher density than the substrate, as shown in a cross-sectional confocal microscopy image (Fig. 6.4 (a)). The photoluminescence spectrum (Fig. 6.4 (b)) indicates that most of the NV centers are in the negatively-charged state under 532 nm laser excitation. On average, the intensity is about 170 times larger than that of a single NV center. The NV center density over 1×10^{15} cm^{-3} is obtained by dividing this value by volume of point spread function of the microscope. For detailed description of point spread function, see Appendix B.2.

Table 6.1: Density and alignment ratio of NV centers in each sample.*

Name	Density (10^{15} cm^{-3})	$R_{[111]}$ (%, k = 3.3)	$R_{[111]}$ (%, k = 1.4)
HPHT1	0.32†	25 ± 1	44 ± 1
CVD2	1.6 ± 0.8	84 ± 4	93 ± 2
CVD3	1.4 ± 0.3	76 ± 2	88 ± 1

More detailed values for each samples are in Table 6.1.

Figure 6.4 (c) shows a typical ODMR spectrum of sample CVD2. Signals from NV centers along three axes (S_{other}) is significantly smaller than that of sample HPHT1 (Fig. 6.1 (e)). The alignment ratio estimated using this spectrum is in a range from 81% (k = 3.3) to 91% (k = 1.4). Summarized in Table 6.1 are values averaged over multiple spectra for each sample. Although the selective alignment is not perfect in the CVD samples, we can expect at least 3 fold improvement of the alignment (75%) on randomly distributed NV centers. The effect of the selective alignment is still larger than (110) and (100) diamonds (2 fold improvement). The reason why we end up with the imperfect selective alignment could be imperfection of the growth mode. As recently shown by theoretical calculations, the two dimensional step-flow growth is important for the selective alignment.[125] The perfect two dimensional growth results in atomically flat surface of the grown film.[122] However, our CVD-grown films have relatively rough surfaces with root mean square roughness of 8.5 nm (sample CVD2) or 23 nm (sample CVD3). Some nucleations on terraces could occur due to the catalytic effect of nitrogen.[126, 127] Further optimization of the growth condition is required for the perfect alignment by the nitrogen doped CVD growth.

*Variations are in standard deviation.

†Averaged value over only ensemble regions used for ODMR measurements.

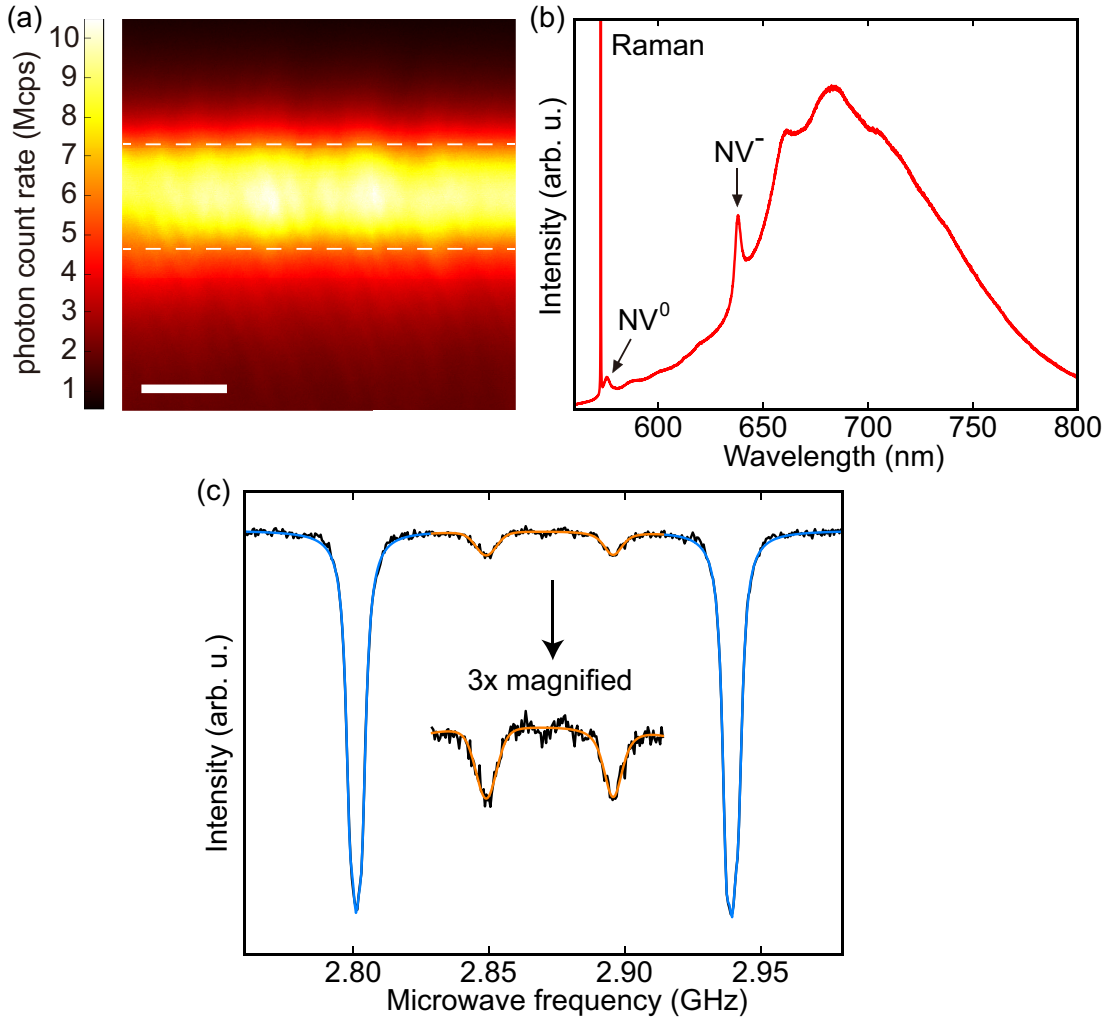

Figure 6.4: Properties of the CVD-grown film (sample CVD2). (a) Cross-sectional confocal microscopy image under a laser power of 0.35 mW. Upper (lower) dashed line indicates boundary between the film and air (substrate). Scale bar is 2 μm. (b) photoluminescence spectrum under 532 nm excitation. Arrows indicate zero phonon lines of neutral (NV^0) and negatively charged (NV^-) NV centers. (c) ODMR spectrum under in-plane B_{MW} and a laser power of 0.5 mW.

Chapter 7

AC field magnetometry using NV center ensemble

In this chapter, we present the realization of our ensemble NV centers as AC magnetometer using pulse ODMR measurements.

7.1 Materials and methods

We compare AC magnetometer performance using four different types of NV centers in (111)-oriented diamond crystal. Two of the four are NV center ensembles in our CVD-grown films. A sample denoted by "CVD2" has already presented in Chapter 6. As summarized in Table 6.1, this sample has NV density over 1×10^{15} cm^{-3} and alignment ratio over 80 %. Another CVD-grown sample named "CVD1" is grown under conditions similar to CVD2, but different microwave power (550 W) and substrate temperature (800 °C) in order to control growth mode. NV center ensemble in this sample showed higher NV density over 1×10^{16} cm^{-3} and alignment ratio over 99 %. Alignment ratio over 99 % means we could not find any ODMR signal from NV centers along axes other than [111] (S_{other}), for over 10 identical ODMR experiments, signal-to-noise of which is much greater than 10. Further details on characterizations of this sample and discussion on growth mechanism will be presented elsewhere.[128]

The other two types of NV center are the NV center ensemble fabricated by ion implantation, and a grow-in single NV center. Both of the two are in a undoped CVD-grown film on (111)-

oriented type-Ib diamond crystal. Growth was performed using a reactor different from the one used for doped CVD films (CVD1 and CVD2). H_2, CH_4 and O_2 gases were introduced at rates of 998, 2 and 0.5 sccm, respectively. The total gas pressure was kept 150 Torr during the growth. A microwave power of 3.5 kW was input and the substrate temperature was kept at 704 °C for a growth duration of 5 hours. SIMS measurement revealed impurity atom concentrations less than 1×10^{16} cm^{-3} for nitrogen and 1×10^{15} cm^{-3} for boron. The grow-in single NV center (named "Single" in this Chapter) is a isolated NV center along [111] axis, which should be formed by incorporation of residual nitrogen during the growth. To form NV center ensemble (named "Implant"), ion implantation and annealing was performed, only for a part of the substrate. $^{14}N^{2+}$ ions are implanted with 350 keV acceleration energy and a density of 1×10^{12} cm^{-2}. A Monte Carlo simulation* result in the depth-distribution of implanted nitrogens in a range about 100 nm centered at about 340 nm from the surface. Substrate temperature was kept at 600 °C during implantation process. After the implantation, substrate was annealed at 750 °C for 30 min in vacuum. Vacancies in the crystal diffuse and convert substitutional nitrogen into NV center during annealing process. The other part of the substrate, which "Single" is in, was kept intact by a mask during implantation process.

Basic physical concepts of the pulse ODMR procedure have been introduced in Sec. 1.6. Experiments are performed using the measurement system presented in Appendix B. For high density NV center ensembles ("CVD1", "CVD2" and "Implant"), NV centers in one confocal spot (volume ~ 0.1 μm^3) is involved in each measurement.

7.2 Characterization of basic parameters

For pulse ODMR magnetometry, it is necessary to characterize the basic parameters of NV centers in detail. The basic parameters are spin-state detection contrast and the spin coherence time. The detection contrast is how much difference of photoluminescence intensity is appeared by the change of spin state populations. As discussed in Sec. 1.6.5, this is a linear scaling factor of magnetometer sensitivity. On the other hand, sensitivity scales as square root of spin coherence time T_2.

*Simulation is performed using SRIM software. http://www.srim.org/

7.2.1 Rabi oscillation and contrast

Rabi oscillation measurement is the first step of pulse ODMR measurements. In this experiment, we apply microwave pulses with different durations in between initialize and readout laser pulses. The spin state is polarized to $|m_s = 0\rangle$ immediately after laser pulse. Since a resonant microwave pulse flips the spin state at certain frequency (Rabi frequency), oscillation can be observed when we plot the photoluminescence intensity of NV centers versus microwave pulse durations.

The result of Rabi oscillation measurement is shown in Fig. 7.1.

All of the three NV center(s) show clear oscillations at the frequency about 11 MHz (angular frequency of 70 MHz). The oscillation is fitted to a decaying sinusoidal function.

$$I = \frac{C}{2} \cos\left(\Omega_R \tau\right) \exp\left(-\frac{\tau}{T_R}\right) \tag{7.1}$$

Fitting parameter here is the contrast C, Rabi (angular) frequency Ω_R and time constant of the decay T_R.

We can find obvious difference in the contrast. Single NV centers show the best contrast $C = 30\%$. This value is the typical value in literature, determined by intrinsic property of NV center. The use of ensemble NV centers generally degrades the contrast. Implanted ensemble NV centers has contrast of $C = 8\%$, which is about a quarter of 30%. This degradation is reasonable because we expect random alignment of implanted ensemble. Since we are performing the ODMR on only a quarter of NV centers in the ensemble, the contrast becomes a quarter as well. The reminder (three quarters) of NV centers only contribute to unwanted back ground photoluminescence. In contrast, the CVD-grown ensemble shows much higher contrast of $C = 19\%$. The reason is the selective alignment in CVD-grown ensemble. For sample CVD1, alignment ratio along [111] determined by CW-ODMR measurement is almost perfect (100 %). Alignment ratio and contrast of sample CVD2 are over 84 % and $C = 21\%$ respectively. The ratio of the contrast of CVD samples to that of single NV center are about 60-70 % and smaller than alignment ratio. One possible the reason of this discrepancy is the background light from NV^0 centers. As in the luminescence spectrum (Figure 6.4 (b)), CVD samples contain NV^0 center as well. Although ODMR experiments are performed with 633 nm LPF to reduce the luminescence from neutral centers, there will be some contribution to total luminescence background. The other possibility is inhomogeneity of static or microwave magnetic field. Inhomogeneity will result in detuning of Rabi oscillation or slight

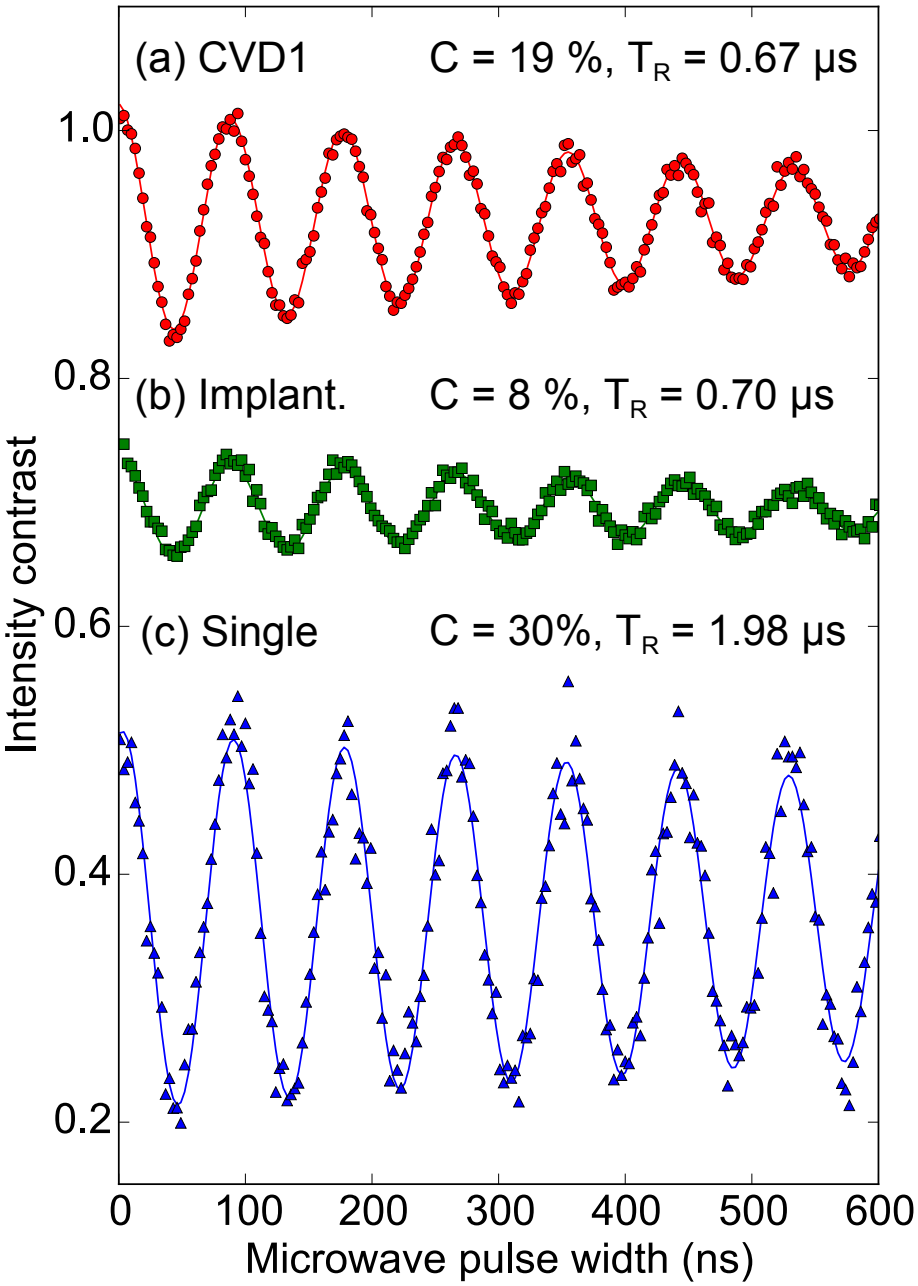

Figure 7.1: Optically detected Rabi oscillation of ensemble NV centers in (a) CVD grown films and (b) Implanted layer. (c) Rabi oscillation of a grow-in single NV center.

change of Rabi frequency for some part of NV centers. If oscillation we observe is the averaged one over individual oscillation with small frequency fluctuations, its amplitude will be smaller than each component oscillation. If this assumption is true, a better contrast for ensemble NV center is achievable in the future by a better instrumentation for magnetic field generation. T_R has some correlation with coherence time, however, more accurate determination should be done by spin echo measurement.

7.2.2 Spin echo and coherence time

Free induction decay (FID) measurement is the simplest method to characterize the coherence property. FID measurement is performed following the standard protocol introduced in Sec. 1.6.1. First, the spin state is initialized by a laser pulse and the $\pi/2$ pulse of resonant microwave, to realize superposition state. And then the spin system is freely evolved during certain time (free evolution time τ). Finally, the coherence is converted into population difference by another microwave $\pi/2$ pulse, and read out optically under subsequent laser pulse.

Fig. 7.2 shows the result of FID experiment. The signal decays exponentially as Eq. 7.2.

$$P = \frac{1}{2} + \frac{1}{2}\exp\left[-\left(\frac{\tau}{T_2^*}\right)^n\right] \tag{7.2}$$

Here T_2^* the coherence time. It is well-known that this T_2^* is shorter than intrinsic coherence time T_2 because of static field inhomogeneity or other low frequency noises.

We can extract nearly intrinsic value of coherence time T_2, by spin echo measurement. Spin echo measurement is different only by additional π pulse during free evolution. The signal decays also exponentially, as Eq. 7.3.

$$P = \frac{1}{2} + \frac{1}{2}\exp\left[-\left(\frac{2\tau}{T_2}\right)^n\right] \tag{7.3}$$

We can see over one-order difference in coherence time comparing Fig. 7.2 and Fig. 7.3 (a). The difference between the samples should be noted here. CVD-grown samples have high nitrogen concentration of 10^{19} cm^{-3}. Electron spin bath of the substitutional nitrogen (P1 center) should limit the coherence.

Implanted ensemble and single NV center is in substrate with lower nitrogen concentration. In very pure sample, the coherence is limited by nuclear spin bath of ^{13}C, and has value of about 600

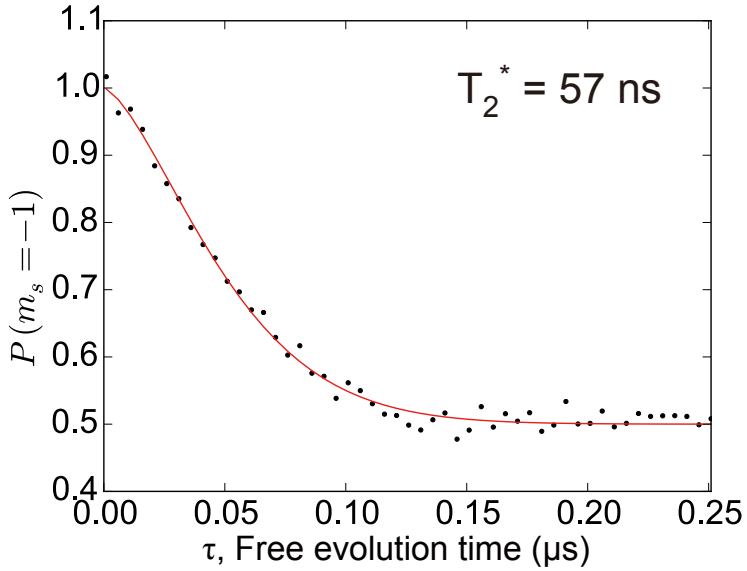

Figure 7.2: Optically detected FID of ensemble NV centers in CVD grown film (CVD2)

μs. What limits the value within about 11 μs is currently unknown, but should be impurity other than nitrogen, substrate strain or effect of surface.

7.2.3 Performance estimation

As noted in Sec. 1.6.5, we have to increase parameters including photon count rate ($R \propto n$), contrast (C), and coherence time (T_2), to improve magnetometer sensitivity. All required parameters are determined by pulse ODMR measurements in this section. Here we define the estimated achievable sensitivity which should be proportional to the minimum detectable field (in fixed acquisition time) as $\eta_{est} = 1/C\sqrt{RT_2}$. The parameter values and η_{est} are summarized in Table 7.1. Since actually available sensitivity is dependent on the whole sensor system (measurement scheme or noise sources), η_{est} is normalized with respect to the value of single NV center. Although T_2 of CVD samples are lower than that of implantation and single NV center, better sensitivities (η_{est}) are expected because of high contrast and photon count rate. Next section, we will see actual performance of these samples as magnetometer.

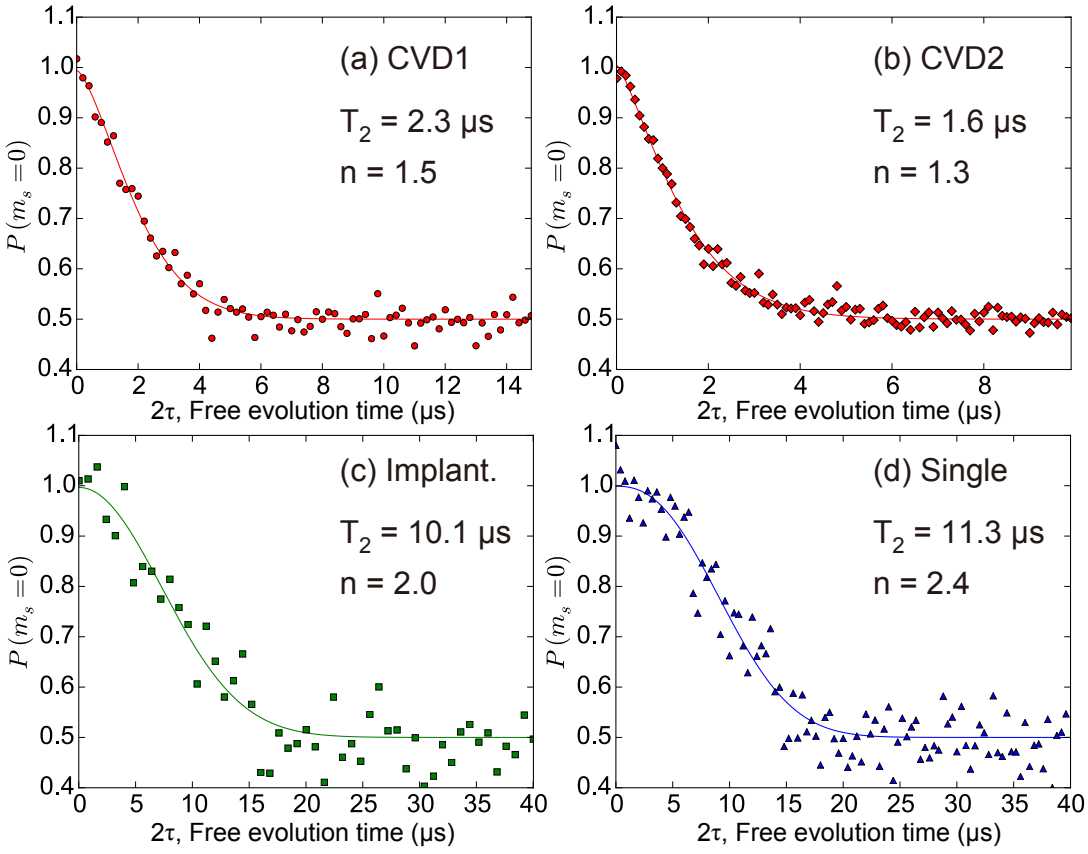

Figure 7.3: Optically detected spin echo decay of ensemble NV centers in (a) sample CVD1, (b) CVD2 and (c) Implanted layer. (d) Spin echo decay of a grow-in single NV center.

7.3 AC magnetometry using dynamical decoupling sequences

Magnetometry based on pulse ODMR can be performed using various microwave pulse sequences introduced in 1.6.5. Although we have to use FID to pick up the effect of DC field, a better sensitivity can be expected using spin echo for the measurement of AC field. We shall present AC field sensing using dynamical decoupling sequences, which is multi-pulse extension of spin echo, to show the best possible performance. AC field to be measured is generated by a coil fixed near the sample.

7.3.1 Car-Purcell-Meiboom-Gill sequence

Car-Purcell-Meiboom-Gill (CPMG) sequence consists of multiple π pulses as illustrated in Fig. 7.4 (a). We hereby denote the two quadrature microwave phases using x or y. Microwave with x (y) phase rotates the Bloch vector around x (y) axis in our rotating frame. The main parameters of CPMG measurement are inter-π pulse evolution time (τ) and number of π pulses (N). The most effective AC field detection, $\tau + t_\pi$ should coincide with half period of AC field, where t_π is duration of the π pulse. We start by the output characteristics in such exact synchronization with AC field ($\tau + t_\pi = 1/2f$) and see the dependence on number of pulses N. AC field frequency of $f = 1.5625$ MHz and π pulse width of $t_\pi = 44$ ns will be used unless otherwise noted.

When AC field is written as $B_{AC}(t) = b_{AC} \sin(2\pi f t + \phi_{AC})$, spin states will accumulate phase difference $\Delta\Phi = (N\gamma b_{AC}/\pi f)\cos(\phi_{AC})$, after a sequence.[129] Since initial π pulse has phase x, $\Delta\Phi$ can be depicted as the angle between Bloch vector and y axis (Fig. 7.4 (b)). Maximum detection efficiency is reached if the phase of AC field is locked to the microwave pulse trains as shown in Fig. 7.4 (a). This phase-locking means that ϕ_{AC} is always zero and $\Delta\Phi$ remain unchanged over many measurement shots. We can use the last $\pi/2$ pulse, which maps the accumulated phase into population difference, with phase either x or y. The results using x readout (Fig. 7.4 (c)) is presented in Fig. 7.5. In this case, the signal can be fitted to following equation.

$$P = \frac{1}{2} + A\cos\left(\frac{N\gamma b_{AC}}{\pi f}\right)\exp\left(-\frac{N}{\nu}\right) \tag{7.4}$$

Here ν is a decay parameter, which should have correlation with coherence properties (T_2 and n in Eq. 7.3). However, we treat this ν as a simple fitting parameter instead of going on physical details.

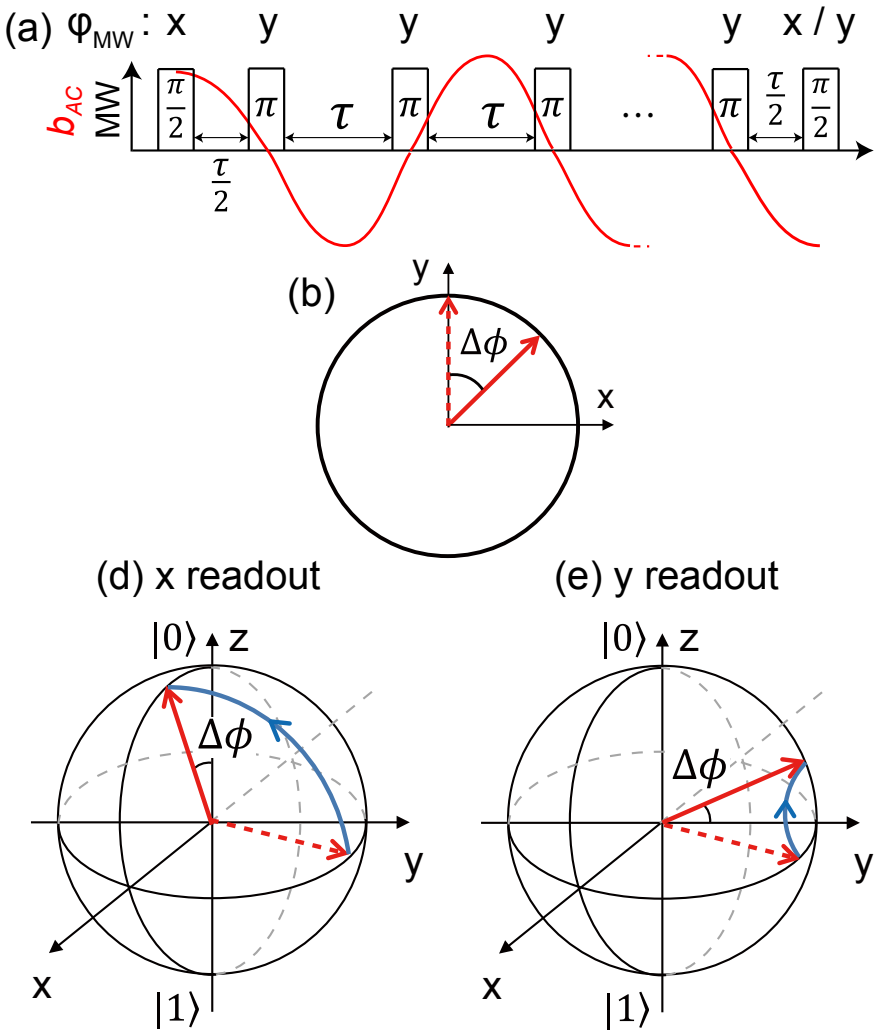

Figure 7.4: Schematic of CPMG sequence and readout methods. (a) Microwave pulse timings and phases. (b) Accumulated phase just before the last $\pi/2$-pulse. (c) Final state using x readout (d) Final state using y readout.

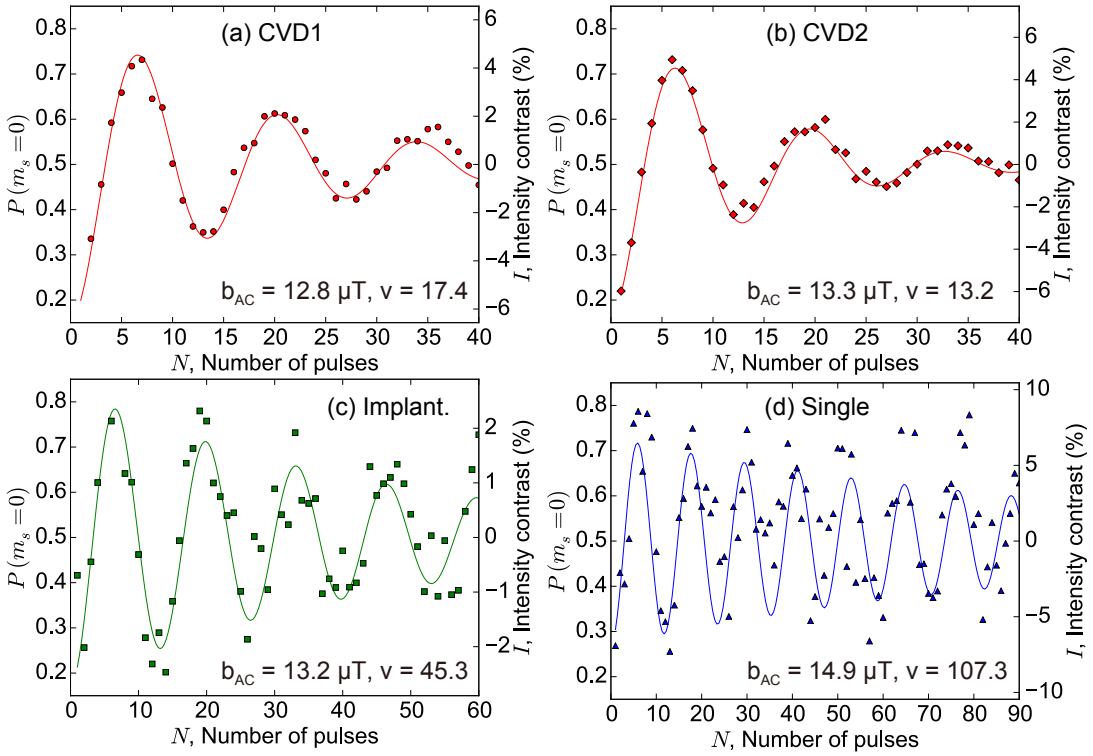

Figure 7.5: Evolution of CPMG signals (x readout) with number of pulses under external AC magnetic field of ensemble NV centers in (a) sample CVD1, (b) CVD2 and (c) Implanted layer. (d) CPMG signals of a grow-in single NV center.

When we use y readout (Fig. 7.4 (d)), output becomes a sine function.

$$P = \frac{1}{2} + A \sin\left(\frac{N\gamma b_{AC}}{\pi f}\right) \exp\left(-\frac{N}{\nu}\right) \tag{7.5}$$

The outputs for this case is shown in Fig. 7.6. This y readout is meritorious for the detection of small magnetic field, because slope near zero of sine function is steeper than that of cosine.

The AC signals with random phase (ϕ_{AC}), i.e., not synchronized with the microwave pulse trains, can also be detected. Accumulated phase $\Delta\Phi$ becomes random among measurement shots as depicted in Fig. 7.7 (a). Assuming ϕ_{AC} is completely random, the average Bloch vector over many measurement shots will lie on y-axis. The information of AC field amplitude is however ascribed to the "shortening" of average Bloch vector. In this case, we can only use x readout (Fig. 7.7 (b)) rather than y readout (Fig. 7.7 (c)), because y readout cannot map any information onto

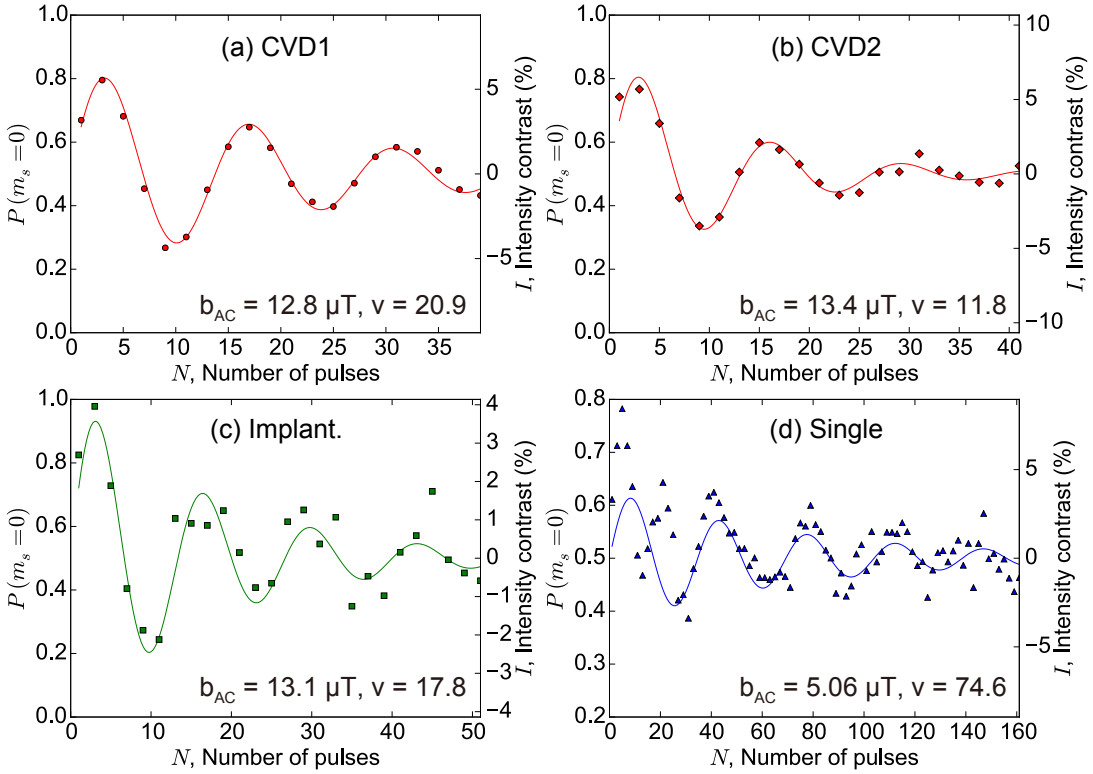

Figure 7.6: Evolution of CPMG signals (y readout) with number of pulses under external AC magnetic field of ensemble NV centers in (a) sample CVD1, (b) CVD2 and (c) Implanted layer. (d) CPMG signals of a grow-in single NV center.

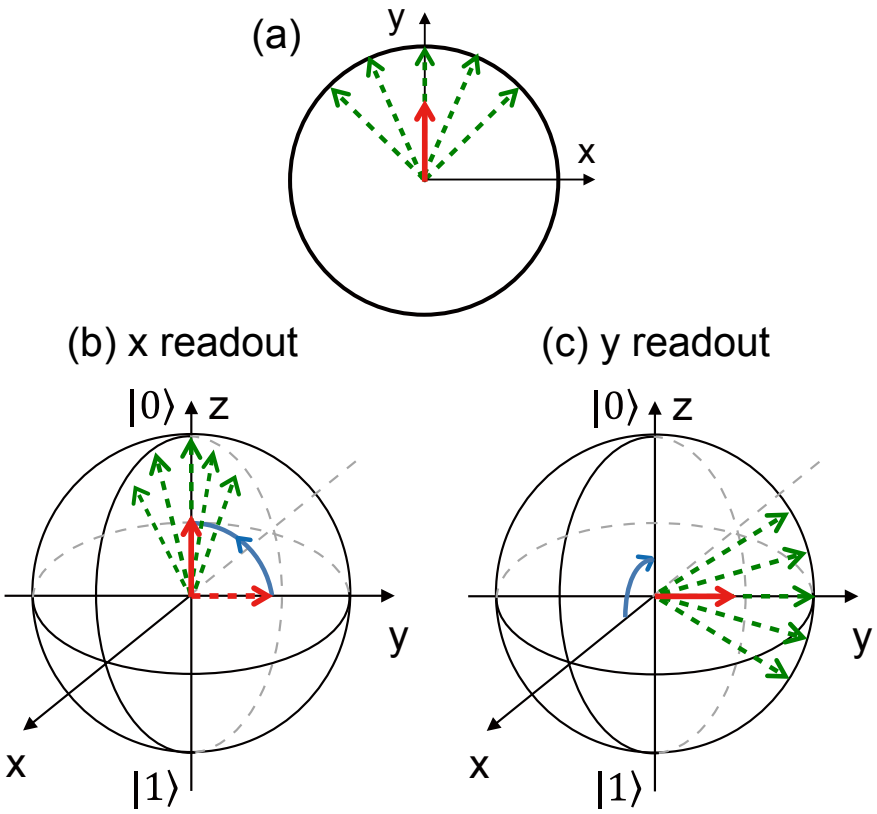

Figure 7.7: Schematic of readout methods for asynchronous AC field. (a) Randomly accumulated phase just before the last $\pi/2$-pulse. (b) Final state using x readout (c) Final state using y readout.

population difference. Formally, the expected signal can be written as

$$P = \frac{1}{2} + A\left\langle \cos\left(\frac{N\gamma b_{AC}}{\pi f}\cos\phi_{AC}\right)\right\rangle_{\phi_{AC}} \exp\left(-\frac{N}{\nu}\right) \tag{7.6}$$

$$= \frac{1}{2} + AJ_0\left(\frac{N\gamma b_{AC}}{\pi f}\right)\exp\left(-\frac{N}{\nu}\right), \tag{7.7}$$

where $\langle\rangle_{\phi_{AC}}$ and J_0 means average over ϕ_{AC} and zeroth-order Bessel function of first kind. The result is shown in Fig. 7.8. We can see that the experimental results is well fitted to the equation above. The detection of AC field with random phase is important for applications like nano-NMR[3–5], though detection efficiency is not as good as phase locked case.

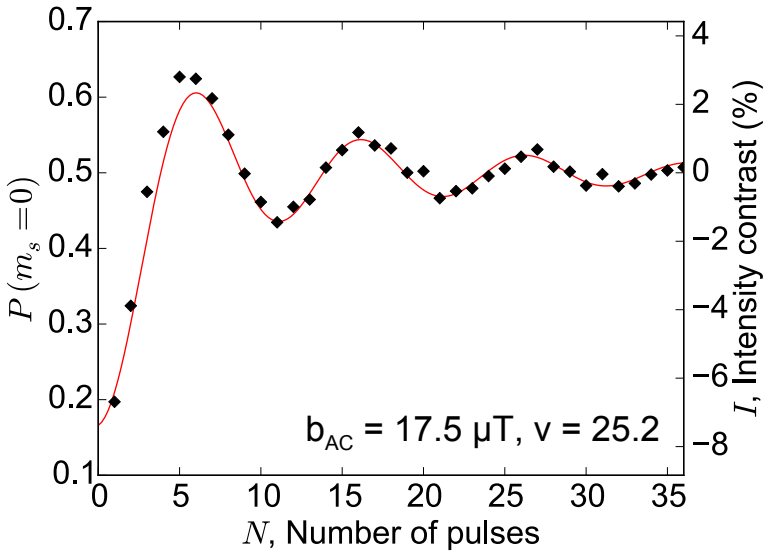

Figure 7.8: Evolution of CPMG signals with number of pulses under external AC magnetic field for ensemble NV centers in CVD2. AC magnetic field is not synchronized with π-pulse trains (random phase).

7.3.2 XY8 sequence

Recent research works show that XY8 pulse sequence can result in better AC field detection performance than CPMG because this sequence can compensate pulse error more effectively. Because we can only choose integer multiple of 8 for number of pulses for XY8 measurement, we can not get smooth curve like Fig. 7.5 by sweeping number of pulses. Phase locked AC field and y readout are used in what follows unless otherwise noted.

We will show τ dependence, instead of N dependence in Figure 7.9. In this figure, τ is converted into the frequency $f = 1/2(\tau + t_\pi)$. Two different frequencies are applied and detected as the change of NV center's spin state (intensity). This kind of frequency selectivity is important for spectroscopic applications like NMR. The same output could be obtained using CPMG sequence, however, we have found that XY8 sequence have better signal-to-noise ratio. The capability to pick up signals in narrow frequency band is one of the advantages of dynamical decoupling sequences

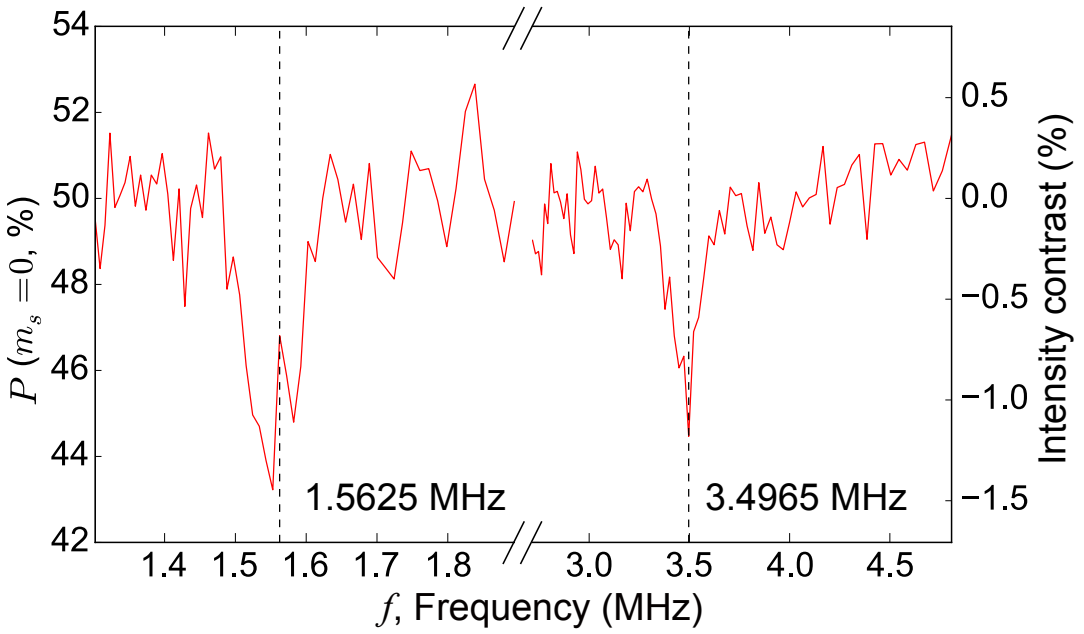

Figure 7.9: Frequency domain output of XY8 magnetometer using sample CVD2 for two different AC frequencies. Number of pulses $N = 24$.

over simple spin echo. The response to arbitrary magnetic field ($B(t)$) can be written as[6, 130]

$$I = A \int df \mathcal{B}(f) W_N(f,\tau)\, e^{i2\pi f t} \tag{7.8}$$

$$W_N(f,\tau) = \frac{1-\sec(\pi f \tau)}{2\pi\tau f} \sin(2\pi N f \tau), \tag{7.9}$$

where $\mathcal{B}(f)$ is Fourier transform of $B(t)$ and $W_N(f,\tau)$ is the filter function. Assuming $B(t)$ is a monochromatic sinusoid with frequency f_0, its Fourier transform is a delta function $\mathcal{B}(f) = B\delta(f - f_0)$ and we can observe the filter function itself. Figure 7.10 shows the frequency domain response of XY8 magnetometry for $f_0 = 1.5625$ MHz and different N. In addition to experimental data, filter function described above ($W_N(f_0,\tau)$) is also shown. We can see good agreements of experimental data with the theory. Obviously, the detection band width can be narrowed by increasing N, however, the practically possible N is limited by the spin coherence. We can actually see smaller signal by using $N = 56$ than $N = 24$ for sample CVD1. Thus, $N = 24$ is more optimized in terms of signal strength for this sample. On the other hand, $N = 72$ shows larger signal than that of $N = 24$ for sample Single, which exhibits better coherence property (greater T_2 or ν).

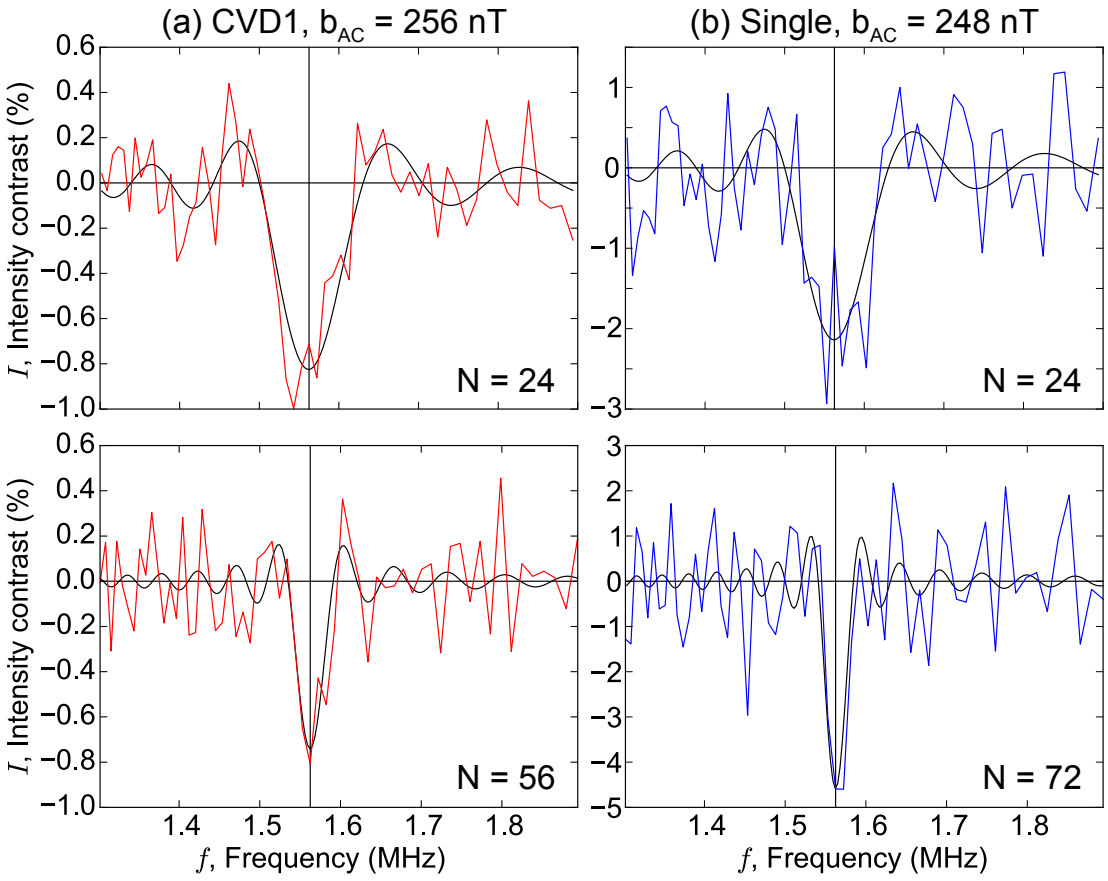

Figure 7.10: Frequency domain output of XY8 magnetometer using sample CVD1 and Single with different number of pulses.

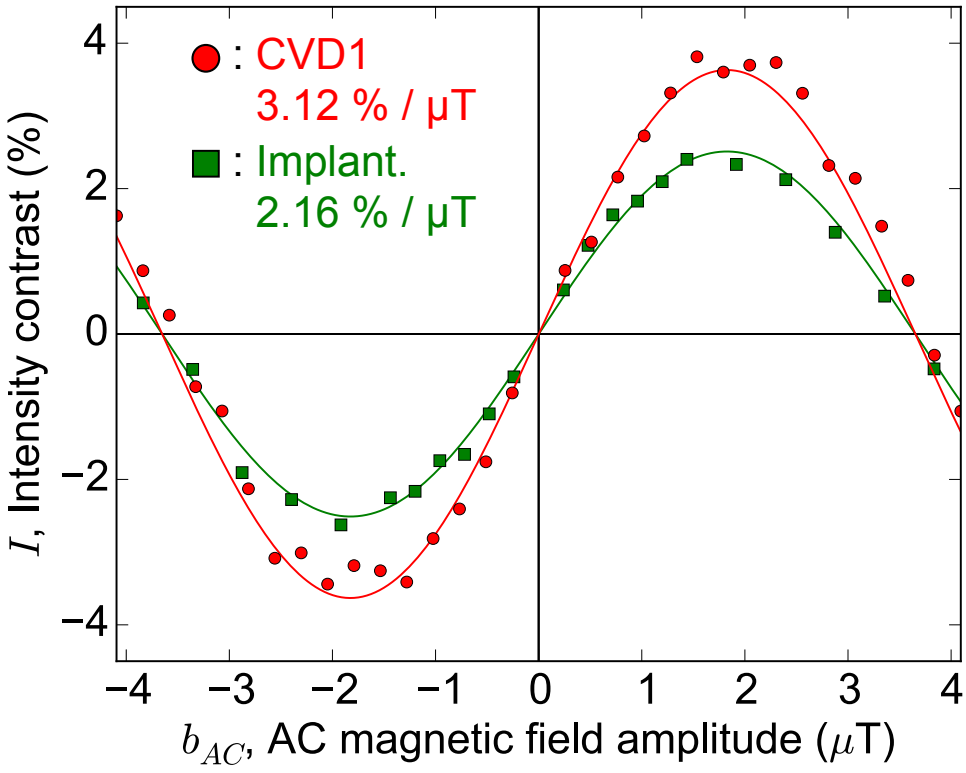

Figure 7.11: Magnetometer output (change of intensity) as a function of AC signal amplitude. Circles (squares) are data for NV centers in sample CVD1 (Implant). $N = 24$ for both.

For the estimation of the maximum possible sensitivity, we have acquired output characteristics as a function of the amplitude of AC signal (b_{AC}). Here, τ is again taken to be $\tau + t_\pi = 1/2f$. As shown in Fig. 7.11, the characteristics follows equation 7.5. The slope of this characteristics in near zero, dI/db_{AC}, has direct impact on the sensitivity. The values are summarized in Table 7.1. Comparing ensemble NV centers, CVD samples mark higher slope than the implantation sample. This result comes from the larger full-scale contrast overcoming the shorter T_2. The single NV center shows the best slope because of its long T_2 and possibly, immunity to homogeneous static or microwave field. As described above, we could get a better slope using larger number of pulses ($N = 72$) for this single NV center.

The magnetometer sensitivity is determined not only by the slope, but also by the noise level. In literatures, the sensitivity has been evaluated in terms of the minimum detectable field in unit

Table 7.1: Photon count rate (R), contrast (C), coherence time (T_2), estimated sensitivity (η_{est}), sensitivity (η_{XY8}) and slope (dI/db_{AC}) of NV centers in each sample. Sensitivity and slope is the values estimated from AC magnetometry operation using XY8 sequence. Pulse number N is 72 for Single, and 24 for the other.

Sample	R (Mcps)	C (%)	T_2 (μs)	η_{est} (arb. u.)	η_{XY8} (nT/$\sqrt{\text{Hz}}$)	dI/db_{AC} (%/μT)
CVD1	33	19	2.3	0.12	34	3.12
CVD2	4.2	21	1.6	0.37	110	2.66
Implant.	0.63	8	10.1	0.99	360	2.16
Single	0.04	30	11.3	1.00	300	20.5

acquisition time (T) as[82, 131]

$$\eta = \delta B_{min}(T)\sqrt{T} = \sigma_I(T)\sqrt{T}/\left(dI/db_{AC}\right), \tag{7.10}$$

where $\sigma_I(T)$ is the fluctuation of intensity in standard deviation. If the source of noise is shot noise, $\sigma_I(T)$ should be proportional to $1/\sqrt{T}$, leading to η independent on T. The $\delta B_{min}(T)$ is shown in Fig. 7.12. We can fit the data as $\delta B_{min}(T) = \eta/\sqrt{T}$ and extract η.

7.4 Discussion

Parameters and performances as AC magnetometer of each NV centers are summarized in Table 7.1. The CVD-grown NV ensemble (CVD1) marked the best performance due to its high photon emission rate (R) and contrast (C), though T_2 is smaller than the other samples.

7.4.1 Toward better sensitivity

Our best sample (CVD1) marked the AC magnetometer sensitivity about 30 nT/$\sqrt{\text{Hz}}$. One typical sensitivity of 30 nT/$\sqrt{\text{Hz}}$ is also demonstrated using single NV center with high T_2 of 600 μs.[132] T_2 of our CVD sample was about 2 μs and should be limited by electron spin of nitrogen. Nitrogen density in the film is 10^{19} cm^{-3} and much higher than NV density of 10^{16} cm^{-3}. Toward better sensitivity we have to maximize NV/N ratio, and thereby maximize NT_2 (N is NV density). For

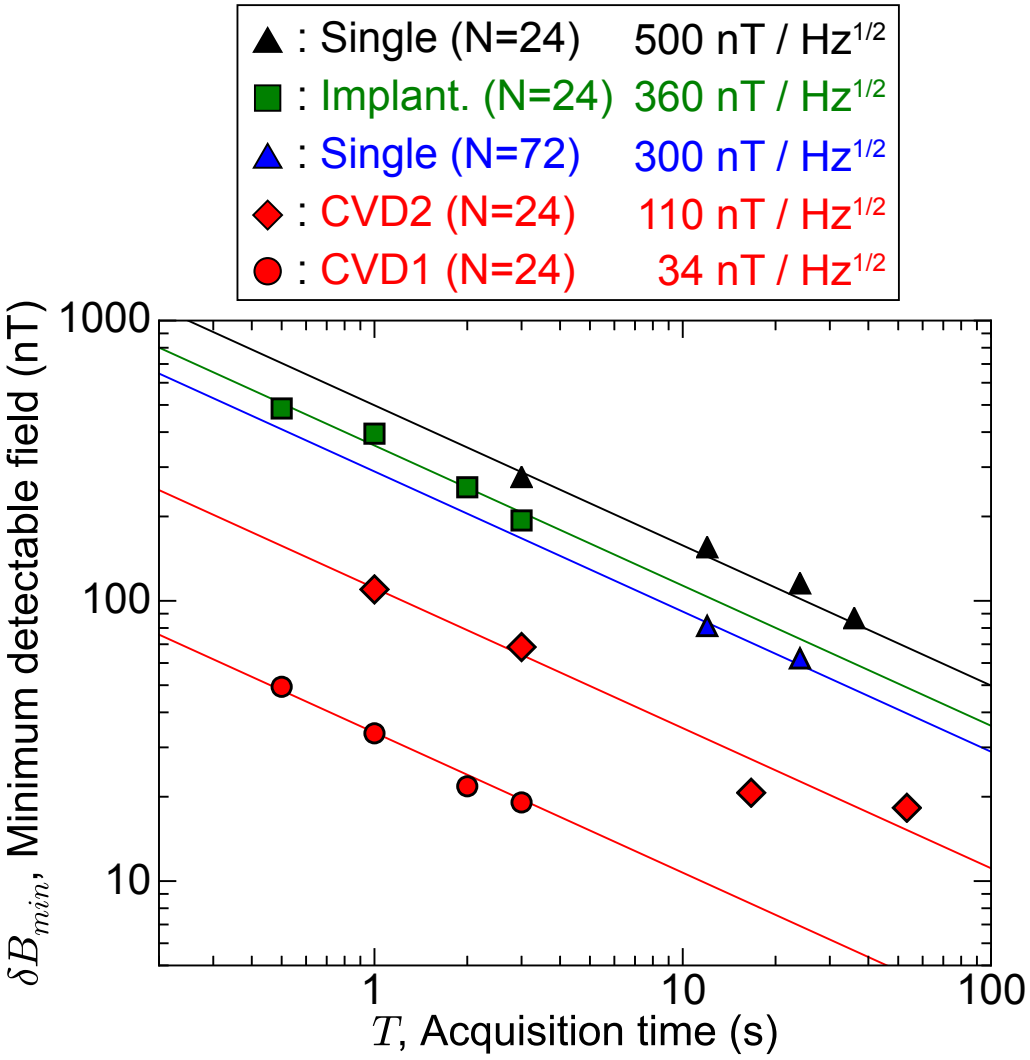

Figure 7.12: Minimum detectable AC field (1.5625 MHz) as a function of total acquisition time using XY8 sequence.

example, NV/N ratio of $\sim$ 10 % (N density of 10^{17} cm^{-3} and NV density of 10^{16} cm^{-3}) could be realized by optimizing growth condition in the future, leading to sensitivity of about 3 nT/$\sqrt{\text{Hz}}$.

Further sensitivity is possible by sacrificing spatial resolution. Recent research reveals that 0.9 pT/$\sqrt{\text{Hz}}$ is possible by using $N \sim 10^{11}$ NV centers in volume of 8.5×10^{-4} mm^3.[133] NV density employed is about 10^{17} cm^{-3} (0.9 ppm), while N density is kept in the same order (3 ppm). Since this research uses NV centers created by electron-beam irradiation, selective alignment is not employed. When CVD-grown ensemble with similar condition is achieved, we can further boost the sensitivity.

7.4.2 Toward NMR applications

NMR and MRI is very important and promising application of NV magnetometry. As introduced in Sec. 1.1, nano or microscopic-scale NMR is the unique application. Latest researches show that the magnetic field fluctuation from nuclear spin samples on (spin noise) diamond surface at distance of about 5 nm is order of 1 μT. The detection of this spin noise using our CVD sample seems to be possible. However, we have to develop δ-doping technique to limit the NV ensemble's distribution within near surface.

Application to conventional NMR would be possible as well. Conventional NMR uses the coil to pick up magnetic field signal of macroscopic magnetization of nuclear spin. The sensitivity is limited by thermal noise on coil and wirings. If we can apply NV center ensemble of large numbers as in Fig. 7.13 to pick up the signal to get better signal to noise, it can contribute to miniaturization of NMR system.

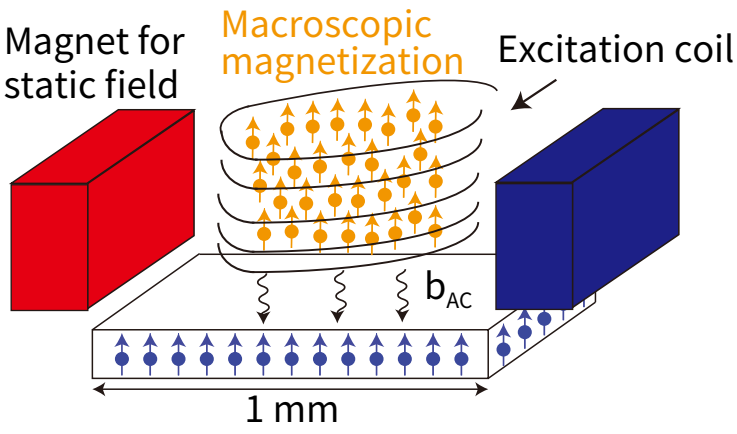

Figure 7.13: Schematic of the application of macroscopic NV ensemble for detection of conventional NMR signal.

Chapter 8

Conclusion and outlook

8.1 Conclusion

In this thesis, we have presented the spin state control of electrons in carbon materials toward quantum sensor applications. Crystalline carbon materials, graphene and diamond, are employed as the platforms of spin state control because of small spin-orbit interaction and lack of nuclear spin in the most abundant isotope (^{12}C). The key for the spin state control is the introduction of paramagnetic impurities. The fluorine impurity controlled the charge and spin current in graphene. The NV center in diamond serves as the localized electron spin state for sensing.

In chapter 2, we have developed fluorination method of graphene using Ar/F_2 plasma. It has been shown that the fluorine concentration was controllable and reversible by characterizations using Raman spectroscopy and XPS.

We have fabricated fluorinated graphene FET devices with different fluorine concentrations and characterized charge transport properties in chapter 3. Resistivities of fluorinated graphene FETs were dependent on fluorine concentrations, and controllable over 3 orders of magnitude at room temperature. Conduction mechanism is also dependent on fluorine concentrations. Metallic conduction like pristine graphene is maintained for low fluorine concentration, while temperature dependence follows variable range hopping mechanism at high fluorine concentration. We have found characteristic electron-hole asymmetry at high fluorine concentration, which could be ascribed to the existence of midgap impurity states. On/off ratio of the device at room temperature is not very different from that of pristine graphene FET. However, the on/off ratio could be enhanced

by using ionic liquid gate.

In chapter 4, we have explored possibilities of spin state control using fluorine impurities. We have used fluorinated graphene FET with lower fluorine concentration, which retains metallic conduction mechanism. Magnetotransport measurements suggest that spin relaxation time could be controllable by one order of magnitude by gate voltages. We have also tried to observe spin Hall effect using non-local resistance measurement of Hall bar device. We found the possibility of the existence of spin Hall effect in fluorinated graphene. However, further evidence should be provided in the future.

Toward quantum sensor application of high density NV center ensemble, we have developed CVD-based fabrication techniques and demonstrated magnetometer action in the latter part of this thesis.

In chapter 5, we have shown self-formed micro-structure for photon collection efficiency improvement. We have proposed a new umbrella shaped micro-structure which has the effect similar to solid immersion lens. The simulation suggested about one-order improvement of photon collection efficiency. We have fabricated the structure using anisotropic CVD-growth and characterized it. The confocal microscopy and photoluminescence spectroscopy measurements revealed about from 3 to 5 times larger luminescence intensity from micro-structure than bulk diamond. These enhancement factor is not as large as the one simulation suggested. Further enhancement should be possible by removing rough surface of the micro-structure.

Chapter 6 is devoted to the selective alignment of high density NV ensemble. We have proposed a quantification method of the alignment ratio based on ensemble ODMR measurement. After calibration measurements using HPHT samples, we have characterized our CVD samples. One of the CVD samples has selective alignment ratio over 80 % and density over 1×10^{15} cm^{-3}.

We have demonstrated the quantum sensor (AC magnetometer) action of our CVD sample in chapter 7. We have also showed results using ensemble NV center fabricated by ion-implantation and a grow-in single NV center for comparison. Important parameters for the sensor performance, contrast, coherence time and luminescence intensity are characterized first. The estimated sensitivity calculated by these parameters suggested that CVD sample can exhibit about one-order better performance than implantation ensemble or single NV. We have characterized sensitivities of AC magnetic field (at frequency of 1.5625 MHz) using dynamical decoupling sequences (CPMG and

XY8). The results were consistent with the estimated sensitivity and CVD sample showed the best performance: sensitivity of 34 nT/$\sqrt{\text{Hz}}$ with XY8 sequence.

8.2 The spin current detector using graphene and diamond

We shall propose the experiments and sensor device application combining the two materials, graphene and diamond, as the outlook of the research. Since graphene can be formed directly on top of atomically flat (111) surface of diamond, compatibility of the two is extremely good.[9]

8.2.1 Sensing spin Hall effect in graphene using NV center

One major problem we have encountered in Ch. 4 is poor reliability of spin Hall effect detection by electrical measurement. The experiment using Hall bar, which we have used in Sec. 4.2, can suffer from inhomogeneity of resistivity in the sample. One of possible solutions is the use of spin injection and detection via inverse spin Hall effect and the observation of Hanle effect. However, Hanle effect experiments have another difficulty to distinguish the effect from magnetoresistivity. Complex device structure and magnetic contamination may also become problems.

The most reliable way to date, which is also employed for one of the earliest demonstration of the spin Hall effect, is spatial resolution and visualization of the accumulated spin using Kerr effect microscopy.[134] However, the Kerr effect microscopy cannot be applied for zero-band gap material like graphene. So we propose, as an alternative of that, spatially resolved sensing of spin Hall effect using NV center as shown in Fig. 8.1. The graphene layer is formed by sublimation of thin NV containing layer in (111) diamond. This fabrication method enable the NV center (sensors) in extreme proximity of graphene layer. The local magnetic field created by accumulated spins in the graphene sample's edge might be detected by NV center, although the discrimination between accumulated spin's field and the field created by charge current is not so easy task.

8.2.2 The spin current sensor

The combination of graphene and NV center would provide more versatile sensor device which can contribute to spin physics and spintronics applications. Provided that graphene is the best charge / spin current channel on top of diamond, the spin current sensor device as shown in Fig.

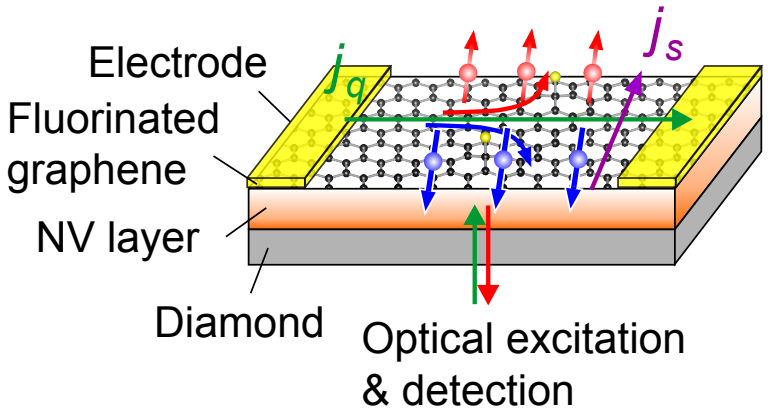

Figure 8.1: Schematic of proposed experiment for spatially resolved detection of spin Hall effect in graphene using NV center.

8.2 is possible. The spin current source of interested forms some junction with graphene and flow a spin current into graphene. And the magnetic moment of spin current is detected by proximal NV centers. In this configuration, graphene itself is not the material under investigation but just a conducting channel. We may use this for investigation for any possible spin current source which can form good contact with graphene. This spin current sensor might open up a new methodology in spin current physics and spintronics applications.

8.3 The integration of total sensor system

The total sensor system should be integrated and miniaturized for industrial applications. Our NV experiments were performed by using home-built system presented in Appendix B.1. The system consists of the microscope on optical table ($>$ 1 m) and a lot of bench-top measurement instruments controlled by PC. The total system including the laser, detector and microwave system and micro-controller would be integrated on diamond chip as in Fig. 8.3. Graphene could serve as, for example, optically transparent electrodes for microwave irradiation on diamond surface. Toward this kind of integration, we have started miniaturization of the measurement system as in Fig. 8.4. There are many works to do with electronics and photonics technologies toward the integration of the quantum sensor system.

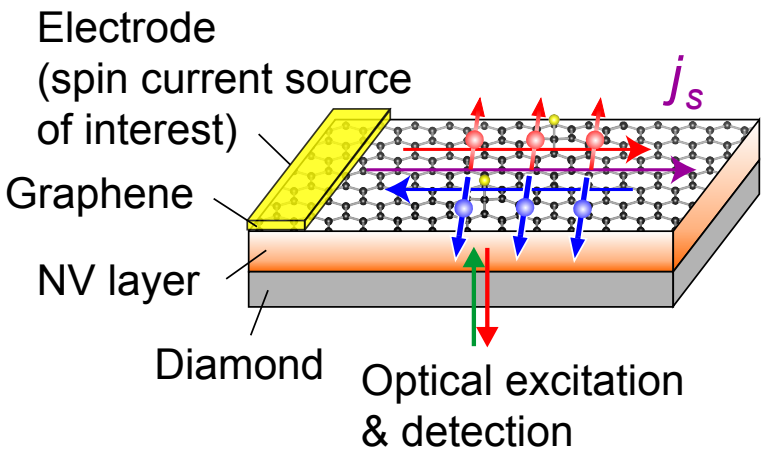

Figure 8.2: Schematic of spin current sensor device using graphene and NV center.

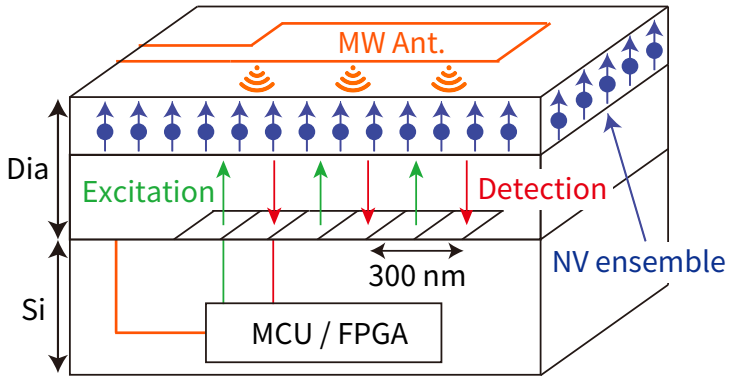

Figure 8.3: Schematic of the concept of integrated on-chip device.

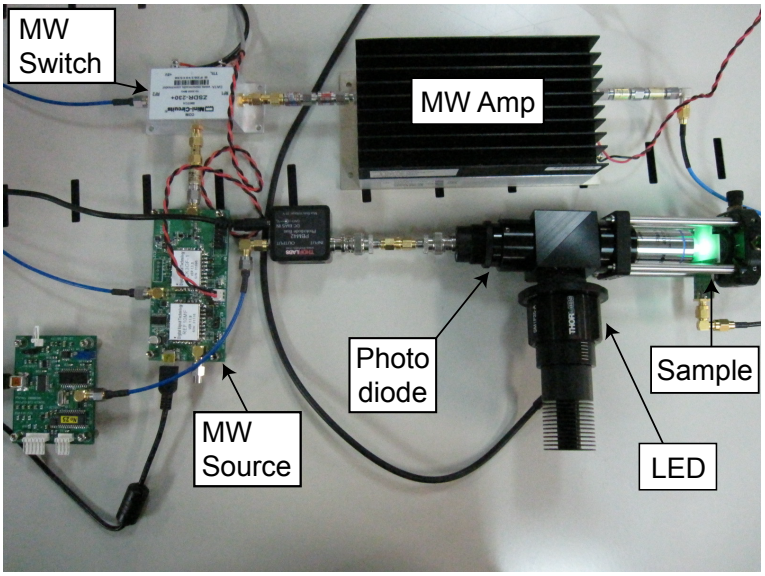

Figure 8.4: Picture of the prototype miniaturized system.

Appendix A

Calculation details

Here we describe calculation details skipped in the main text of this thesis.

A.1 Rabi nutation

We shall calculate the evolution of NV spin states (qubit) under a static and oscillating (microwave) magnetic fields $\boldsymbol{B} = (B_1 \cos(\omega_{MW} t + \phi_{MW}), -B_1 \sin(\omega_{MW} t + \phi_{MW}), B_0)$ to derive Eq. 1.9. On basis of $\{|0\rangle, |-1\rangle\}$, the spin Hamiltonian (Eq. 1.2) can be represented as

$$H_{gs} = \begin{pmatrix} 0 & \frac{\mu_B g_\perp}{\sqrt{2}}\left(B_x - iB_y\right) \\ \frac{\mu_B g_\perp}{\sqrt{2}}\left(B_x + iB_y\right) & D_{gs} - \mu_B g_\parallel B_z \end{pmatrix} \tag{A.1}$$

$$= \hbar \begin{pmatrix} 0 & \omega_1 e^{i(\omega_{MW} t + \phi_{MW})} \\ \omega_1 e^{-i(\omega_{MW} t + \phi_{MW})} & \omega_0 \end{pmatrix}. \tag{A.2}$$

Arbitrary quantum state at time t can be written as $|\psi(t)\rangle = a_0(t)\,|0\rangle + a_{-1}(t)\,|-1\rangle$.

Solution of Schrödinger equation using the Hamiltonian and state ket above is complicated because both of the two depends on time. To simplify the problem, we shall move onto the rotating frame, which is rotating around z-axis at angular frequency $-\omega_{MW} t$. Such transformation is performed by unitary operator

$$U_R = \exp(-i\omega_{MW} t S_z) = \begin{pmatrix} e^{-i\omega_{MW} t} & 0 & 0 \\ 0 & 1 & 0 \\ 0 & 0 & e^{i\omega_{MW} t} \end{pmatrix} \tag{A.3}$$

Here basis of matrix representation is taken as $\{|1\rangle, |0\rangle, |-1\rangle\}$. In this coordinate, the Hamiltonian matrix loses time dependence as follows

$$H_{gs}^{R} = U_R H_{gs} U_R^{\dagger} = \hbar \begin{pmatrix} 0 & \omega_1 e^{i\phi_{MW}} \\ \omega_1 e^{-i\phi_{MW}} & \omega_0 \end{pmatrix} \tag{A.4}$$

The state row vector becomes

$$\left(a_0^R(t), a_{-1}^R(t)\right) = U_R \left(a_0(t), a_{-1}(t)\right) = \left(a_0(t), a_{-1}(t) e^{i\omega_{MW} t}\right). \tag{A.5}$$

Schrödinger equation in laboratory frame

$$i\frac{d}{dt}a_0(t) = \omega_1 a_{-1}(t) e^{i(\omega_{MW} t + \phi_{MW})} \tag{A.6}$$

$$i\frac{d}{dt}a_{-1}(t) = \omega_1 a_0(t) e^{-i(\omega_{MW} t + \phi_{MW})} + \omega_0 a_{-1}(t) \tag{A.7}$$

can be re-written in rotating frame as

$$i\frac{d}{dt}a_0^R(t) = \omega_1 e^{i\phi_{MW}} a_{-1}^R(t) \tag{A.8}$$

$$i\frac{d}{dt}a_{-1}^R(t) = \omega_1 e^{-i\phi_{MW}} a_0^R(t) + (\omega_0 - \omega_{MW}) a_{-1}^R(t) \tag{A.9}$$

In the case resonance is perfect ($\omega_{MW} = \omega_0$) and initial conditions $a_0^R(t) = 1, a_{-1}^R(t) = 0$, the solution becomes

$$a_0^R(t) = \cos(\omega_1 t), a_{-1}^R(t) = -ie^{-i\phi_{MW}} \sin(\omega_1 t) = e^{-i\left(\phi_{MW} + \frac{\pi}{2}\right)} \sin(\omega_1 t), \tag{A.10}$$

which can be represented as Eq. 1.9.

Appendix B

Instrumentation and methods for NV center experiments

Confocal microscopy and ODMR experiments in Chapters 5, 6, and 7 are performed using home-built measurement system. Here we will describe overview of the system and experimental methods.

B.1 Measurement system

From evaluation of photoluminescence intensity to AC magnetometer operation, we performed most of the experiments for NV center research using a home-built confocal microscope equipped with ODMR capabilities. We would say that this is not only a measurement system for the material but also a part of the sensor system.

Figure B.1 and B.2 shows the diagram and picture of the optical system of confocal microscope. A laser light (532 nm) is first passed through a neutral density (ND) filter, an acousto-optic modulator (AOM), a spatial filter and a beam expander. The ND filter is used for tuning laser power and AOM is for the pulse modulation of laser light. Spatial mode and diameter of the light is made proper by spatial filter and beam expander. After that, a part of ($\sim$ 25%) laser light is reflected by beam sampler and focused on to the diamond sample by a objective lens. We have mainly used a oil immersion lens (Olympus PLAPON60XO: 60x, NA 1.42) in Chapters 6 and 7, and a normal (no immersion) lens (Olympus MPLAPON50X: 50x, NA 0.95) in Chapter 5. The

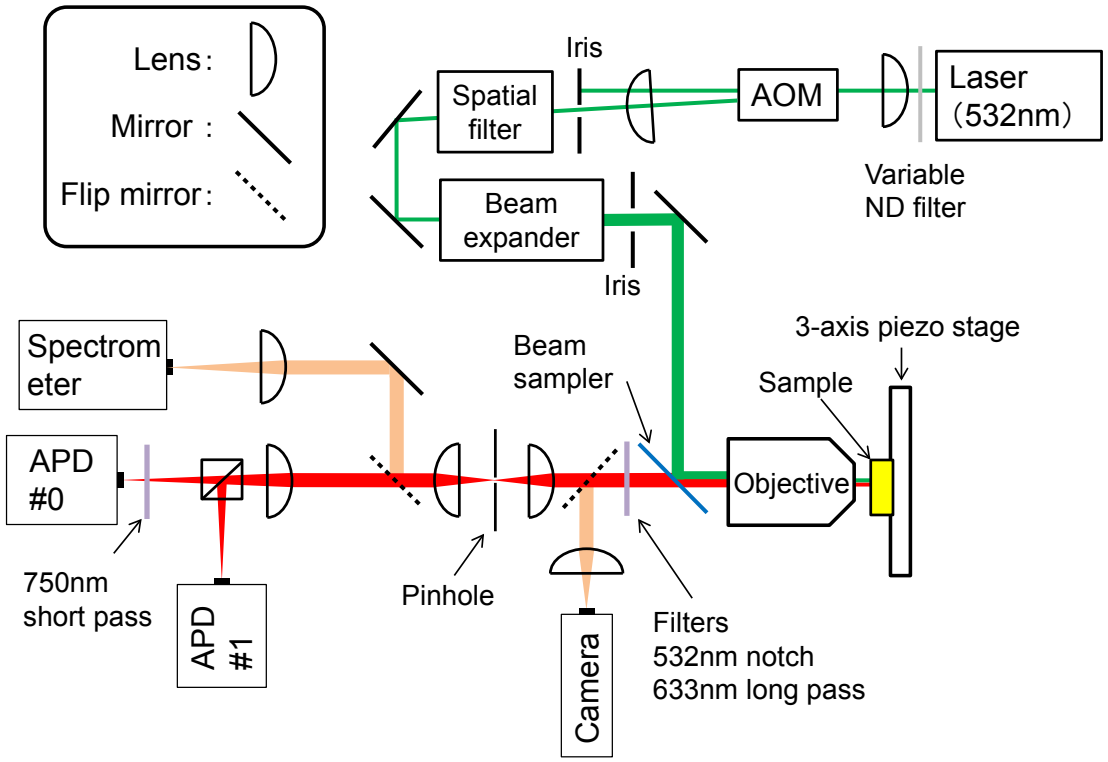

Figure B.1: The optical system of confocal microscope.

photoluminescence from the sample is collected by same objective lens and passed through beam sample, pinhole and beam splitter. The pinhole constructs the confocal system. The beam splitter pass the luminescence randomly into either of two avalanche photo diodes (APD0 or APD1) with equal probabilities. APDs are actually single photon counting modules (Excelitas SPCM-AQRH-14) which operates APD in Geiger-mode and output pulse signals per detected photons. The sample is travelled by a 3-axis piezo stage (PI P-545) to obtain planar and cross-sectional confocal micrographs. There are two alternative detectors: a camera and a spectrometer. The camera is used to observe bright field image. The spectrometer enables acquisition of photoluminescence spectrum at each confocal point.

The microwave field is irradiated to the diamond sample for ODMR experiments. The microwave signal is generated by a signal generator (Keysight N5182B) and passed through a diode switch (Minicircuits ZYSWA-2-50DR-S) for the pulse modulation and an amplifier (Minicircuits ZHL-16W-43+). We used two methods to irradiate the amplified microwave. The first one is a coil-like antenna at relatively remote position (few millimeter away from the sample) used for CW

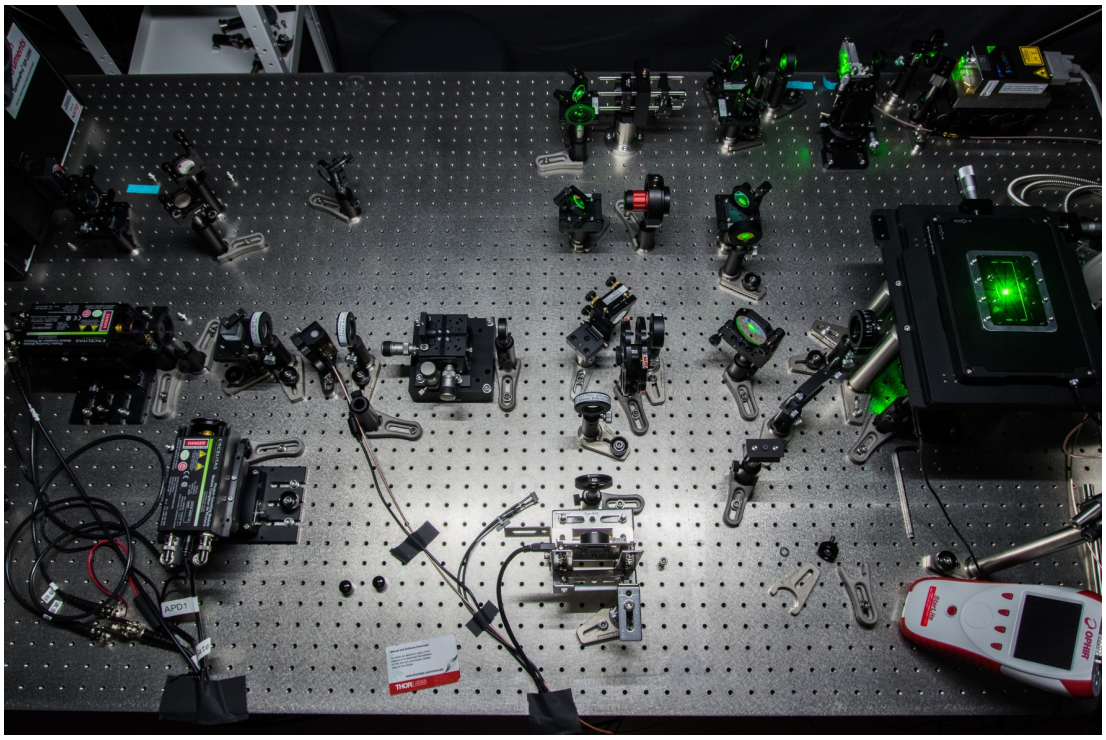

Figure B.2: Picture of confocal microscope.

ODMR experiments in Chapter 6. This approach enables a control of microwave field direction applied to the sample. The second one is a microwave wire (Cu wire with a diameter of 20 μm) passed on the surface of diamond sample. Since the distance between microwave current and the NV centers can be short (tens of microns), this approach can irradiate microwave field strong enough to conduct pulse ODMR experiments in Chapter 7.

For confocal microscopy and CW ODMR experiments, the signals from APDs (photon count pulses) are recorded by the counters on a data acquisition board (National Instruments PCI-6602). The pulses are counted during a time window of a few milliseconds and photon count rate is calculated, for each position (confocal microscopy) or microwave frequency (CW ODMR). The pulse modulation of laser and microwave is required for the pulse ODMR, concept of which is introduced in Sec. 1.6 and result of which is shown in Chapter 7. Following timing signals generated by a pulse generator (Tektronix DTG5274), laser is modulated by the AOM and microwave, the diode switch, as described above. The signals from APDs are detected as time-resolved events using a time-to-digital converter (FAST ComTec MCS6A). Recorded time-resolved photon counts

are analyzed to give normalized intensity corresponding to NV spin state (further details in B.3). Time-resolved photon counting is used for Hanbury-Brown Twiss (HBT) experiments shown in next section (B.2).

The control of the instruments and collection, analysis and visualization of the data is done by custom softwares written in Python.* Development of software heavily relies on effectiveness of the language itself and abundant powerful libraries on following list.

numpy, scipy, matplotlib and pandas data manipulation, analysis and visualization†

PyQt4 and pyqtgraph GUI development and fast visualization on it‡

PyVISA and PyDAQmx Communication with instruments§

*https://www.python.org/

†http://www.scipy.org/

‡https://riverbankcomputing.com/software/pyqt/, http://www.pyqtgraph.org/

§https://pypi.python.org/pypi/PyVISA, https://pypi.python.org/pypi/PyDAQmx

B.2 Observation of single NV center

Although our main target is high density NV center ensemble, observation of single (isolated) NV center is necessary. This is because we can estimate the density of NV center ensemble by comparing photoluminescence intensity with that of single NV center. We briefly show the results of standard observations for single NV center in this section. We use grow-in NV center in a CVD diamond film grown on (111)-oriented type-Ib substrate.

Figure B.3 shows confocal micrograph of a single NV center, which we will denote by NV1 throughout this section. Since single NV center is a single photon emitter with atomic-size, the sub-μm size of the bright spot in the micrograph is diffraction limit of the confocal microscope. Apparently, we can see wider broadening along z direction (sample depth direction) than x or y direction. To evaluate the diffraction limit quantitatively, we plot the line profiles of confocal micrographs in Fig. B.4. The profile can be fitted to a Gaussian function as shown in the Figure. For estimation of high density NV center ensemble, an effective volume of diffraction limited spot, or point spread function (PSF), should be calculated. A point intensity of arbitrary confocal micrograph contains information of finite volume: the intensity will be a convolution of the real intensity and the PSF (Gaussian function). We shall regard the PSF as a spheroid with two different semi-axes (along x and z axes) r_x and r_z. Semi-axes are defined by the area of Gaussian function divided by its height:

$$r_{x(z)} = \sqrt{2\pi}\sigma_{x(z)}/2, \tag{B.1}$$

where $\sigma_{x(z)}$ is a parameter in the common definition of Gauss function as

$$f(x) = \frac{1}{\sigma\sqrt{2\pi}} \exp\left[-(x-\mu)^2/(2\sigma^2)\right]. \tag{B.2}$$

In other words, we approximated a Gaussian function with a step function with same value of integral. The volume of PSF can be calculated as $4\pi/3r_x^2 r_z = 0.1\ \mu\mathrm{m}^3$. The density of NV ensemble is estimated by dividing its intensity by the intensity of single NV center, and by this volume.

The photon antibunching is shown by HBT-type interferometry experiments in order to show that a single NV center above is a single photon source.[135, 136] We measure the (normalized)

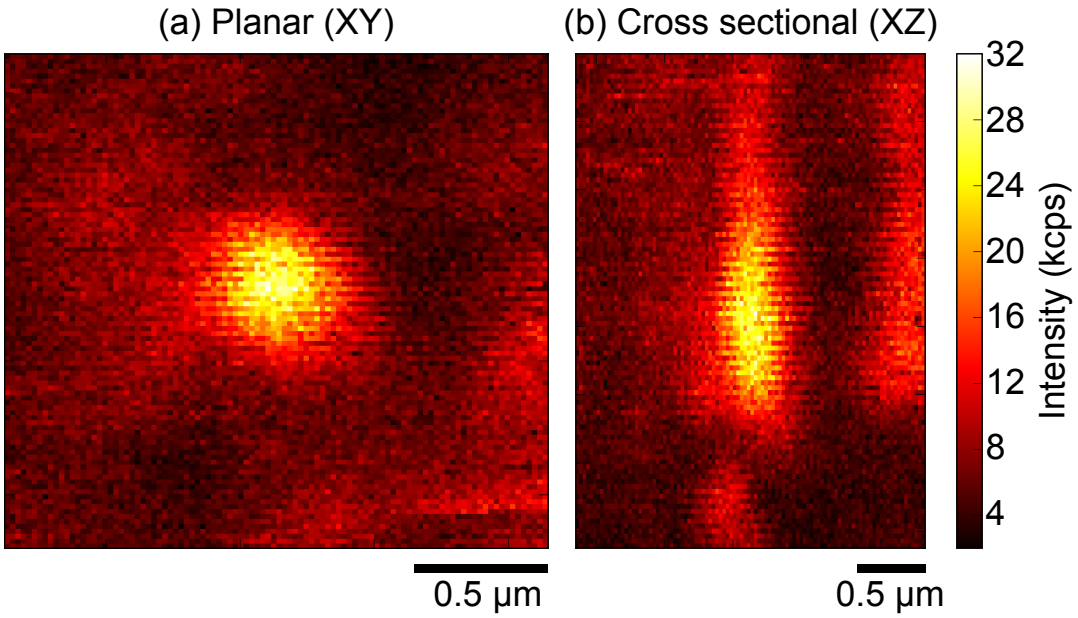

Figure B.3: (a) Planar and (b) cross sectional confocal micrographs of a single NV center. Laser power is 0.35 mW.

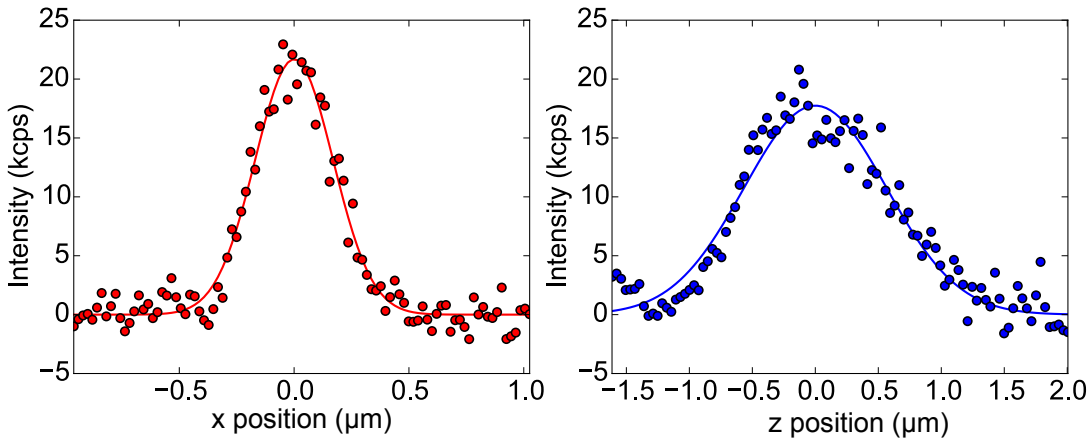

Figure B.4: Line profiles along x-axis (left) and z-axis (right) of confocal micrographs in Fig. B.3. Lines are fittings with Gaussian function. Backgrounds are subtracted.

second order correlation function of photoluminescence intensity,

$$g^{(2)}(\tau) = \frac{\langle I(t)I(t+\tau)\rangle}{\langle I(t)\rangle\langle I(t+\tau)\rangle}. \tag{B.3}$$

$I(t)$ is the intensity as a function of time, and then $g^{(2)}(\tau)$ means the rate of finding photons simultaneously at two different times separated by τ. For randomly fluctuating light, the correlation should diminish ($g^{(2)}(\tau) \to 1$) as $|\tau| \to \infty$. We are interested in the behavior at small time difference (τ). Theoretical calculation based on quantum mechanics results in, for n photon state at zero time difference,

$$g^{(2)}(0) = 1 - \frac{1}{n} < 1. \tag{B.4}$$

This is called photon antibunching. We expect $g^{(2)}(0)$ to vanish for single photon state ($n = 1$) created by single photon source. We experimentally used two APDs, a delay cable and the time-to-digital converter (TDC) to measure $g^{(2)}(\tau)$. The signal from APD0 is connected to TDC's start input while the signal of APD1 is delayed by about 60 ns and connected to stop input. TDC records the number of incoming pulses (photon counting events, $I(t)I(t+\tau)$) as a function of time between start and stop (τ). The data is normalized using expectation above: $g^{(2)}(\tau) \to 1$ ($|\tau| \to \infty$). Figure B.5 shows the results of $g^{(2)}(\tau)$ measurement under different excitation laser powers. We can see clear antibunching behavior near $\tau = 0$. $g^{(2)}(0)$ is not showing exact zero due to background light, however, it shows value about 0.25, which is much smaller than 0.5. According to Eq. B.4, $g^{(2)}(0)$ will be 0.5 if the emitted light is a two photon state. Thus, $g^{(2)}(0) < 0.5$ can be used for the evidence of single photon emitter.[135–137]

The single photon emitter shows clear saturating behavior of photoluminescence.[135, 136] Figure B.6 shows the laser power dependence of photoluminescence intensity of two different NV centers. Both dependence is well fitted to an empirical expression,

$$I(P) = \frac{I_{sat}P}{P_{sat} + P}. \tag{B.5}$$

The saturating behavior is due to a finite lifetime of excited state (and metastable singlet states). Maximum rate of photons emitted from a single NV center is limited by these lifetimes.[136] In addition to NV1, we have showed intensity of another NV center (NV2). NV2 shows lower intensity than that of NV1 at same excitation laser power. This difference seemingly originates from difference of orientation. The electric dipole lies in the plane perpendicular to the NV

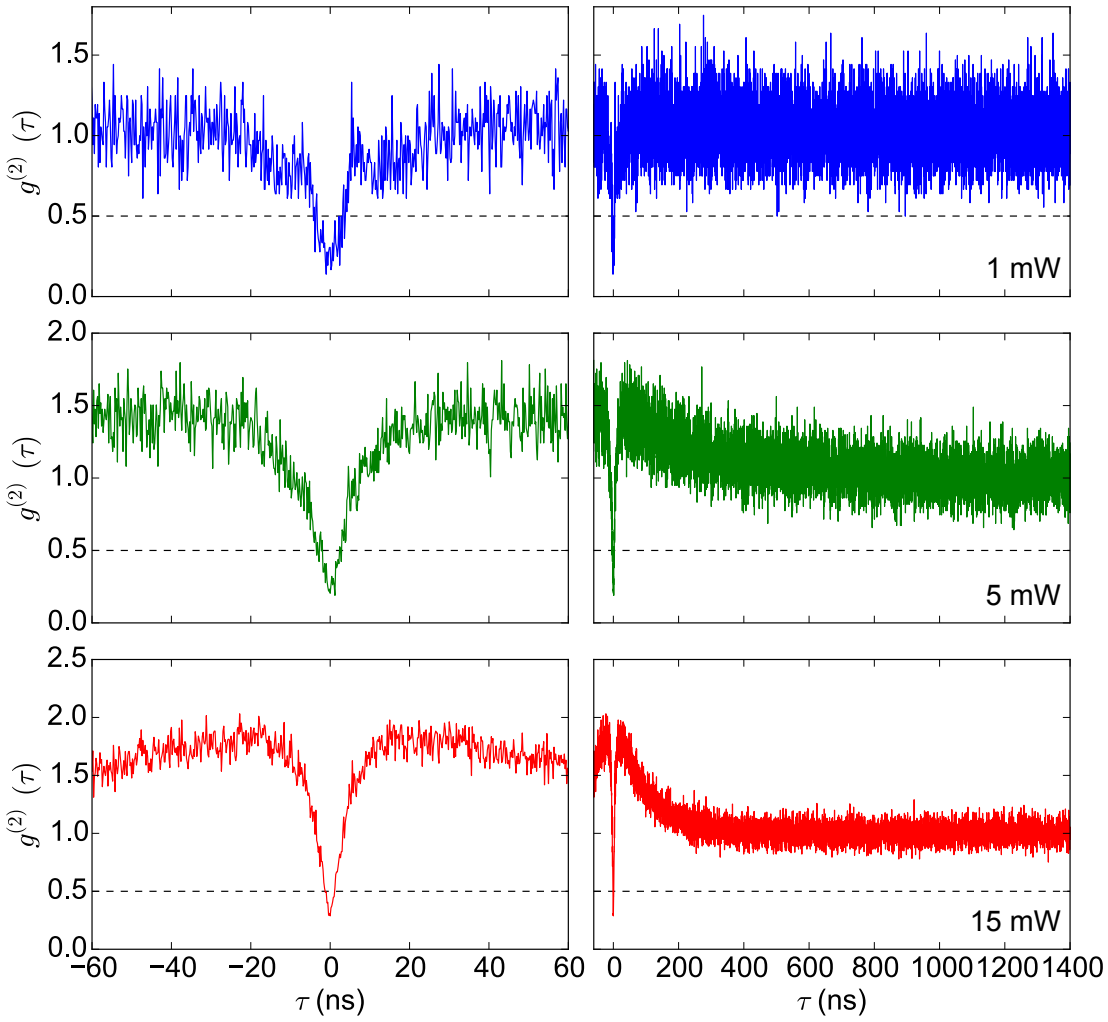

Figure B.5: The second order correlation function ($g^{(2)}(\tau)$) of photoluminescence from a single NV center (NV1).

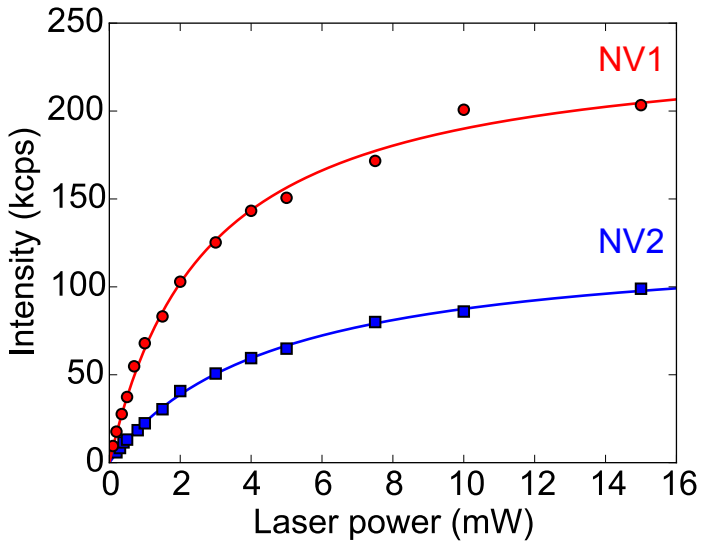

Figure B.6: Laser power dependence of photoluminescence intensity of single NV centers. P_{sat} = 2.7 mW, I_{sat} = 240 kcps for NV1. P_{sat} = 4.6 mW, I_{sat} = 130 kcps for NV2.

axis,[124] NV centers along [111] can interact more efficiently with the laser propagating toward perpendicular direction to the substrate. Several groups have reported stronger photoluminescence from single NV centers along the [111] axis than the other three.[85, 121] As shown in Fig. B.7, we determined NV center orientation using ODMR under static field along [111] direction. By comparing split of two ODMR lines, we can determine that NV1 is along [111] axis, and NV2 is along either of 3 axes other than [111].

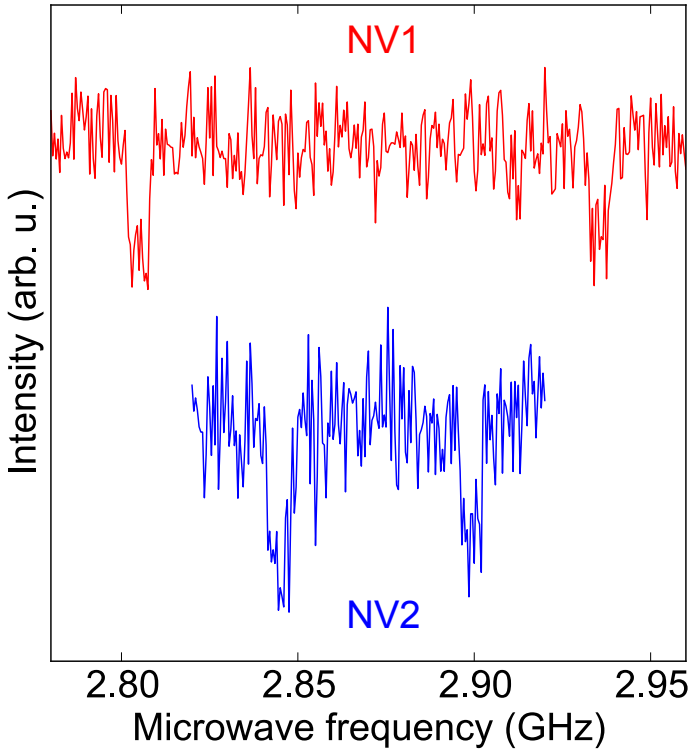

Figure B.7: ODMR of single NV centers under static magnetic field of about 25 G along [111] direction. Signal-to-noise is not very good because microwave power is not optimized.

B.3 Pulse ODMR experiments

Pulse ODMR experiments are performed using basically two different pulses, the laser and microwave pulses. Detailed descriptions of the microwave pulse sequence are presented in Sec. 1.6 in introduction and Chapter 7. In this section, we will show how to read the spin state of NV centers using the laser pulse. This is a standard method which can be found in literatures on pulse ODMR experiments of single NV center.[69, 138, 139]

Figure B.8 illustrates typical experiments to read out NV center spin state by observing photoluminescence intensity under a laser pulse. The sample is CVD2 appeared in Chapter 6 and 7. Two different initial spin states, $|m_s = 0\rangle$ and $|m_s = -1\rangle$, are prepared and read out. As shown in Fig. B.8 (a), the $|m_s = 0\rangle$ state is prepared by a laser pulse (5 μs width) and subsequent delay of 1 μs to wait the states to decay from meta stable singlet states. Preparation of $|m_s = -1\rangle$ state is done by the same laser pulse and delay, plus a resonant microwave π pulse to flip the state from $|m_s = 0\rangle$ to $|m_s = -1\rangle$. After the preparation, the spin state is read out under another laser pulse, as shown in Fig. B.8 (b). This data is recorded by directly measuring time dependence of APDs' photon counting events using TDC. The timebin is 3.2 ns and about 1.5×10^5 individual experiments are repeated for each trace. We see stronger luminescence for initial $|m_s = 0\rangle$ case than $|m_s = -1\rangle$ at the beginning of laser pulse. Since the optical pumping re-initialize the spin state, both case shows almost same intensity in latter half of the laser pulse. To quantify this difference, we set a time window of 300 ns (Signal) at the very beginning of laser pulse and another window of 2400 ns (Reference) in flat area. Normalized intensity is defined as average intensity in Signal window divided by average intensity in Reference window. This normalized intensity is used throughout Chapter 7 as a quantity representing NV center's spin state.

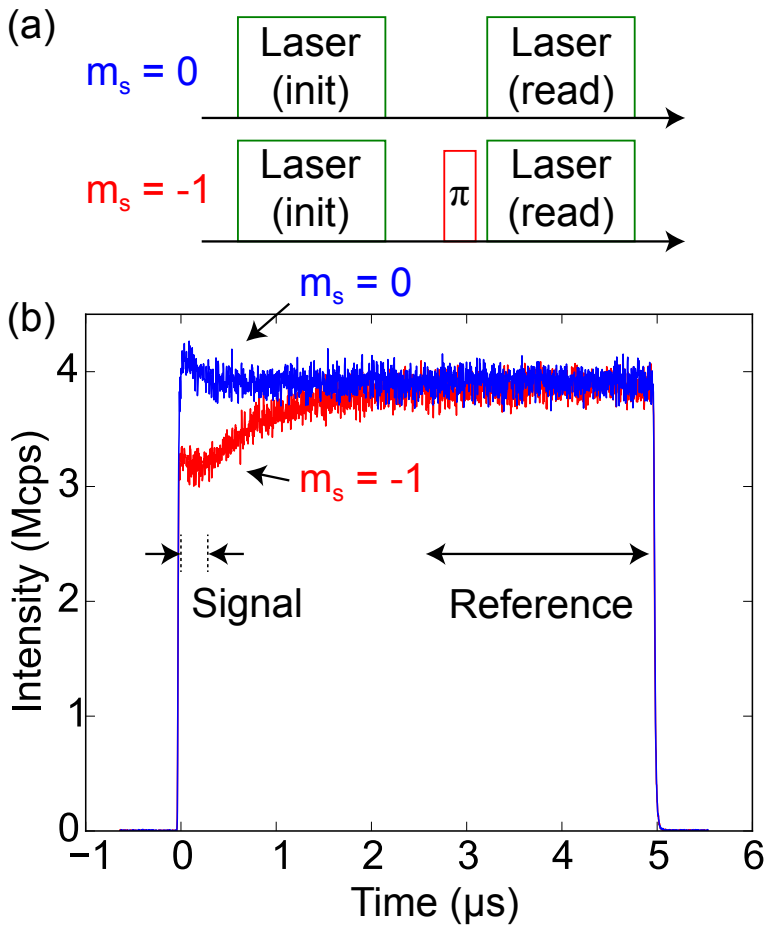

Figure B.8: Time-trace of photoluminescence intensity from NV center ensemble. (a) Pulse timings of a laser pulse (and microwave π pulse) to create initial state, and another laser pulse to read out. (b) Recorded time-trace data.

Bibliography

[1] S. Fraga, J. Karwowski, and K. M. S. Saxena, *Handbook of atomic data* (Elsevier Scientific Pub. Co., 1976).

[2] P. Y. Yu and M. Cardona, *Fundamentals of Semiconductors* (Springer, Berlin, 2010).

[3] T. Staudacher, F. Shi, S. Pezzagna, J. Meijer, J. Du, C. a. Meriles, F. Reinhard, and J. Wrachtrup, Science **339**, 561 (2013).

[4] S. J. DeVience, L. M. Pham, I. Lovchinsky, A. O. Sushkov, N. Bar-Gill, C. Belthangady, F. Casola, M. Corbett, H. Zhang, M. Lukin, H. Park, A. Yacoby, and R. L. Walsworth, Nature Nanotechnology **10**, 129 (2015), arXiv:1406.3365 .

[5] T. Häberle, D. Schmid-Lorch, F. Reinhard, and J. Wrachtrup, Nature Nanotechnology **10**, 125 (2015).

[6] C. Müller, X. Kong, J.-M. Cai, K. Melentijević, A. Stacey, M. Markham, D. Twitchen, J. Isoya, S. Pezzagna, J. Meijer, J. F. Du, M. B. Plenio, B. Naydenov, L. P. McGuinness, and F. Jelezko, Nature Communications **5**, 4703 (2014).

[7] F. Dolde, H. Fedder, M. W. Doherty, T. Nöbauer, F. Rempp, G. Balasubramanian, T. Wolf, F. Reinhard, L. C. L. Hollenberg, F. Jelezko, and J. Wrachtrup, Nature Physics **7**, 459 (2011), arXiv:1103.3432 .

[8] M. W. Doherty, V. V. Struzhkin, D. A. Simpson, L. P. McGuinness, Y. Meng, A. Stacey, T. J. Karle, R. J. Hemley, N. B. Manson, L. C. L. Hollenberg, and S. Prawer, Physical Review Letters **112**, 047601 (2014), arXiv:1305.2291 .

[9] N. Tokuda, M. Fukui, T. Makino, D. Takeuchi, S. Yamasaki, and T. Inokuma, Japanese Journal of Applied Physics **52** (2013), 10.7567/JJAP.52.110121.

[10] K. S. Novoselov, A. K. Geim, S. V. Morozov, D. Jiang, Y. Zhang, S. V. Dubonos, I. V. Grigorieva, and A. A. Firsov, Science **306**, 666 (2004).

[11] X. Du, I. Skachko, A. Barker, and E. Y. Andrei, Nature nanotechnology **3**, 491 (2008).

[12] J. P. Perdew, K. Burke, and M. Ernzerhof, Physical Review Letters **77**, 3865 (1996).

[13] M. Y. Han, B. Özyilmaz, Y. Zhang, and P. Kim, Physical Review Letters **98**, 206805 (2007).

[14] X. Wang, Y. Ouyang, X. Li, H. Wang, J. Guo, and H. Dai, Physical Review Letters **100**, 206803 (2008).

[15] E. McCann, Physical Review B **74**, 161403 (2006).

[16] T. Ohta, A. Bostwick, T. Seyller, K. Horn, and E. Rotenberg, Science **313**, 951 (2006).

[17] J. B. Oostinga, H. B. Heersche, X. Liu, A. F. Morpurgo, and L. M. K. Vandersypen, Nature Materials **7**, 151 (2008).

[18] F. Xia, D. B. Farmer, Y.-m. Lin, and P. Avouris, Nano Letters **10**, 715 (2010).

[19] J. O. Sofo, A. S. Chaudhari, and G. D. Barber, Physical Review B **75**, 153401 (2007).

[20] D. C. Elias, R. R. Nair, T. M. G. Mohiuddin, S. V. Morozov, P. Blake, M. P. Halsall, A. C. Ferrari, D. W. Boukhvalov, M. I. Katsnelson, A. K. Geim, and K. S. Novoselov, Science **323**, 610 (2009).

[21] R. R. Nair, W. Ren, R. Jalil, I. Riaz, V. G. Kravets, L. Britnell, P. Blake, F. Schedin, A. S. Mayorov, S. Yuan, M. I. Katsnelson, H.-M. Cheng, W. Strupinski, L. G. Bulusheva, A. V. Okotrub, I. V. Grigorieva, A. N. Grigorenko, K. S. Novoselov, and A. K. Geim, Small **6**, 2877 (2010).

[22] O. Leenaerts, H. Peelaers, A. D. Hernández-Nieves, B. Partoens, and F. M. Peeters, Physical Review B **82**, 195436 (2010).

[23] K.-J. Jeon, Z. Lee, E. Pollak, L. Moreschini, A. Bostwick, C.-M. Park, R. Mendelsberg, V. Radmilovic, R. Kostecki, T. J. Richardson, and E. Rotenberg, ACS nano **5**, 1042 (2011).

[24] F. Withers, M. Dubois, and A. K. Savchenko, Physical Review B **82**, 073403 (2010).

[25] X. Hong, S.-H. Cheng, C. Herding, and J. Zhu, Physical Review B **83**, 085410 (2011).

[26] F. Withers, S. Russo, M. Dubois, and M. F. Craciun, Nanoscale Research Letters **6**, 526 (2011).

[27] T. O. Wehling, M. I. Katsnelson, and A. I. Lichtenstein, Physical Review B **80**, 085428 (2009).

[28] T. O. Wehling, S. Yuan, A. I. Lichtenstein, A. K. Geim, and M. I. Katsnelson, Physical Review Letters **105**, 056802 (2010).

[29] J. P. Robinson, H. Schomerus, L. Oroszlány, and V. I. Fal'ko, Physical Review Letters **101**, 196803 (2008).

[30] A. Lherbier, S. M.-M. Dubois, X. Declerck, S. Roche, Y.-M. Niquet, and J.-C. Charlier, Physical Review Letters **106**, 046803 (2011).

[31] N. Leconte, A. Lherbier, F. Varchon, P. Ordejon, S. Roche, and J.-C. Charlier, Physical Review B **84**, 235420 (2011).

[32] S.-H. Cheng, K. Zou, F. Okino, H. R. Gutierrez, A. Gupta, N. Shen, P. C. Eklund, J. O. Sofo, and J. Zhu, Physical Review B **81**, 205435 (2010).

[33] X. Hong, K. Zou, B. Wang, S.-H. Cheng, and J. Zhu, Physical Review Letters **108**, 226602 (2012).

[34] N. Tombros, C. Jozsa, M. Popinciuc, H. T. Jonkman, and B. J. van Wees, Nature **448**, 571 (2007).

[35] M. Ohishi, M. Shiraishi, R. Nouchi, T. Nozaki, T. Shinjo, and Y. Suzuki, Japanese Journal of Applied Physics **46**, L605 (2007).

[36] W. Han, W. Wang, K. Pi, K. McCreary, W. Bao, Y. Li, F. Miao, C. Lau, and R. Kawakami, Physical Review Letters **102**, 137205 (2009).

[37] W. Han and R. K. Kawakami, Physical Review Letters **107**, 047207 (2011).

[38] A. Avsar, T.-Y. Yang, S. Bae, J. Balakrishnan, F. Volmer, M. Jaiswal, Z. Yi, S. R. Ali, G. Güntherodt, B. H. Hong, B. Beschoten, and B. Özyilmaz, Nano Letters **11**, 2363 (2011), arXiv:1104.4715 .

[39] M. Wojtaszek, I. J. Vera-Marun, E. Whiteway, M. Hilke, and B. J. van Wees, Physical Review B **89**, 035417 (2014).

[40] D. Pesin and A. H. MacDonald, Nature Materials **11**, 409 (2012).

[41] A. H. Castro Neto and F. Guinea, Physical Review Letters **103**, 026804 (2009).

[42] D. Kochan, M. Gmitra, and J. Fabian, Physical Review Letters **112**, 116602 (2014), arXiv:1306.0230 .

[43] J. Balakrishnan, G. Kok Wai Koon, M. Jaiswal, A. H. Castro Neto, and B. Özyilmaz, Nature Physics **9**, 284 (2013).

[44] A. Ferreira, T. G. Rappoport, M. A. Cazalilla, and A. H. Castro Neto, Physical Review Letters **112**, 066601 (2014).

[45] M. Morota, Y. Niimi, K. Ohnishi, D. H. Wei, T. Tanaka, H. Kontani, T. Kimura, and Y. Otani, Physical Review B **83**, 174405 (2011).

[46] K. Ando and E. Saitoh, Nature Communications **3**, 629 (2012).

[47] L. Liu, C.-F. Pai, Y. Li, H. W. Tseng, D. C. Ralph, and R. A. Buhrman, Science **336**, 555 (2012).

[48] A. Pachoud, A. Ferreira, B. Özyilmaz, and a. H. Castro Neto, Physical Review B **90**, 035444 (2014).

[49] J. Balakrishnan, G. K. W. Koon, A. Avsar, Y. Ho, J. H. Lee, M. Jaiswal, S.-J. Baeck, J.-H. Ahn, A. Ferreira, M. A. Cazalilla, A. H. Castro Neto, and B. Özyilmaz, Nature Communications **5**, 4748 (2014).

[50] M. W. Doherty, N. B. Manson, P. Delaney, and L. C. L. Hollenberg, New Journal of Physics **13**, 025019 (2011).

[51] J. R. Maze, A. Gali, E. Togan, Y. Chu, A. Trifonov, E. Kaxiras, and M. D. Lukin, New Journal of Physics **13**, 025025 (2011), arXiv:1010.1338 .

[52] M. W. Doherty, F. Dolde, H. Fedder, F. Jelezko, J. Wrachtrup, N. B. Manson, and L. C. L. Hollenberg, Physical Review B **85**, 205203 (2012).

[53] P. G. Baranov, A. P. Bundakova, A. A. Soltamova, S. B. Orlinskii, I. V. Borovykh, R. Zondervan, R. Verberk, and J. Schmidt, Physical Review B **83**, 125203 (2011).

[54] S.-Y. Lee, M. Widmann, T. Rendler, M. W. Doherty, T. M. Babinec, S. Yang, M. Eyer, P. Siyushev, B. J. M. Hausmann, M. Loncar, Z. Bodrog, A. Gali, N. B. Manson, H. Fedder, and J. Wrachtrup, Nature Nanotechnology **8**, 487 (2013).

[55] A. L. Falk, B. B. Buckley, G. Calusine, W. F. Koehl, V. V. Dobrovitski, A. Politi, C. A. Zorman, P. X.-L. Feng, and D. D. Awschalom, Nature Communications **4**, 1819 (2013).

[56] H. Kraus, V. A. Soltamov, D. Riedel, S. Väth, F. Fuchs, A. Sperlich, P. G. Baranov, V. Dyakonov, and G. V. Astakhov, Nature Physics **10**, 157 (2013).

[57] P. V. Klimov, A. L. Falk, B. B. Buckley, and D. D. Awschalom, Physical Review Letters **112**, 087601 (2014).

[58] J. R. Weber, W. F. Koehl, J. B. Varley, A. Janotti, B. B. Buckley, C. G. Van de Walle, and D. D. Awschalom, Proceedings of the National Academy of Sciences **107**, 8513 (2010).

[59] T. D. Ladd, F. Jelezko, R. Laflamme, Y. Nakamura, C. Monroe, and J. L. O'Brien, Nature **464**, 45 (2010), arXiv:1009.2267 .

[60] H. Bernien, B. Hensen, W. Pfaff, G. Koolstra, M. S. Blok, L. Robledo, T. H. Taminiau, M. Markham, D. J. Twitchen, L. Childress, and R. Hanson, Nature **497**, 86 (2013), arXiv:1212.6136 .

[61] W. Pfaff, B. J. Hensen, H. Bernien, S. B. van Dam, M. S. Blok, T. H. Taminiau, M. J. Tiggelman, R. N. Schouten, M. Markham, D. J. Twitchen, and R. Hanson, Science **345**, 532 (2014), arXiv:1404.4369 .

[62] G. Balasubramanian, I. Y. Chan, R. Kolesov, M. Al-Hmoud, J. Tisler, C. Shin, C. Kim, A. Wojcik, P. R. Hemmer, A. Krueger, T. Hanke, A. Leitenstorfer, R. Bratschitsch, F. Jelezko, and J. Wrachtrup, Nature **455**, 648 (2008).

[63] J. M. Taylor, P. Cappellaro, L. Childress, L. Jiang, D. Budker, P. R. Hemmer, A. Yacoby, R. Walsworth, and M. D. Lukin, Nature Physics **4**, 810 (2008).

[64] L. Rondin, J.-P. Tetienne, T. Hingant, J.-F. Roch, P. Maletinsky, and V. Jacques, Reports on Progress in Physics **77**, 056503 (2014), arXiv:1311.5214 .

[65] H. Y. Carr and E. M. Purcell, Physical Review **94**, 630 (1954).

[66] S. Meiboom and D. Gill, Review of Scientific Instruments **29**, 688 (1958).

[67] T. Gullion, D. B. Baker, and M. S. Conradi, Journal of Magnetic Resonance **89**, 479 (1990).

[68] W. M. Itano, J. C. Bergquist, J. J. Bollinger, J. M. Gilligan, D. J. Heinzen, F. L. Moore, M. G. Raizen, and D. J. Wineland, Physical Review A **47**, 3554 (1993).

[69] L. Childress, M. V. Gurudev Dutt, J. M. Taylor, A. S. Zibrov, F. Jelezko, J. Wrachtrup, P. R. Hemmer, and M. D. Lukin, Science **314**, 281 (2006).

[70] P. L. Stanwix, L. M. Pham, J. R. Maze, D. Le Sage, T. K. Yeung, P. Cappellaro, P. R. Hemmer, A. Yacoby, M. D. Lukin, and R. L. Walsworth, Physical Review B **82**, 201201 (2010), arXiv:1006.4219 .

[71] N. Mizuochi, P. Neumann, F. Rempp, J. Beck, V. Jacques, P. Siyushev, K. Nakamura, D. J. Twitchen, H. Watanabe, S. Yamasaki, F. Jelezko, and J. Wrachtrup, Physical Review B **80**, 041201 (2009), arXiv:0811.4731 .

[72] G. Balasubramanian, P. Neumann, D. Twitchen, M. Markham, R. Kolesov, N. Mizuochi, J. Isoya, J. Achard, J. Beck, J. Tissler, V. Jacques, P. R. Hemmer, F. Jelezko, and J. Wrachtrup, Nature Materials **8**, 383 (2009).

[73] V. M. Acosta, E. Bauch, M. P. Ledbetter, C. Santori, K.-M. C. Fu, P. E. Barclay, R. G. Beausoleil, H. Linget, J. F. Roch, F. Treussart, S. Chemerisov, W. Gawlik, and D. Budker, Physical Review B **80**, 115202 (2009).

[74] J. W. Baldwin, M. K. Zalalutdinov, T. Feygelson, B. B. Pate, J. E. Butler, and B. H. Houston, Diamond and Related Materials **15**, 2061 (2006).

[75] C. F. Wang, Y.-S. Choi, J. C. Lee, E. L. Hu, J. Yang, and J. E. Butler, Applied Physics Letters **90**, 081110 (2007).

[76] C. F. Wang, R. Hanson, D. D. Awschalom, E. L. Hu, T. Feygelson, J. Yang, and J. E. Butler, Applied Physics Letters **91**, 201112 (2007).

[77] B. J. Hausmann, M. Khan, Y. Zhang, T. M. Babinec, K. Martinick, M. McCutcheon, P. R. Hemmer, and M. Lončar, Diamond and Related Materials **19**, 621 (2010).

[78] T. M. Babinec, B. J. M. Hausmann, M. Khan, Y. Zhang, J. R. Maze, P. R. Hemmer, and M. Lončar, Nature Nanotechnology **5**, 195 (2010).

[79] E. Neu, P. Appel, M. Ganzhorn, J. Miguel-Sánchez, M. Lesik, V. Mille, V. Jacques, A. Tallaire, J. Achard, and P. Maletinsky, Applied Physics Letters **104**, 153108 (2014).

[80] S. A. Momenzadeh, R. J. Stöhr, F. F. de Oliveira, A. Brunner, A. Denisenko, S. Yang, F. Reinhard, and J. Wrachtrup, Nano letters **15**, 165 (2015), arXiv:1409.0027 .

[81] A. M. Edmonds, U. F. S. D'Haenens-Johansson, R. J. Cruddace, M. E. Newton, K.-M. C. Fu, C. Santori, R. G. Beausoleil, D. J. Twitchen, and M. L. Markham, Physical Review B **86**, 035201 (2012), arXiv:1112.5757 .

[82] L. M. Pham, N. Bar-Gill, D. Le Sage, C. Belthangady, A. Stacey, M. Markham, D. J. Twitchen, M. D. Lukin, and R. L. Walsworth, Physical Review B **86**, 121202 (2012).

[83] T. Fukui, Y. Doi, T. Miyazaki, Y. Miyamoto, H. Kato, T. Matsumoto, T. Makino, S. Yamasaki, R. Morimoto, N. Tokuda, M. Hatano, Y. Sakagawa, H. Morishita, T. Tashima, S. Miwa, Y. Suzuki, and N. Mizuochi, Applied Physics Express **7**, 055201 (2014).

[84] J. Michl, T. Teraji, S. Zaiser, I. Jakobi, G. Waldherr, F. Dolde, P. Neumann, M. W. Doherty, N. B. Manson, J. Isoya, and J. Wrachtrup, Applied Physics Letters **104**, 102407 (2014).

[85] M. Lesik, J.-P. Tetienne, A. Tallaire, J. Achard, V. Mille, A. Gicquel, J.-F. Roch, and V. Jacques, Applied Physics Letters **104**, 113107 (2014), arXiv:1401.2795 .

[86] M. Lesik, T. Plays, A. Tallaire, J. Achard, O. Brinza, L. William, M. Chipaux, L. Toraille, T. Debuisschert, A. Gicquel, J. Roch, and V. Jacques, Diamond and Related Materials **56**, 47 (2015), arXiv:1504.02011 .

[87] E. H. Martins Ferreira, M. V. O. Moutinho, F. Stavale, M. M. Lucchese, R. B. Capaz, C. A. Achete, and A. Jorio, Physical Review B **82**, 125429 (2010).

[88] P. Venezuela, M. Lazzeri, and F. Mauri, Physical Review B **84**, 035433 (2011).

[89] Z. Luo, T. Yu, Z. Ni, S. Lim, H. Hu, J. Shang, L. Liu, Z. Shen, and J. Lin, The Journal of Physical Chemistry C **115**, 1422 (2011).

[90] H. Yang, M. Chen, H. Zhou, C. Qiu, L. Hu, F. Yu, W. Chu, S. Sun, and L. Sun, The Journal of Physical Chemistry C **115**, 16844 (2011).

[91] M. Chen, H. Zhou, C. Qiu, H. Yang, F. Yu, and L. Sun, Nanotechnology **23**, 115706 (2012).

[92] J. C. Meyer, A. K. Geim, M. I. Katsnelson, K. S. Novoselov, T. J. Booth, and S. Roth, Nature **446**, 60 (2007).

[93] J. T. Robinson, J. S. Burgess, C. E. Junkermeier, S. C. Badescu, T. L. Reinecke, F. K. Perkins, M. K. Zalalutdniov, J. W. Baldwin, J. C. Culbertson, P. E. Sheehan, and E. S. Snow, Nano Letters **10**, 3001 (2010).

[94] T. Shirasaki, F. Moguet, L. Lozano, and A. Tressaud, Carbon **37**, 1891 (1999).

[95] H. Y. Liu, Z. F. Hou, C. H. Hu, Y. Yang, and Z. Z. Zhu, The Journal of Physical Chemistry C **116**, 18193 (2012).

[96] J.-H. Chen, C. Jang, S. Xiao, M. Ishigami, and M. S. Fuhrer, Nature Nanotechnology **3**, 206 (2008).

[97] B. I. Shklovskii and A. L. Efros, *Electronic Properties of Doped Semiconductors* (Springer, Berlin, 1984).

[98] B. Huard, N. Stander, J. Sulpizio, and D. Goldhaber-Gordon, Physical Review B **78**, 121402 (2008).

[99] E. J. H. Lee, K. Balasubramanian, R. T. Weitz, M. Burghard, and K. Kern, Nature Nanotechnology **3**, 486 (2008).

[100] P. Blake, R. Yang, S. Morozov, F. Schedin, L. Ponomarenko, A. Zhukov, R. Nair, I. Grigorieva, K. Novoselov, and A. Geim, Solid State Communications **149**, 1068 (2009).

[101] K. Tahara, T. Iwasaki, A. Matsutani, and M. Hatano, Applied Physics Letters **101**, 163105 (2012).

[102] J. Ye, M. F. Craciun, M. Koshino, S. Russo, S. Inoue, H. Yuan, H. Shimotani, A. F. Morpurgo, and Y. Iwasa, Proceedings of the National Academy of Sciences **108**, 13002 (2011).

[103] N. H. Shon and T. Ando, Journal of the Physics Society Japan **67**, 2421 (1998).

[104] J.-H. Chen, C. Jang, S. Adam, M. S. Fuhrer, E. D. Williams, and M. Ishigami, Nature Physics **4**, 377 (2008).

[105] M. M. Lucchese, F. Stavale, E. H. Martins Ferreira, C. Vilani, M. V. O. Moutinho, R. B. Capaz, C. A. Achete, and A. Jorio, Carbon **48**, 1592 (2010).

[106] L. G. Cançado, A. Jorio, E. H. M. Ferreira, F. Stavale, C. A. Achete, R. B. Capaz, M. V. O. Moutinho, A. Lombardo, T. S. Kulmala, and A. C. Ferrari, Nano letters **11**, 3190 (2011).

[107] K. Novoselov, A. Geim, S. Morozov, D. Jiang, M. I. Katsnelson, I. V. Grigorieva, S. Dubonos, and A. Firsov, Nature **438**, 197 (2005).

[108] E. McCann, K. Kechedzhi, V. I. Fal'ko, H. Suzuura, T. Ando, and B. L. Altshuler, Physical Review Letters **97**, 146805 (2006).

[109] K. Kechedzhi, E. McCann, V. I. Fal'ko, H. Suzuura, T. Ando, and B. L. Altshuler, The European Physical Journal Special Topics **148**, 39 (2007).

[110] E. Abrahams, P. W. Anderson, P. A. Lee, and T. V. Ramakrishnan, Physical Review B **24**, 6783 (1981).

[111] M. Uren, R. Davies, M. Kaveh, and M. Pepper, Journal of Physics C: Solid State Physics **14**, L395 (1981).

[112] D. Bishop, R. Dynes, and D. Tsui, Physical Review B **26**, 773 (1982).

[113] A. A. Kozikov, D. W. Horsell, E. McCann, and V. I. Fal'ko, Physical Review B **86**, 045436 (2012).

[114] D. A. Abanin, A. V. Shytov, L. S. Levitov, and B. I. Halperin, Physical Review B **79**, 035304 (2009).

[115] I. Aharonovich, J. C. Lee, A. P. Magyar, D. O. Bracher, and E. L. Hu, Laser & Photonics Reviews **7**, L61 (2013).

[116] K. J. Pooley, J. H. Joo, and E. L. Hu, APL Materials **2**, 012111 (2014).

[117] D. Sovyk, V. Ralchenko, M. Komlenok, A. A. Khomich, V. Shershulin, V. Vorobyov, I. Vlasov, V. Konov, and A. Akimov, Applied Physics A **118**, 17 (2015).

[118] J. P. Hadden, J. P. Harrison, A. C. Stanley-Clarke, L. Marseglia, Y.-L. D. Ho, B. R. Patton, J. L. O'Brien, and J. G. Rarity, Applied Physics Letters **97**, 241901 (2010).

[119] M. Jamali, I. Gerhardt, M. Rezai, K. Frenner, H. Fedder, and J. Wrachtrup, Review of Scientific Instruments **85**, 123703 (2014).

[120] C. Wild, R. Kohl, N. Herres, W. Müller-Sebert, and P. Koidl, Diamond and Related Materials **3**, 373 (1994).

[121] T. P. M. Alegre, C. Santori, G. Medeiros-Ribeiro, and R. G. Beausoleil, Physical Review B **76**, 165205 (2007), arXiv:0705.2006 .

[122] N. Tokuda, T. Makino, T. Inokuma, and S. Yamasaki, Japanese Journal of Applied Physics **51**, 090107 (2012).

[123] X.-f. He, N. B. Manson, and P. T. H. Fisk, Physical Review B **47**, 8816 (1993).

[124] R. J. Epstein, F. M. Mendoza, Y. K. Kato, and D. D. Awschalom, Nature Physics **1**, 94 (2005), arXiv:0507706 [cond-mat] .

[125] T. Miyazaki, Y. Miyamoto, T. Makino, H. Kato, S. Yamasaki, T. Fukui, Y. Doi, N. Tokuda, M. Hatano, and N. Mizuochi, Applied Physics Letters **105**, 261601 (2014).

[126] G. Z. Cao, J. J. Schermer, W. J. P. van Enckevort, W. A. L. M. Elst, and L. J. Giling, Journal of Applied Physics **79**, 1357 (1996).

[127] S. Dunst, H. Sternschulte, and M. Schreck, Applied Physics Letters **94**, 224101 (2009).

[128] H. Ozawa, K. Tahara, *et al.*, (in preparation).

[129] G. de Lange, D. Ristè, V. V. Dobrovitski, and R. Hanson, Physical Review Letters **106**, 080802 (2011).

[130] Ł. Cywiński, R. M. Lutchyn, C. P. Nave, and S. Das Sarma, Physical Review B **77**, 174509 (2008).

[131] B. Naydenov, F. Dolde, L. T. Hall, C. Shin, H. Fedder, L. C. L. Hollenberg, F. Jelezko, and J. Wrachtrup, Physical Review B **83**, 081201 (2011).

[132] J. R. Maze, P. L. Stanwix, J. S. Hodges, S. Hong, J. M. Taylor, P. Cappellaro, L. Jiang, M. V. G. Dutt, E. Togan, A. S. Zibrov, A. Yacoby, R. L. Walsworth, and M. D. Lukin, Nature **455**, 644 (2008).

[133] T. Wolf, P. Neumann, K. Nakamura, H. Sumiya, T. Ohshima, J. Isoya, and J. Wrachtrup, Physical Review X **5**, 041001 (2015).

[134] Y. K. Kato, R. C. Myers, A. C. Gossard, and D. D. Awschalom, Science **306**, 1910 (2004).

[135] C. Kurtsiefer, S. Mayer, P. Zarda, and H. Weinfurter, Physical Review Letters **85**, 290 (2000).

[136] F. Jelezko and J. Wrachtrup, physica status solidi (a) **203**, 3207 (2006).

[137] M. W. Doherty, N. B. Manson, P. Delaney, F. Jelezko, J. Wrachtrup, and L. C. Hollenberg, Physics Reports **528**, 1 (2013), arXiv:arXiv:1302.3288v1 .

[138] F. Jelezko, T. Gaebel, I. Popa, A. Gruber, and J. Wrachtrup, Physical Review Letters **92**, 076401 (2004).

[139] R. Hanson, O. Gywat, and D. D. Awschalom, Physical Review B **74**, 161203 (2006), arXiv:0608233 [quant-ph] .